12-14-2012 12:00 AM

Crystal Structure and Al/Si Cation Ordering in "Fassaite": A Combined Single Crystal, 27Al and 29Si NMR Study

Monika M. Haring
The University of Western Ontario

Supervisor
Dr. Roberta Flemming
The University of Western Ontario

Graduate Program in Geology

A thesis submitted in partial fulfillment of the requirements for the degree in Master of Science

© Monika M. Haring 2012

CRYSTAL STRUCTURE AND Al/Si CATION ORDERING IN "FASSAITE": A COMBINED SINGLE CRYSTAL, ^{27}Al AND ^{29}Si NMR STUDY

(Al/Si Cation Ordering in "Fassaite")

(Integrated Article)

by

Monika M.M. <u>Haring</u>

Graduate Program in M.Sc. Geology

A thesis submitted in partial fulfillment
of the requirements for the degree of
Master of Science in Geology

The School of Graduate and Postdoctoral Studies
The University of Western Ontario
London, Ontario, Canada

© Monika M.M. Haring 2012

THE UNIVERSITY OF WESTERN ONTARIO
School of Graduate and Postdoctoral Studies

CERTIFICATE OF EXAMINATION

Supervisor   Examiners

_____   _____
Dr. Roberta Flemming   Dr. Sean Shieh

Supervisory Committee

                                                            _____
                                                            Dr. Kim Tait

_____
Dr. H Wayne Nesbitt

                                                            _____
                                                            Dr. John Corrigan

The thesis by

Monika Magdaline-Marion <u>Haring</u>

entitled:

Crystal Structure and Al/Si Cation Ordering in "Fassaite": A Combined Single Crystal, ^{27}Al and ^{29}Si NMR Study

is accepted in partial fulfillment of the
requirements for the degree of
Master of Science in Geology

_____   _____
            Date   Chair of the Thesis Examination Board

ii

Abstract

Al-,Ti-rich diopside, referred to herein as fassaite, occurs in both terrestrial and extraterrestrial environments. The composition of fassaite, $Ca(Mg, Al)(Si, Al)_2 O_6$, makes it ideal for Al/Si cation ordering studies. In this study, crystal XRD, ^{27}Al and ^{29}Si MAS NMR as well as ^{27}Al 3QMAS NMR is used to study cation ordering in extraterrestrial fassaite from Allende CAIs and a terrestrial analogue from Fassa Valley Italy. From ^{27}Al and ^{29}Si spectroscopy, fassaite from Allende CAIs is found to have more local Al/Si cation ordering than terrestrial fassaite. Both terrestrial and extraterrestrial have $C2/c$ symmetry indicating long range cation disorder. Completely ordered fassaite has never been found in nature. The local ordering in the Allende fassaite likely indicates ordering above the disorder/ order transition temperature. Cation ordering could provide an independent estimate of temperature and cooling rate on the Allende parent body, once the transformation temperature is known.

Keywords

Acknowledgements

Table of Contents

Chapter 2

List of Tables

Chapter 1

Chapter 2

Chapter 3

Chapter 4

List of Figures

Chapter 1

Chapter 2

Chapter 3

Chapter 4

List of Appendices

Table of Abbreviations

Al-Diop	Al-Diopside
An	Anorthite
AOA	Amoeboid Olivine Aggregate
APFU	Atoms Per Formula Unit
AU	Astonomical Unit
B_1	Radio frequency field
B_o	External magnetic field
BSE	Back Scattered Electron
CAI	Ca- Al-rich Inclusion
CaTs	Calcium Tschermak pyroxene
CB	Becubbin type carbonaceous chondrite
CCAM	Carbonaceous Chondrite Anhydrous Mineral
CH	Carbonaceous chondrite with a High metal content
CI	Ivuna type carbonaceous chondrite
CK	Karoonda type carbonaceous chondrite
CM	Mighei type carbonaceous chondrite
CO	Ornans type carbonaceous chondrite
C_Q	Quadrupolar coupling constant
CR	Renazzo type carbonaceous chondrite
CSA	Chemical Shift Anisotropy
CV	Vigarano type carbonaceous chondrite
Di	Diopside
EPFU	Electrons Per Formula Unit
EPMA	Electron Probe Micro Analysis
F CAI	CAI with Fractionation anomalies
Fas	Fassaite
FEG-SEM	Field Emission Gun Scanning Electron Microscope
FID	Free Induction Decay
Fo	Forsterite
FUN CAI	CAI with Fractionation and Unidentified Nuclear anomalies
FWHM	Full Width Half Maximum
GADDS	General Area Detector Diffraction System
h	Planck's constant
H^1_Q	First order quadrupolar interaction
H^2_Q	Second order quadrupolar interaction

Hib	Hibonite
HREE	Heavy Rare Earth Element
H_z	Zeeman effect
I	Spin quantum number
ICDD	International Center for Difraction Data
IOM	Institute of Meteoritics
Kir	Kirschtenite
LREE	Light Rare Earth Element
M	Magnetization
M_1	Magnetic nuclear spin quantum number
MAS NMR	Magic Angle Spinning Nuclear Magnetic Resonance
Mel	Melilite
MQMAS NMR	Multiple Quantum Magic Angle Spinning Nuclear Magnetic Resonance
Mtx	Matrix
NMR	Nuclear Magnetic Resonance
NNN	Next Nearest Neighbour
N_α	Lower energy $2I + 1$ energy levels
N_β	Higher energy $2I + 1$ energy levels
P	Pressure
P	Spin angular momentum
Pv	Perovskite
Q	Quadrupolar moment
REE	Rare Earth Element
RF	Radio Frequency
SEM - EDS	Scanning Electron Microscopy - Energy Dispersive Spectrometry
SOF	Site Occupancy Factor
Sp	Spinel
T	Temperature
T_1	Spin-lattice interaction
T_2	Spin-spin interaction
TF	Terrestrial Fractionation
UN CAI	CAI with Unidentified Nuclear anomalies
Ves	Vesuvianite
v_o	Larmor frequency
XRD	X-ray Diffraction
γ	Gyromagnetic ratio
ΔE	Difference between $2I + 1$ energy levels in Hz
θ	Angle between the internuclear vector and the external magnetic field

θ_m	Magic angle (54°44')
μ	Nuclear spin magnetic moment (a.k.a. Magnetic moment)

Chapter 1: Introduction

1.1 Fassaite

Clinopyroxene is a Ca - rich single chain silicate mineral, with the general formula XYT_2O_6, that occurs over a wide range of temperatures (T) and pressures (P). This mineral forms a complete solid solution between $CaMgSi_2O_6$ (diopside) and $CaFeSi_2O_6$ (hedenbergite) although other elements, most importantly aluminum and titanium, may be substituted for Mg and Fe (Deer et al. 1987). The large stability field of pyroxene makes it a ubiquitous phase in both terrestrial environments and extra-terrestrial environments. This in combination with the effect of temperature and pressure makes pyroxene useful in geothermobarometry. Aluminous pyroxene such as jadeite ($NaAlSi_2O_6$) and omphacite (($Ca,Na)(Mg,Fe,Al)Si_2O_6$) are of particular importance to geobarometers due to the positive correlation between Al_2O_3 content and pressure of formation for pyroxene. These aluminous pyroxenes contain a significant proportion of calcium Tschermak's component ($CaAl_2SiO_6$) which becomes incorporated into the structure through Tschermak reactions such as $(Si^{4+}) + [Mg^{2+}] \rightarrow (Al^{3+}) + [Al^{3+}]$ where ( ) is a tetrahedral site and [ ] is an octahedral site. This study focuses on an aluminous pyroxene known as fassaite ($Ca(Mg,Fe,Al,Ti)(Si,Al)_2O_6$).

Fassaite is a name first introduced to describe a light to dark green pyroxene from an augite syenite-limestone contact in Fassa valley, Trentino, Italy (Deer et al. 1987). Although the name "fassaite" has been discredited by the International Mineralogical Association (IMA), the name fassaite is used for brevity to describe Al-rich Ti-bearing diopside. In a terrestrial context, this name has been more often used to describe aluminum – rich and sodium – poor pyroxene usually occurring in metamorphosed limestones and dolomites as well as eclogitic inclusions

from kimberlites. The name fassaite was also widely adopted by the meteoritics community to describe this Ti-bearing and Al-rich diopside-like clinopyroxene, because it occurs widely in the solar system, in Calcium Aluminum-rich Inclusions (CAIs) for example (Deer et al 1987, Brearley & Jones 1998). The name was discredited in 1988 by the IMA-CNMNC naming commission, in favour of "sub-silicic titanoan aluminian pyroxene" (Morimoto N. et al. 1988 Am Min 73, 1123), but I will retain the name "fassaite" throughout, for brevity. The structure of fassaite was determined by Peacor in 1967 from samples of a carbonatite complex in Oka, Quebec, Canada. Peacor (1967) determined the unit cell of fassaite to be a 9.794, b 8.906, c 5.319 Å, and β 105.90° with spacegroup $C2/c$, similar to the unit cell of diopside. The unit cell parameters of fassaite, however vary with composition. It has been shown that $[Fe^{3+}] + (Al^{3+}) \rightarrow [Mg^{2+}] + (Si^{4+})$ substitutions decrease b and increase c whereas $[Ti^{4+}] + 2(Al^{3+}) \rightarrow [Mg^{2+}] + 2(Si^{4+})$ substitutions decrease b and β and increase a and c (Coleman 1962).

Compositionally, fassaite is also characterized by a high calcium content (CaO ~ 25 %) as well as a high but variable Al content. Aluminum in fassaite replaces cations in both tetrahedral sites and octahedral M1 sites through Tschermak reactions described above (Deer et al. 1987). In tetrahedral sites, the replacement of Si by Al is between 0.25 and 0.50 per mole. This significant replacement of Si by Al makes fassaite useful for Al/Si cation ordering studies (See discussion below). Cation ordering describes the arrangement of cations in a crystal structure which can be more regular or ordered versus more random or disordered. This process is highly temperature dependant with structures becoming more disordered with increasing temperature (Neuhoff et al. 2003). Disordered cation arrangements may be preserved at lower temperatures if the mineral is quenched.

Besides Al and Mg, the M1 site in fassaite may contain additional cations such as Fe^{3+}, Fe^{2+}, Ti^{4+}, Ti^{3+}, V^{3+}, and Sc^{3+} (Deer et al. 1987, Dowty & Clark 1973). The proportions of these cations vary between crystallization environments of fassaite. For example, terrestrial fassaite tends have more Fe, particularly Fe^{3+}, than meteoritic fassaite where there is little or no Fe and more Ti^{3+}, Ti^{4+} and Al (Deer et al. 1987). This compositional difference can be explained by meteoritic fassaite having formed in more refractory environments than Earth fassaite and thus the less-refractory element iron is unable to condense (Grossman 1972). In this study the meteoritic fassaite samples are from ultrarefractory Ca-Al-rich inclusions (CAIs) (see discussion below).

1.2. Solid-state Nuclear Magnetic Resonance Spectroscopy

(Information in following text cited from: Keeler 2002, Grant & Harris 1996, Schlichter 1990, Bovey 1987, and Abragam 1961, unless otherwise stated)

Cation ordering studies have been completed on a variety of mineral structures and often involve solid state nuclear magnetic resonance (NMR) spectroscopy techniques. Nuclear magnetic resonance was first observed experimentally in 1945 by Felix Bloch at Stanford University and Edward Purcell at Harvard University. This electromagnetic radiation has a resonance frequency that is affected by the strength of the magnetic field as well as the magnetic properties of the nuclei. Solid-state NMR techniques are often used in addition to single crystal and powder X-ray diffraction techniques. The NMR spectra of solids are affected by changes in bond lengths, angles, and the local symmetry around nuclei making solid state NMR techniques ideal for cation ordering studies (Duer 2002, Kirkpatrick 1988).

1.2.1. NMR Basics

NMR spectroscopy exploits intrinsic properties of atomic nuclei such as spin angular momentum (a.k.a. spin) and magnetic moment to determine structure and dynamics of materials at a molecular level. Spin is given a spin quantum number, "I", which either an integer or half integer (i.e. 0, ½, 1, 3/2, 2, ...). The spin quantum number has important implication on the ability to collect NMR spectra for a certain nuclei. Spin angular momentum or spin is a vector quantity and its direction and magnitude are quantized. In certain nuclei (e.g. ^{12}C, ^{16}O, ...), the spin quantum number $I = 0$ and as such the nuclei have no angular momentum and thus no nuclear movement and so an NMR spectrum cannot be acquired. It can be easily predicted for which nuclei an NMR spectrum can or cannot be acquired by simply determining the number of protons and neutrons (Table 1.1). For nuclei with even numbers of protons and neutrons, $I = 0$ and therefore they are NMR inactive and no NMR spectrum can be acquired.

Finally, the spin quantum number can predict the shape of the positive charge distribution in a nucleus (Table 1.1). For nuclei where $I = 1/2$, the positive charge distribution is spherical. When I for a nucleus is greater than 1/2, the positive charge distribution is non-spherical, such nuclei have a nuclear electric quadrupolar moment (Q). Whether a nucleus is quadrupolar or not has implications on how the NMR spectrum is acquired and processed as well as its appearance (discussed below).

Isotope	# of Protons	# of Neutrons	Spin I	NMR Active	Gyromagnetic Ratio (MHz/T)	Charge Distribution
^{1}H	1	0	1/2	Yes	42.580	Spherical
^{10}B	5	5	3	Yes	4.575	Non-spherical
^{11}B	5	6	3/2	Yes	13.660	Non-spherical
^{12}C	6	6	0	No	N/A	N/A
^{13}C	6	7	1/2	Yes	10.710	Spherical
^{14}N	7	7	1	Yes	3.076	Non-Spherical
^{15}N	7	8	1/2	Yes	4.314	Spherical
^{16}O	8	8	0	No	N/A	N/A
^{17}O	8	9	5/2	Yes	5.772	Non-spherical
^{23}Na	11	12	3/2	Yes	11.420	Non-spherical
^{27}Al	13	14	5/2	Yes	11.090	Non-spherical
^{29}Si	14	15	1/2	Yes	8.458	Spherical
^{133}Cs	55	78	7/2	Yes	5.584	Non-spherical

Table 1.1. Atomic data for Various isotopes Relevant to NMR.

The magnetic moment is a value which determines the torque a magnetic field will exert on a magnet or in the case of an NMR experiment, a certain nucleus. Spin angular momentum is linearly related to nuclear spin magnetic moment (a.k.a. magnetic moment (μ)) through the gryomagnetic ratio (γ). This relationship can be written as $\mu = \gamma P$ where P is spin angular momentum, thus nuclei with a zero angular momentum will have no magnetic moment. When nuclei with non-zero spin angular momenta are exposed to an external magnetic field (B_o) their magnetic moments, rather than reorient will begin to spin about the applied magnetic field. This spinning is known as Larmor precession and its frequency is known as the Larmor frequency (Sander & Hunter 1987). The direction in which the magnetic moments precess is determined by the gyromagnetic ratio (γ) where a negative gyromagnetic ratio means a clockwise precession and a negative gyromagnetic ratio means a counterclockwise precession.

1.2.2. Nuclear Zeeman Interaction

When an NMR active nucleus is exposed to an external magnetic field (B_o), an interaction between the nuclear spins (I) and the magnetic field occurs, known as the nuclear Zeeman interaction, occurs. For a nucleus with a nuclear spin I, there are $2I + 1$ possible energy levels associated with a magnetic nuclear spin quantum number M_1 ($M_1 = +I$, $+I$-1, $+I$-2, ..., $-I$). Before an external magnetic field (B_o) is applied, the $2I + 1$ energy levels have on average the same energy and are thus referred to as degenerate. Once the magnetic field is applied, the nuclei with different spin states begin to precess about the magnetic field axis (Fig. 1.1) and thus the $2I + 1$ nuclear spin energies become non-degenerate.
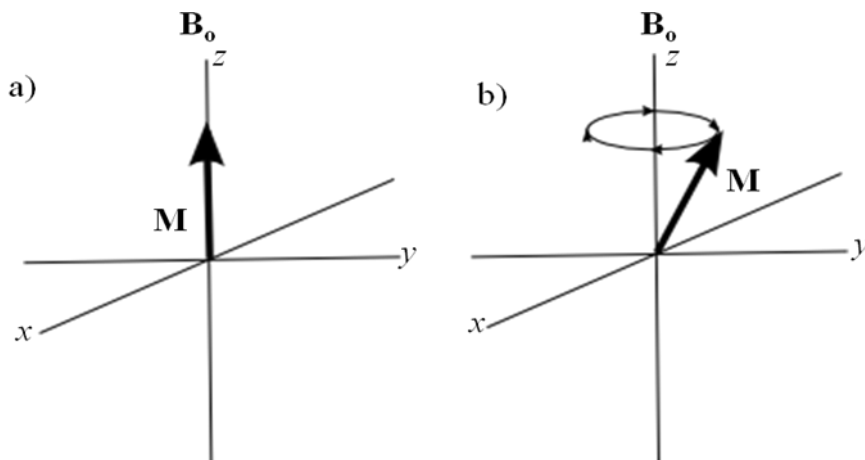
Figure 1.1. a) The magnetization (M) is oriented parallel to the z axis in the absence of an external magnetic field (B_o).   b) In the presence of an external magnetic field, the magnetization begins to precess about the magnetic field axis (z axis) at the Larmor frequency. Figure adapted from Sanders & Hunter 1987.

The strength of the nuclear Zeeman interaction is proportional to the strength of B_o, therefore a stronger magnetic field is necessary to get a larger separation between the $2I + 1$ energy levels (Fig. 1.2) (Sander & Hunter 1987). The difference between the energy levels can be expressed as $\Delta E = h\nu_o$ where h is Planck's constant and ν_o is the Larmor frequency (the frequency of precession about the magnetic field axis) in Hz.
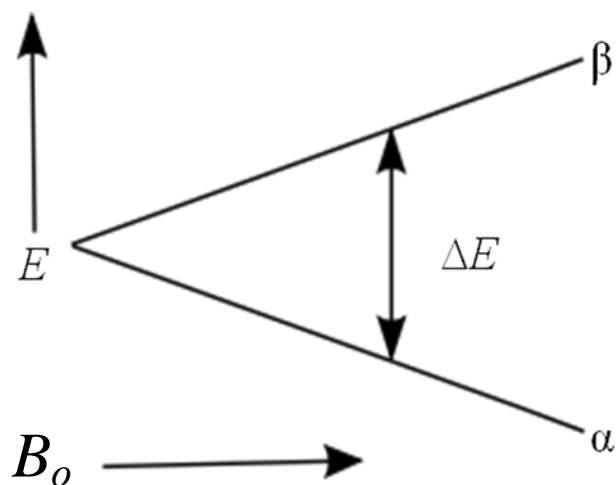
Figure 1.2. Energy diagram for a spin with I = ½ in the presence of a magnetic field (B$_o$). As the strength of B$_o$ increases, the energy difference (ΔE) between the energy levels β and α increases. β represents higher energy levels while α represent lower energy levels. Figure adapted from Sanders & Hunter 1987.

As the energy difference between the $2I + 1$ spin states increases, the population differences between energy levels increases as is expressed in the equation: $N_\beta/N_\alpha = e^{-\Delta E/kT}$, where N_β is the population in the higher energy level, N_α is the population in the lower energy level, k is the Boltzmann constant, and T is the temperature in Kelvin. From this equation, we can see that the populations follow the Boltzmann distribution and that temperature as well as magnetic field strength, both affect the population distribution. Although there is a small difference between the populations of the $2I + 1$ energy states, it is enough to impart a net magnetization on the nuclei (Sanders & Hunter 1997). The larger the difference between N_β and N_α, the better the detection sensitivity, however, the difference between the two populations is very small, making NMR insensitive compared to other spectroscopic techniques. The NMR experiment inverts these populations to generate a measurable signal (as explained in section 1.2.4.).

1.2.3. Other Nuclear Spin Interactions in NMR

The nuclear Zeeman interaction is the strongest nuclear spin interaction however, weaker interactions include chemical shift anisotropy, dipolar, and quadrupolar interactions. Chemical shift anisotropy (or chemical shielding) is the response of the magnetic cloud around the nucleus to the applied magnetic field B_o. The applied magnetic field induces a circulation of electrons which results in a small localized magnetic field. For a bare nucleus, no circulation occurs and therefore no smaller magnetic field results. The smaller magnetic field interacts with the external applied magnetic field modifying the total field experienced by the nucleus. The actual field felt by the nucleus is dependent on the electronic environment around it. For an atom, the electron density distribution is spherical thus induced motion generates a small magnetic field in the opposite direction of the external magnetic field, resulting in the nucleus being shielded from the external magnetic field. In the case of molecules, the electron circulation is more complicated and the density distribution is usually not spherical, as a result the induced magnetic field can either augment or oppose the external magnetic.

Chemical shielding and chemical shifts are both caused by induced local magnetic fields in an atom or a molecule but how they are measured differs. Chemical shifts are measured in ppm (parts per million) with respect to a reference signal, and increase from right to left. The reference signal is taken from a stable reference compound and is assigned an arbitrary shift of usually 0 ppm. Chemical shielding is measured in ppm with respect to the "bare" nucleus and increases from left to right. Because a bare nucleus is not a practical lab standard, the chemical shift is more often cited. Chemical shielding has two components: diamagnetic and paramagnetic terms. Both diamagnetic and paramagnetic terms arise from the circulation of electrons in atomic and molecular orbitals, however, the direction of circulation with respect to

the external magnetic field differs. For the diamagnetic component, electrons circulate in a plane perpendicular to the direction of the magnetic field, generating a secondary magnetic field which opposes the external magnetic field. For the paramagnetic component, electrons circulate in a direction parallel to the direction of the external magnetic field, generating a secondary magnetic field which augments the external magnetic field. This difference in direction for the secondary magnetic field makes the change in the chemical shift highly dependent on the orientation of the molecule. The directional dependence of the change in chemical shift has no effect on the spectrum of a solution due the rapid tumbling motions of molecules which averages out the anisotropic effects of chemical shielding, as a result the spectrum for a solution has narrow peaks (Duer 2002, Fyfe 1983, Mehring 1980). Narrow peaks are also possible for the NMR spectra of single crystals, however, the chemical shift of the peak corresponds to a single orientation of a crystal. In the case of a crystal powder, there are an infinite number of crystal orientations, so all chemical shifts are observed simultaneously and they each produce a discrete peak, the sum of which results in a broad powder pattern called a chemical shift envelope (Duer 2002, Fyfe 1983, Mehring 1980).

Another nuclear spin interaction that leads to broadening in the solid state is dipole-dipole coupling or direct dipole interactions. Dipole – dipole interactions are usually the dominant broadening mechanism in solids and are the result of the magnetic moments of the two spins, I and S, interacting through space (Sanders & Hunter 1987). The two spin states can be either homonuclear (i.e. spin states from the same nuclei) or heteronuclear (i.e. spin states from different nuclei).   In both cases the two neighbouring nuclei have local magnetic fields that interact with each other. The local magnetic field felt by a nuclei is therefore expressed as $B_{loc}=$ $+/-\mu_s r_{is}^{-3}(3\cos^2\theta-1)$ where μ_s is the magnetic moment of spin S, r_{is} is the distance between the

spins I and S, and θ is the angle between the internuclear vector and the external magnetic field (Sanders & Hunter 1987). The +/- sign arises from the fact that the spins generating the local magnetic fields may augment or reduce the effects of the external magnetic field (Sanders & Hunter 1987). Dipolar interactions are proportional to the gyromagnetic ratios of the nuclei involved and are inversely proportional to the cube of the internuclear distance between the two nuclei. Furthermore, the dipolar interaction is affected by the orientation of internuclear vector with respect to the external magnetic field (B_o).

In solutions, dipolar interactions have no effect on peak broadening due to the rapid tumbling motions of molecules averaging out dipolar interactions. Dipolar interactions in the solid state however, are usually not averaged to zero and are orientation dependent (Duer 2002, Fyfe 1983, Mehring 1980). In the case of a single crystals, dipolar interactions result in two peaks separated by $D(3\cos^2\theta-1)$ where D is the dipolar coupling constant and θ is the angle of the internuclear vector with respect to the external magnetic field. The separation of the peaks is therefore highly dependent on θ. If the sample is powdered, peaks for all orientations are seen simultaneously resulting in a powder pattern known as a Pake doublet (Duer 2002, Sander & Hunter 1987, Fyfe 1983, Mehring 1980).

The third nuclear spin interaction important in solids is the electric quadrupolar interaction. Electric quadrupolar interactions occur for those nuclei with spins $I > 1/2$. Nuclei with $I > 1/2$ spins have a non spherical charge distribution which gives rise to a quadrupolar moment (Q) (Keeler 2002, Grant & Harris 1996, Schlichter 1990, Bovey 1987, Ernst, Bodenhausen & Wokaun 1987). The electric quadrupolar moment interacts with the local electric field gradient at the nucleus giving rise to an electric quadrupolar interaction which causes line broadening in the resulting NMR spectrum (Sanders & Hunter 1987). The local

electric field gradient is an external property of a nucleus and arises from the environment

surrounding the nucleus. Quadrupolar interactions cause line broadening in NMR spectra by

further perturbing the quantized energy levels created by the Zeeman interaction.

Figure 1.3. Energy diagram for a quadrupolar nuclei with spin $I = 5/2$. The difference between each energy level is increased by the Zeeman effect (H_z) however, first order quadrupolar interactions (H^1_Q) perturb all energy levels except for the central transition ($+1/2 \leftrightarrow -1/2$). Second order quadrupolar interactions (H^2_Q) perturb all energy levels. Diagram adapted from Kentgens 1997.
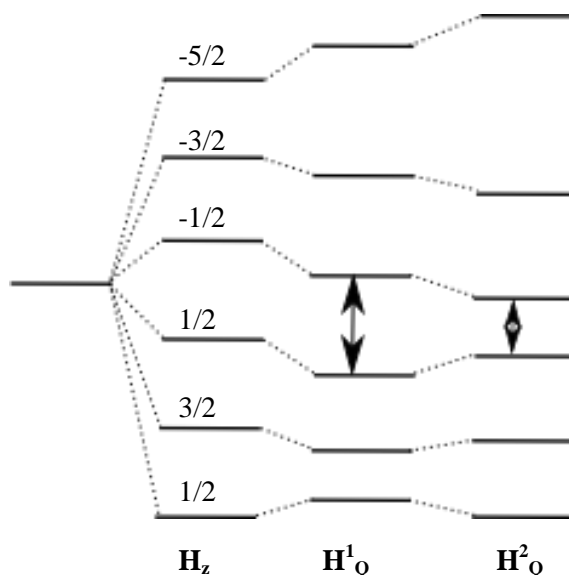
Of these energy levels, the central transition ($I = +1/2 \leftrightarrow -1/2$), is not effected in the first order

by quadrupolar interactions. First order quadrupolar interactions, however, cause the frequencies

the satellite transitions (e.g. $I = -1/2 \leftrightarrow -3/2$) to change by an amount dependant on the

quadrupolar coupling constant (C_Q).   In most cases, the magnitude quadrupolar interaction can

be within the range of that of the Zeeman interaction so therefore second order quadrupolar

interactions must be considered. Second order quadrupolar interactions perturb the central

transition as well as the satellite transitions. While the effects of first order quadrupolar

interactions may be removed by Magic Angle Spinning Nuclear Magnetic Resonance

spectroscopy (MAS NMR), second order quadrupolar interactions cannot be removed by MAS

and instead must be removed by two dimensional NMR techniques like multiple quantum NMR

(Frydman 1995).

1.2.4. A Basic Single – Pulse NMR Experiment

A basic single-pulse NMR experiment may be broken down into three steps: magnetization, perturbation, and detection. The first step in the experiment, magnetization, involves exposing the sample to an external magnetic field causing the magnetic moments of the nuclei being studied to precess about the magnetic field which will be referred to as the z-axis. At this stage the bulk magnetization of the sample is in an equilibrium state and is aligned with the z-axis.
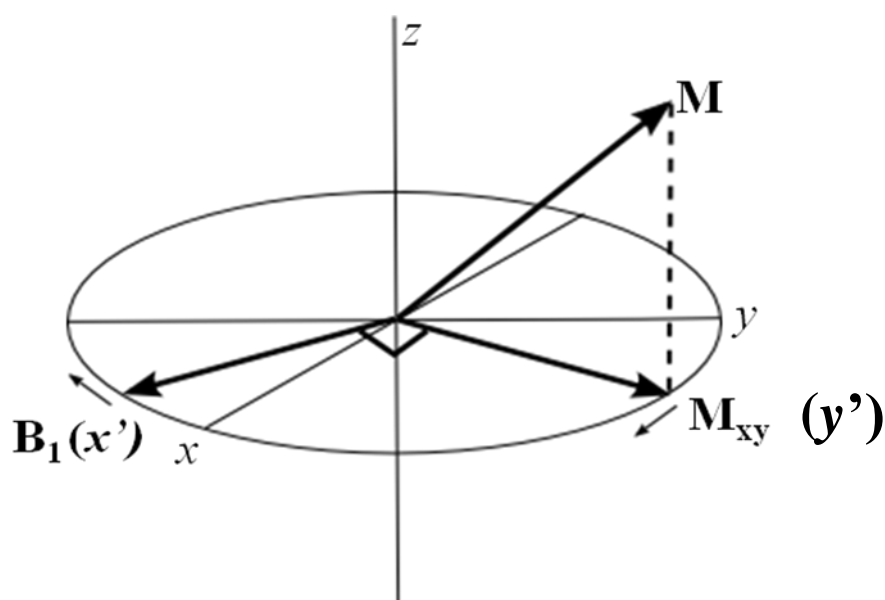
Figure 1.4. The orientations of the magnetization (M), its *xy* component (M_{xy}), and the radio frequency field (B_1). If a rotating frame of reference (*x* and *y* rotate about *z*) is considered, B_1 is referred to as *x'* and M_{xy} is referred to as *y'*. Figure adapted from Sanders & Hunter 1987.

In order to acquire an NMR signal, the equilibrium magnetization built up along the z axis must be perturbed with a second radio frequency (RF) field (B_1). This second RF field is emitted from a current in a coil positioned perpendicular to the external magnetic field and will be referred to as the x-axis. The B_1 field is much smaller in magnitude than the external

magnetic field and it has an oscillation frequency close to the Larmor frequency (the frequency

at which the magnetization precesses about the z axis). The oscillation of the B_1 field occurs

along the x-axis and can be thought of two counter rotating vectors in the xy plane (Fig. 1.5).
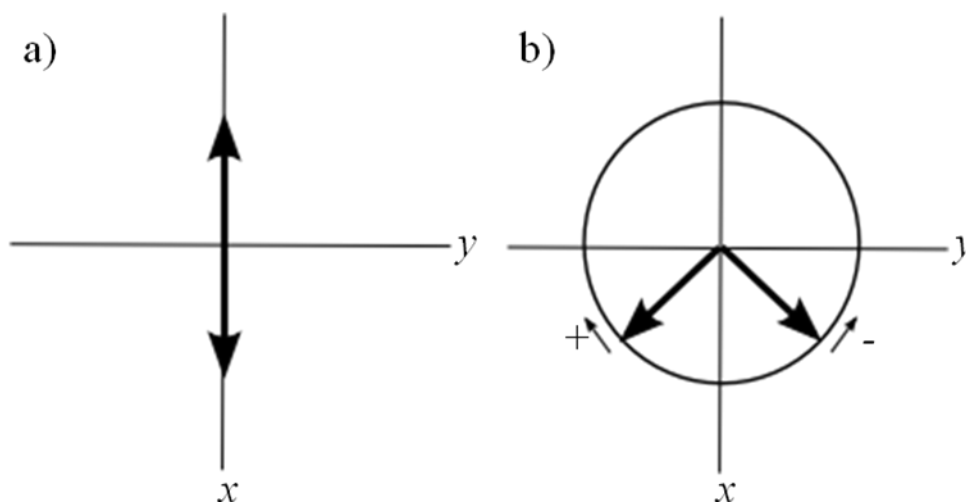
Figure 1.5. a) Oscillation of the B_1 field along *x* can be thought of as b) two counter rotating vectors in the *xy* plane. Interaction with the magnetism only occurs with the vector precessing in the same direction as the magnetization. Figure adapted from Sanders & Hunter 1987.

Of the two counter-rotating vectors, interaction only occurs between the precessing magnetism

and the vector rotating in the same direction as the precession. The interaction between the B_1

field and the magnetization produced a torque which moves the magnetization towards the xy

plane (Fig 1.6). Interactions between the magnetization and the B_1 field result in a complicated

precession in the magnification where it is precessing about the z-axis and the x-axis at the same

time (Sanders & Hunter 1987). To simplify this, NMR experiments are often looked at in a

rotating frame of reference. A rotating frame of reference is when the z' axis is in the direction

of the external magnetic field but the x' and y' axes rotate about the z' axis (Keeler 2002, Grant

& Harris 1996, Bovey 1987). The rotating reference frame essentially eliminates the angular

component of the magnetization that results from precession about the z-axis as a result only

precession about the B_1 field axis is considered (Sanders & Hunter 1987). The final position of the magnetization will depend on the length of time that the B_1 field is applied (pulse width). In NMR experiments the pulse width used is enough to rotate the magnetization 90° from the z-axis to the xy plane where the NMR signal can be directly observed.
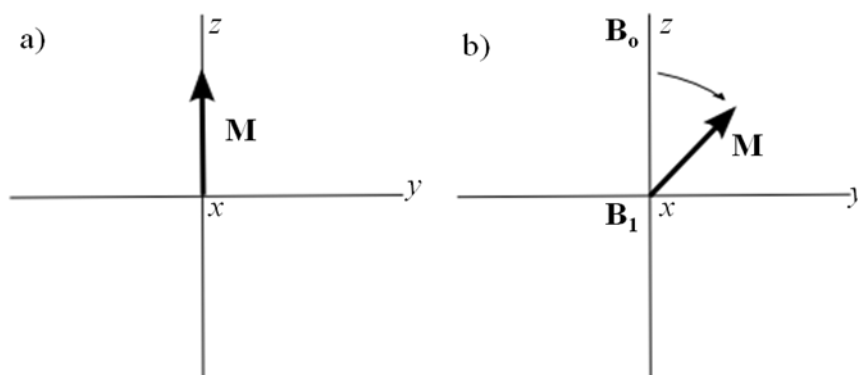
Figure 1.6. a) Magnetization at equilibrium oriented along *z*. b) In the presence of an external magnetic field (B_o) magnetization precesses about *z,* however, application of a radiofrequency field (B_1) results in simultaneous rotation about *x*. Figure by Monika Haring based on information from Sanders & Hunter 1987.

Once the magnetization is rotated 90° onto the xy plane the B_1 field is removed and the NMR signal is detected, usually at the coil that transmitted the B_1 field (Sanders & Hunter 1987). When the B_1 field is removed, the NMR signal will begin to weaken or decay as the magnetization move back to an equilibrium position along the z axis. The process is called free induction decay (FID) where free means free of the influence of the B_1 field, induction means current induced in the detection coil by the oscillating NMR signal, and decay means weakening of signal due to the magnetization going back to equilibrium (Sanders & Hunter 1987). The FID of an NMR signal is time dependant with the signal decaying exponentially while still maintaining the same frequency (Fig. 1.7).
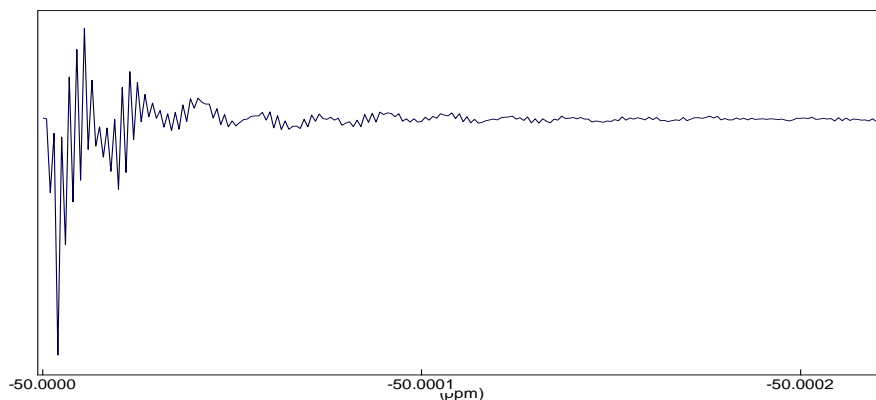
Figure 1.7. FID of terrestrial fassaite acquired at 14.1 T showing exponential decay with time. FID figure by Monika Haring.

The time it takes for the NMR signal to totally decay is known as relaxation time (or delay time in multipulse experiments where equilibrium must be reached before another pulse is completed). Two processes, spin-lattice (T_1) and spin-spin (T_2) interactions contribute to the decay or relaxation of the magnetization. Spin-lattice interactions refer to high energy spin states interacting with the surrounding lattice resulting in a loss of excess energy and thus relaxation. This relaxation process results in relaxation along the z-axis and is often referred to at longitudinal relaxation. Spin-spin relaxation refers to spin states along the xy plane losing coherence or becoming out of phase resulting in a net xy magnetization of zero (Fig. 1.8) (Sanders & Hunter 1987).
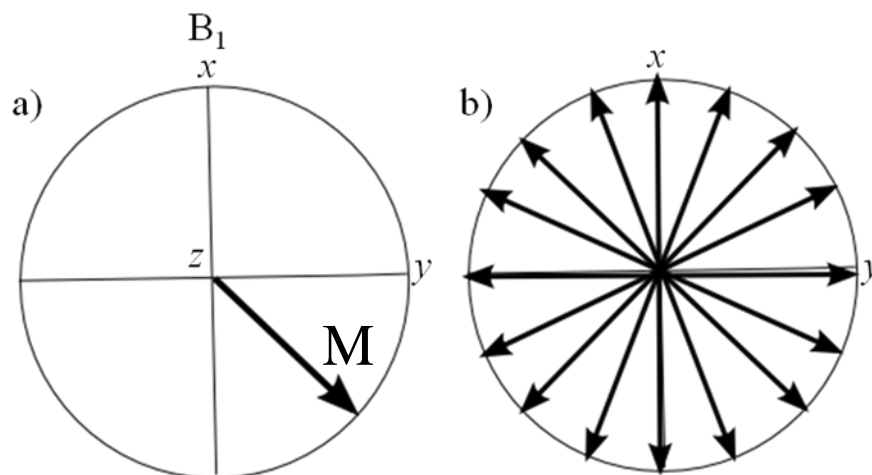
Figure 1.8. a) The presence of the radio frequency field (B$_1$) results in a coherent magnetization (M) in the *xy* plane. b) In the absence of B$_1$, the magnetization fans out into several smaller components resulting in a zero net magnetization. This process is known as spin-spin relaxation (T2). Figure by Monika Haring based on information from Sanders & Hunter 1987.

Once an FID is recorded, a Fourier transformation must be completed to convert the FID into a readable spectrum (Sanders & Hunter 1987). A Fourier transformation is a mathematical function that is used to convert time domain (time dependent) data in the FID into frequency domain (frequency dependent) data in the useable spectrum (Sanders & Hunter 1987).

1.2.5 MAS NMR Spectroscopy

As discussed above nuclei are affected by a number of nuclear spin interactions such as the nuclear Zeeman effect, chemical shift anisotropy (CSA), dipolar interactions, and electric quadrupole interactions. In solutions, these interactions have little broadening effects on spectra due to the rapid tumbling motions of atoms. In solids, atoms are in fixed positions and as such, interactions such as CSA, dipolar interactions, and quadrupolar interaction cannot be ignored because they are affected by atomic orientation. As a result, each crystallographic orientation has a unique chemical shift therefore a polycrystalline sample with an infinite number of

crystallographic orientations produces a range of chemical shifts, or chemical shift envelope, and spectral peaks appear broadened.

MAS NMR is a technique devised to eliminate the broadening effects of CSA and dipolar interactions making it possible to get high resolution spectra of solids. In solids, the angular dependence of CSA and dipolar interactions takes the form of $3\cos^2\theta - 1$ where θ is the angle between the interatomic vector and the external magnetic field. During an MAS NMR experiment, the sample is spun at an angle of 54° 44' to the external magnetic field (Fig 1.9). This angle is referred to as the "magic angle" and at that angle the $3\cos^2\theta - 1$ term goes to zero and the effects of crystallographic orientation are averaged out. Since the effects of crystallographic orientation are averaged out, the peaks on an MAS NMR spectrum represent an average or isotropic chemical shift. To ensure that the MAS NMR spectrum successfully narrows the peak, the sample must be rotated at a frequency that is at least of the order of the CSA peak width. Since peak widths are often on the order of a few kilohertz, MAS experiments are often run at ~ 3 kHz.
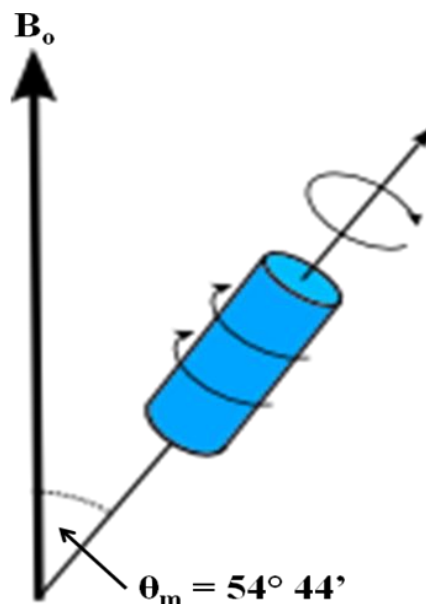
Figure 1.9. Relative positions of sample (blue cylinder) and external magnetic field (B_o) during an MAS NMR experiment (θ_m is the magic angle). Figure by Monika Haring based on information from Sanders & Hunter 1987.

$\mathbf{B_o}$

$\theta_m = 54° \ 44'$

MAS NMR is ideal for inorganic solids which have little or no hydrogen atoms in their structure. The lack of hydrogen reduces the amount of dipolar interactions and therefore peak broadening is mostly due to CSA. For nuclei that are in regular coordination polyhedra (eg. Si (tetrahedral) and Al (tetrahedral or octahedral)), CSA is often very low resulting in high resolution MAS NMR spectra in which the chemical shift for specific sites may be determined. While this technique can eliminate first order quadrupolar interactions, it cannot eliminate second order quadrupolar interactions; therefore other techniques such as multiple quantum magic angle spinning NMR spectroscopy (MQMAS NMR) must be used to get high resolution spectra on quadrupolar nuclei.

1.2.6. MQMAS NMR Spectroscopy

MQMAS NMR is a relatively new technique for studying quadrupolar nulei developed by L. Frydman and J.S. Harwood in 1995. This bidimensional technique makes it possible to obtain high resolution spectra of quadrupolar nuclei by eliminating the effects of second order quadrupolar interations. Quadrupolar interactions are affected by second and fourth order polynomials:

$$\text{Second order polynomial } P_2 \left(\cos(\theta) \right) = \tfrac{1}{2}[3\cos^2\theta - 1]$$

$$\text{Fourth order polynomial } P_4 \left(\cos(\theta) \right) = 1/8[35\cos^4\theta - 30\cos^2\theta + 3]$$

for which, no single value of θ can eliminate both polynomials, hence MAS NMR cannot eliminate second order quadrupolar interactions nor broadening (Kentgens 1997). MAS NMR can be thought of as a single quantum experiment as it uses only those coherences between energy states differing by m= +/- 1 (single quantum coherences). MQMAS NMR, on the other

hand, makes use of coherences that occur between energy states differing by more than m = +/- 1

(multiple quantum coherences) (Ernst et al. 1987) (see Fig. 1.10).

Figure 1.10. Energy diagram showing zero quantum coherences (ZQT) to triple quantum coherences (3QT). Diagram after Ernst et al. 1987.
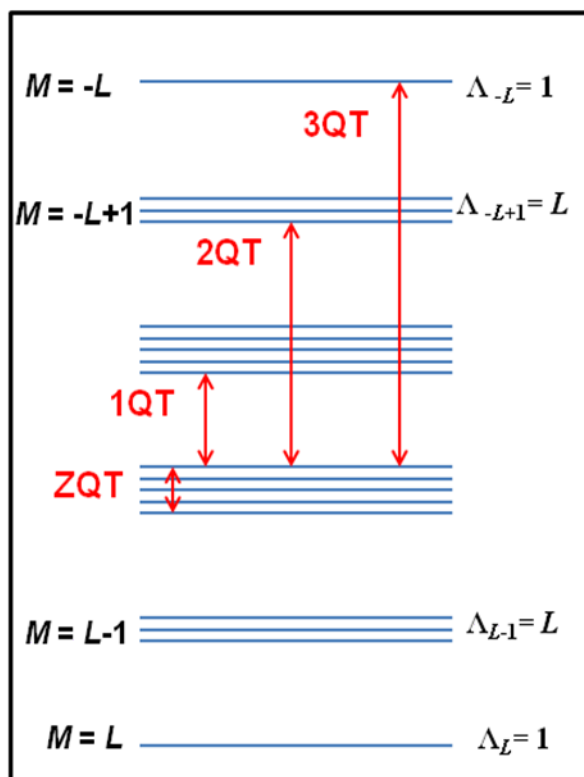
During a MQMAS experiment, excitation of multiple quantum coherences is performed by

subjecting the sample to radio frequency (RF pulses). After the initial excitation pulses, the

multiple quantum coherences undergo an evolution time in the absence of RF pulses. Unlike

single quantum coherences, multiple quantum coherences produce no magnification and cannot

be directly observed by NMR and must be converted to single quantum coherences using another

series of pulses (Kentgens 1997, Frydman & Harwood 1995, Medek et al. 1995). After the data

are collected additional data processing is performed to present data that are free of all

quadrupolar effects (Frydman & Harwood 1995, Medek et al. 1995). By using multiple quantum coherences, it is possible to select coherences that will cancel out the second order quadrupolar interactions, while spinning the sample at the magic angle will eliminate CSA, dipolar interactions, and first order quadrupolar interactions (Frydman & Harwood 1995, Medek et al. 1995). Since MQMAS NMR is a bidimensional technique, two Fourier transformations are perfomed and the spectrum is presented as a two dimensional plot. Unlike one dimensional NMR spectra, the intensity of peaks in 2D spectra (Fig. 1.11) are represented by a series of contours similar to a topographic map. The peaks in the 2D spectra are then projected onto each dimension to give two single dimensional spectra. The dimensions of 2D NMR spectra are referred to as the F1 and F2 dimensions. The F2 dimension contains single quantum data and is referred to as the MAS NMR dimension whereas the F1 dimension contains indirectly calculated multiple quantum and is referred to as the isotropic dimension (Medek et al. 1995).

F2: Magic Angle Spinning (MAS)
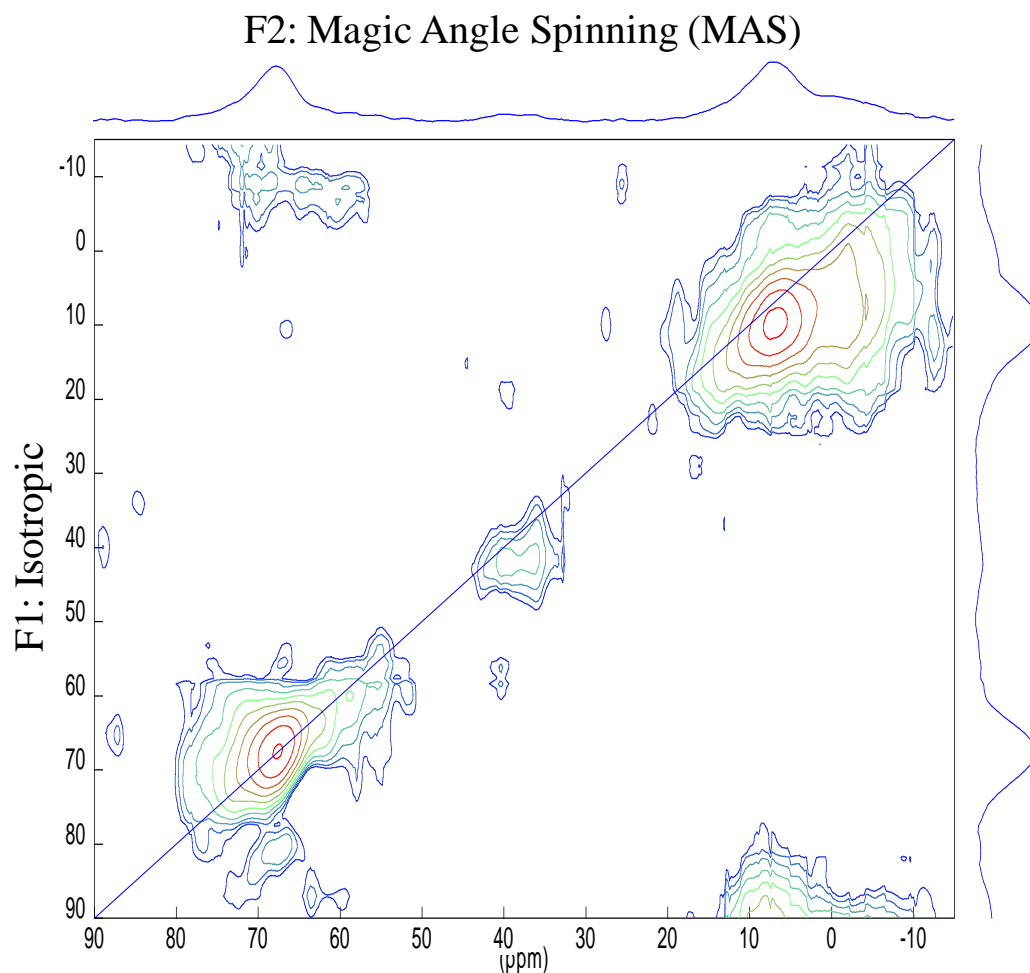
Figure 1.11. 2D ^{27}Al 3QMAS spectrum of trerrestrial fassaite at 21.1 T. Spectrum by Monika Haring.

1.2.7. Spectroscopy in the Earth Sciences

Solid-state NMR spectroscopy is often used in Earth Science disciplines such as mineralogy and geochemistry. The use of NMR spectroscopy became prevalent after the successful ^{29}Si NMR study on inorganic solids was published by Lippmaa et al. (1980). Solid state NMR has been applied to problems concerning amorphous and poorly crystalline inorganic materials, crystalline phases that are too fine grained to study by single crystal X-ray diffraction (eg. glasses, gels, zeolites, and clays), order/disorder in crystals (particularly Al/Si), structure and

dynamic behaviour of melts, detection of small amounts of phases in mixtures, and the investigation of reaction mechanisms (Kirkpatrick 1988).   Some commonly-used nuclei in Earth science related NMR studies include ^{29}Si, ^{27}Al, ^{17}O, ^{31}P, and ^{11}B (Kirkpatrick 1988). While NMR has useful applications in the Earth sciences, there are problems that arise when using NMR for natural materials. Many natural materials contain paramagnetic impurities, usually Fe^{2+}, Fe^{3+} or Mn^{2+} which cause extensive peak broadening (Sherriff & Hartman 1985, Grimmer et al. 1983).   The peak broadening results from unpaired d- or f- electrons, associated with the paramagnetic impurities, interacting with the external magnetic field, leading to a range of chemical shifts. Paramagnetic cations also promote rapid spin-spin relation (dephasing). Very rapid decay of the FID (short T_2) causes severe line broadening. (Sanders and Hunter 1987). In most cases 1-2 wt % Fe is not enough to extensively broaden peaks however, it may be enough to reduce the resolution of closely spaced peaks, especially in ^{29}Si spectra. For quadrupolar nuclei, paramagnetic effects tend to be less important due to intrinsically broad peaks (Kirkpatrick 1988).

1.3. Calcium Aluminum Inclusions (CAIs)

CAIs are whitish-grey submillimeter to centimeter sized clasts are found in chondritic meteorites. They are the earliest forming solids; with Pb-Pb age at 4568.67 +/- 0.17 Myr (Bouvier & Wadhwa 2010) and thus define the age of the solar system. CAIs are often found with younger materials such as chondrules, with an ages ranging between 4565.45 +/- 0.4 and 4562.7 +/- 0.6 Myr (Connelly et al. 2008; Amelin et al. 2002; Krot et al. 2005a), and amoeboid olivine aggregates (AOAs). AOAs are suggested to be genetically related to CAI's based on mineralogical and petrological observations (Krot et al. 2004). Based on ^{26}Al/^{27}Al ratios, AOAs

likely formed 0.1 – 0.5 Ma after CAI formation assuming that ^{26}Al was uniformly distributed in the nebula (Scott & Krot 2003).

There are two types of models for the formation of CAIs that are currently debated: shockwave models (Desch et al. 2005) and the X-wind model (Shu et al. 2001). Shockwave models postulate that CAIs, chondrules and AOA's formed within the inner 1 to 4 AU of the protoplanetary disk where periodic heating events, caused by shock waves, thermally processed amorphous presolar dust (Krot et al. 2009). The exact cause of the shockwaves is still unclear, however, scenarios such as fast moving planetesimals, collisions between planetary embryos, X-ray flares, and gravitational instability in the disk have been proposed (Krot et al. 2009).

The X-wind model is based on 1) astronomical observations of bi-polar outflows and X-ray flares from young stellar objects, 2) theoretical models of the interaction between stellar magnetic fields and the protoplanetary disk, and 3) theoretical models of the irradiation origin of short-lived radionuclide (Krot et al. 2009). This model was originally proposed to explain the coexistence of high temperature CAIs, chondrules and AOAs, with a chondrite matrix that seems to have undergone little if any thermal processing (Shu et al. 1997). Based on this model, disk accretion is divided within the inner disk (R ~ 0.06 AU) into a funnel flow onto the star and an X-wind outflow (Fig.1.12). The inner radius of the protoplanetary disk is suggested to fluctuate, stressing the protosolar magnetic field, resulting in solar flares that melt inner disk solids (Krot et al. 2009). Specifically, CAIs and AOA's are suggested to have formed closest to the proto-Sun near the funnel flow – X-wind transition region whereas chondrules formed further away within the X-wind region and as such CAIs were exposed to more radiation that produced short-lived radionuclides than chondrules (Krot et al. 2009). Both refractory inclusions and chondrules were

subsequently moved by the X-wind to 1-20 AU where they accreted with thermally unprocessed

matrix material (Shu et al. 1997).
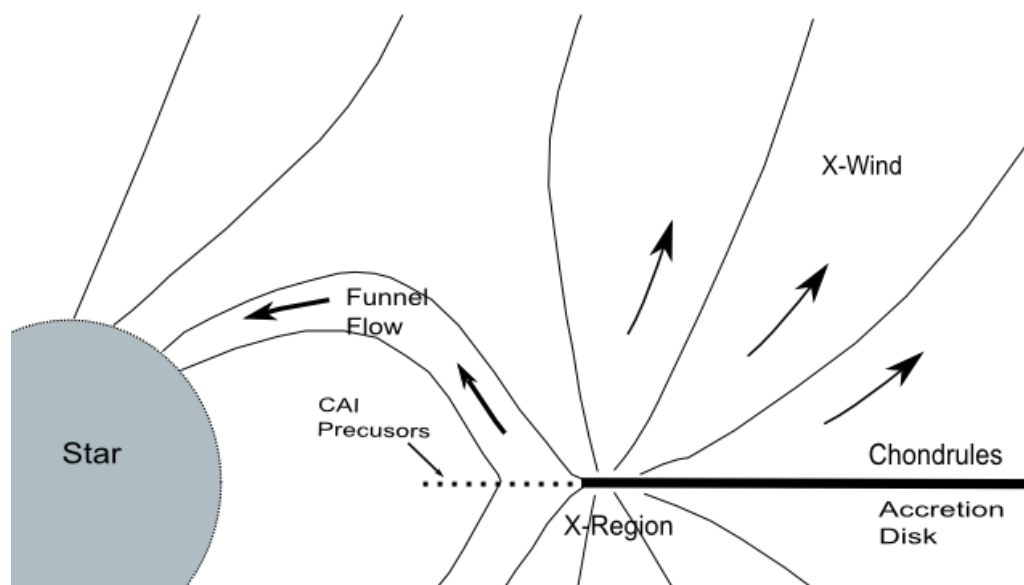
Figure 1.12. The X-wind model. CAIs formed in the reconnection ring at ~0.6 AU while chondrules formed at 1-20 AU. Diagram adapted from Krot et al. 2009.

Due to the variety of sizes, mineralogies, occurrences and shapes of CAIs, it has been

difficult to classify these materials. The most widely-used classification scheme for CAIs was

suggested by Grossman in 1975 who grouped CAIs as Type A or Type B based on mineralogy.

The additional CAI group Type C was later added by Wark (1987). Besides differences in

mineralogy, which will be explained in the next section, the groups of CAIs have some

differences in size, shape and occurrence.

Type A CAIs can range up to 2 cm or more in size but are usually smaller than Type B

CAIs. These inclusions are widespread occurring in carbonaceous (hence "C" in CV, CO, CR,

etc.) chondrites such as CV (Vigarano), CO (Ornans), CR (Renazzo), CM (Mighei), as well as

ordinary chondrites (Table 1.2). Type A CAIs are further subdivided into "fluffy" or "compact"

Type A CAIs based on texture. Fluffy Type A CAIs are found in CV chondrites and are

characterized by their contorted, irregular shapes. In many cases, fluffy Type A CAIs consist of

multiple nodules each surrounded with Wark-Lovering rims (described below) or sometimes

fine- grained matrix material. This class of Type A CAI can have grain sizes ranging from <50

μm to 1.5 mm. Compact Type A CAIs (Fig. 1.13a) have more regular shapes and tend to be

coarse grained with crystals up to 2 or 3 mm in size (Brearley & Jones 1998).

Table 1.2. CAI abundances in chondrites (r = rare, c = common, -- = absent (adapted from Scott & Krot 2003).

Object	CM	CO	CV	CR	CH	CB	CK
Melilite-rich (Type A)	r	c	c	c	c	c	--
Al,Ti-px-rich (Type B)	--	--	c	r	--	r	R
Fo-Type B CAIs	--	--	r	--	--	r	--
Plagioclase-Pyroxene-rich (Type C)	--	r	c	r	--	--	--

Note: CH = carbonaceous chondrites with high metal content, CB = Becubbin type carbonaceous chondrite, CK = Karoonda type carbonaceous chondrite.

Type B CAIs (Fig. 1.13b), unlike Type A CAIs, occur only in CV chondrites. These

inclusions can be >6-15 mm in size or larger and can vary in shape from spherical to subrounded

to irregular with vugs and vesicles. Such CAIs have complex histories including melting,

alteration, and capture of solid material while in a molten state (Brearley and Jones 1998).

Type C CAIs were classified by Grossman (1975) as intermediate between Type A and B

CAIs. This group of CAI tend to be larger than 2 mm in size and coarse-grained (Brearley and

Jones 1998). Three textural subgroups are recognized in Type C CAIs: coarse laths of anorthite,

ophitic textured equigranular anorthite and pyroxene, and fine-grained groundmass and pyroxene with a "lacy texture" (Wark 1987).
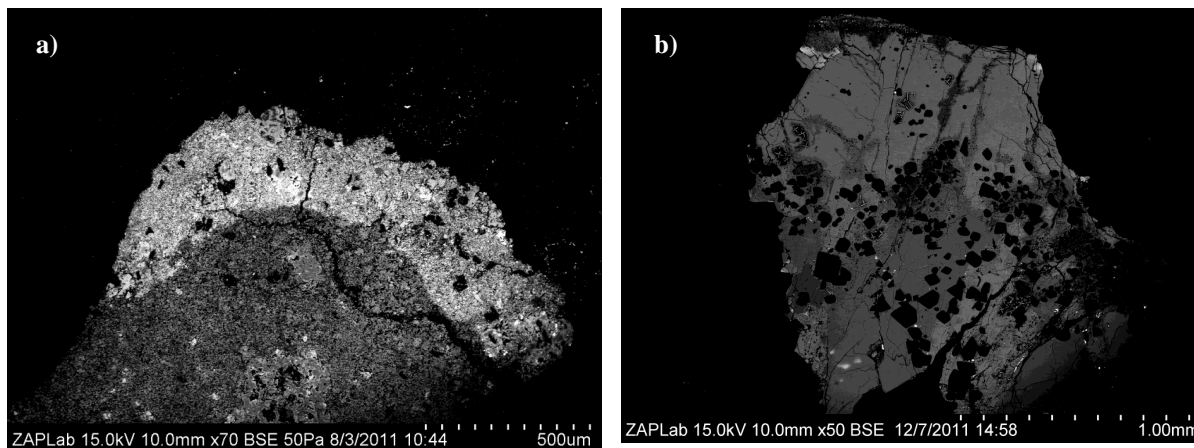
Figure 1.13. a) Type A and b) Type B CAI from the Allende meteorite. Images by Monika Haring.

An alternative way of classifying CAIs involves their trace element geochemistry. Based on trace element geochemistry, CAIs are classified as Group I, II, III, V, VI, or ultra refractory (Fig. 1.14) (Hutchinson 2004). Groups I, III, V, and VI are characterized by rare earth element (REE) abundance patterns that indicate little fractionation except for minor depletions or enrichments in volatile REE such as Eu or Yb. Unlike groups I, III, V, and VI, CAIs from group II and the ultra refractory group show progressive enrichments or depletions in REE.   The REE pattern of Group II CAIs shows little fractionation in moderately refractory, light REE (LREE) elements between Ce to Sm but depletions in volatile Eu and Yb and very refractory, heavy REE (HREE) from Gd to Lu. The REE pattern of ultra refractory group CAIs shows depletions in moderately refractory LREE between Ce and Sm and volatile REE such as Eu and Yb but enrichment in HREE from GD to Lu. This classification scheme works for both fine - grained and coarse - grained CAIs (Hutchinson 2004).
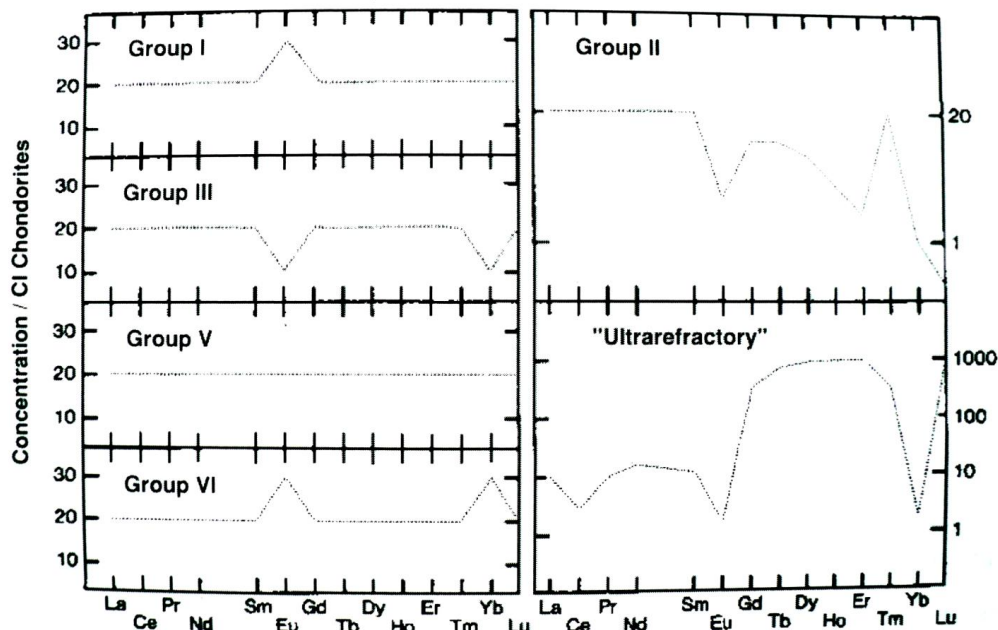
Figure 1.14. Classification of CAIs based on REE abundances. Figure adapted from Hutchinson 2004.

1.3.1. Mineralogy

CAIs are mineralogically and chemically diverse objects as is reflective of their complex histories which include multiple heating events and accretion into chondritic parent bodies. The primary mineralogy of CAIs includes Ca, Al, Ti, and Mg bearing silicates and oxides such as: corundum (Al_2O_3), hibonite ($CaAl_{12}O_{19}$), grossite ($CaAl_4O_7$), perovskite ($CaTiO_3$), melilite ($Ca_2Al_2SiO_7$-$Ca_2MgSi_2O_7$), spinel ($MgAl_2O_4$), olivine (Mg_2SiO_4), plagioclase, as well as three types of pyroxene including fassaite ($Ca(Mg,Al)(Si,Al)_2O_6$), rhönite, and diopside ($CaMgSi_2O_6$) (Brearley & Jones 1998). These primary phases are highly refractory and have condensation temperatures above 1300 K (Fig. 1.15) as modelled by Grossman 1972. It is important to note however, that in some CAIs the primary phases present did not necessarily form by condensation processes but instead crystallization of a melt (Brearley and Jones 1998). As the CAI cools, the higher temperature primary phases become unstable and undergo reactions with the nebular gas

to form lower temperature primary phases. For example, corundum has the highest condensation temperature of the primary phases listed above but upon cooling it reacts with nebular gas to form hibonite which is stable at lower temperatures, and as such corundum is rare is most CAIs (MacPherson 2003). In addition to common primary phases, some CAIs may contain accessory phases including refractory elements such as platinum group elements, sulfides such as troilite and millerite, cordierite, hercynite-rich spinel, and coulsonite (Brearley and Jones 1998).
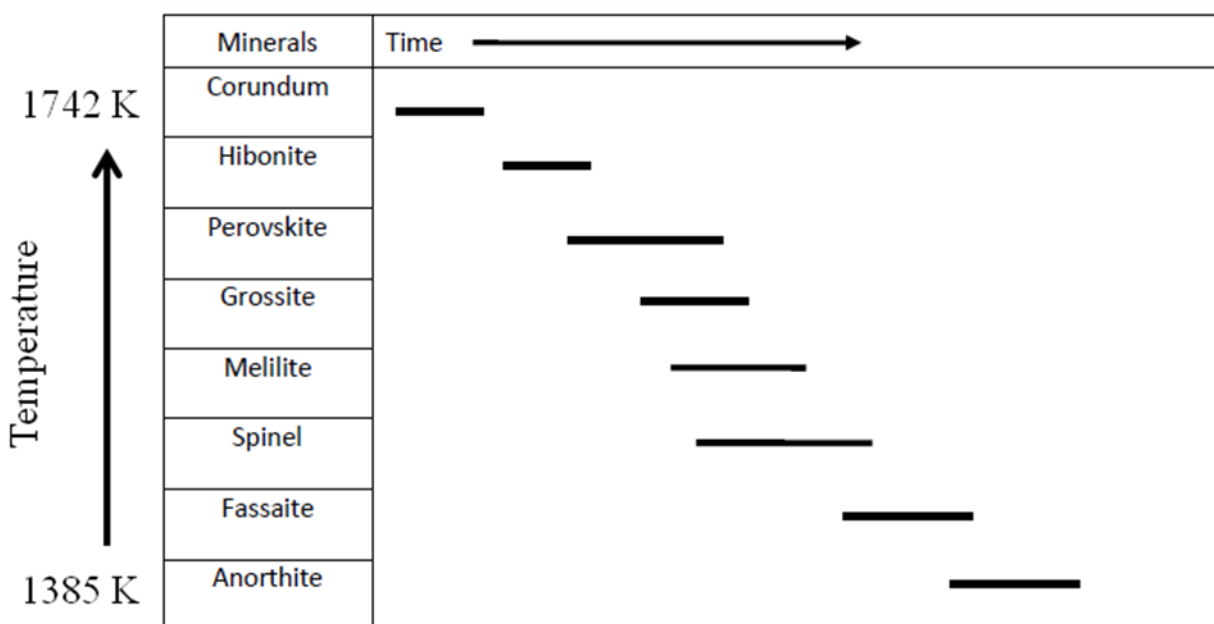
Figure 1.15. Condensation sequence for CAIs synthesized from Lauretta and McSween Eds (2006) and Brearley & Jones (1997).

The proportions of the primary phases listed above can vary between CAIs and for this reason CAIs can be classified according to primary mineralogy. Grossman (1975) divided CAIs into "coarse-grained" and "fine-grained" based on how readily observable the CAI components were under a petrographic microscope (Scanning electron microscope is needed to observe components in fine grained CAIs) (Hutchinson 2004). The CAIs were further subdivided into "Type A" and "Type B" groups based on mineralogy. An additional group of coarse-grained CAI, "Type C", was recognized by Wark (1987). Type A CAIs have a low abundance of clinopyroxene and a high abundance of melilite compared to Type B and Type C CAIs. Type B CAIs are characterized by an abundance (30-60 vol%) of fassaite (Al, Ti – rich clinopyroxene), coarse grained anorthite, spinel, as well as some melilite. This group is further subdivided into Type B1s which have melilite mantles and Type B2s which don't. A third less common subgroup is Type B3 CAIs which are less refractory and forsterite-bearing. Finally, Type C CAIs are characterized by an abundance of plagioclase (~ 60-70 vol%). Plagioclase in Type C CAIs is essentially pure anorthite and is often intergrown with fassaite (Brearley & Jones 1998).

Besides use in classification, primary minerals in CAIs can provide useful insights into the formation conditions of the CAIs. Titanium bearing primary minerals such as fassaite have been found to contain titanium in both the Ti^{4+} and Ti^{3+} valence states making them useful indicators of oxidation state. Beckett (1986) showed experimentally that the Ti^{3+}/Ti^{4+} ratios measured in natural Type B1 fassaite required highly reducing conditions (Beckett 1986). Measurements from the B1 fassaite suggest that CAIs formed in a nebular gas with C/O ~0.86, indicating that oxygen fugacity in the solar nebula was very low (MacPherson 2003). Highly reducing conditions in the solar nebula have also been inferred from Ti-bearing hibonite but more oxidizing compared to inferences based on fassaite (Ihinger & Stopler 1986).

CAIs are not all the primitive objects they were once thought to be. They have undergone multiple thermal events and incorporation into parent bodies such that after the crystallization of primary phases, some CAIs show evidence for secondary alteration. Secondary alteration is commonly found in CAIs from oxidized CV chondrites such as Allende and Axtel but is less common in reduced CV chondrites such as Leoville, Vigarano, and Efremovka. The common secondary minerals include nepheline, sodalite, grossular, andradite, wollastonite, hedenbergite, diopside, salite, and anorthite. Of these phases, nepheline is the most widespread and it is often found replacing melilite along with sodalite, grossular, and anorthite (Brearley & Jones 1997). Anorthite and diopside also occur as primary phases, however, secondary anorthite and diopside are more fine-grained. Besides being more fine-grained, secondary anorthite often shows a replacement relationship with melilite (Brearley and Jones 1998).

Table 1.3. Minerals in CAIs and Their Formulas, Paragenesis and Occurrence. Information compiled from Brearley & Jones 1997 and MacPherson 2003. Note: r = rare, lc = less common, c = common, and * = accessory phase

Mineral	Formula	Paragenesis	Occurrence
Andradite	$Ca_3Fe_2(SiO_4)_3$	Secondary	lc
Cordierite*	$Mg_2Al_4(Si_5O_{18})$	Primary	r
Corundum	Al_2O_3	Primary	lc
Coulsonite*	FeV_2O_4	Primary	r
Diopside	$CaMg(Si_2O_6)$	Primary and/or Secondary	c
Fassaite	$Ca(Mg,Al,Ti)(Si,Al)_2O_6$	Primary	c
Grossite	$CaAl_4O_7$	Primary	lc
Grossular	$Ca_3Al_2(SiO_4)_3$	Secondary	c
Hedenbergite	$CaFe(Si_2O_6)$	Secondary	r
Hercynite*	$FeAl_2O_4$	Primary	r
Hibonite	$Ca(Al,Ti,Mg)_{12}O_{19}$	Primary	c
Melilite	$Ca_2(Al,Mg)(Si,Al)_2O_7$	Primary	c
Millerite*	NiS	Primary	lc
Nepheline	$(Na,K)AlSiO_4$	Secondary	c
Olivine var. Fayalite	Fe_2SiO_4	Secondary	lc
Olivine var. Forsterite	Mg_2SiO_4	Primary	c
Perovskite	$CaTiO_3$	Primary	c
Plagioclase var. Anorthite	$CaAl_2Si_2O_8$	Primary and/or Secondary	c
Rhönite	$Ca_2(Mg,Ti)_6(Si,Al)_6O_{20}$	Primary	lc
Salite	(See Diopside)	Secondary	lc
Sodalite	$Na_8Al_6Si_6O_{24}Cl_2$	Secondary	c
Spinel	$MgAl_2O_4$	Primary	c
Troilite*	FeS	Primary	lc
Wollastonite	$CaSiO_3$	Secondary	lc

1.3.2. Geochemistry

Important clues as to the conditions of CAI formation are recorded by the trace element compositions and oxygen isotope compositions. Many CAIs are inferred to have formed from condensation in the solar nebula. Strong evidence for a condensation origin comes from type II rare earth element (REE) patterns exhibited by ~ 30% of all CAIs (Ireland & Fegley 2000). A type II REE pattern is characterized by a low abundance of heavy REEs such as Gd, Er and Lu,

such a pattern requires the prior removal of ultra refractory elements (Fig. 1.16) (Scott & Krot 2003). Other CAIs are inferred to be residues left over from the evaporation of presolar material. Evidence for this process comes from isotopic anomalies of ^{48}Ca and ^{50}Ti in platy hibonites from CM chondrites (Ireland & Fegley 2000).
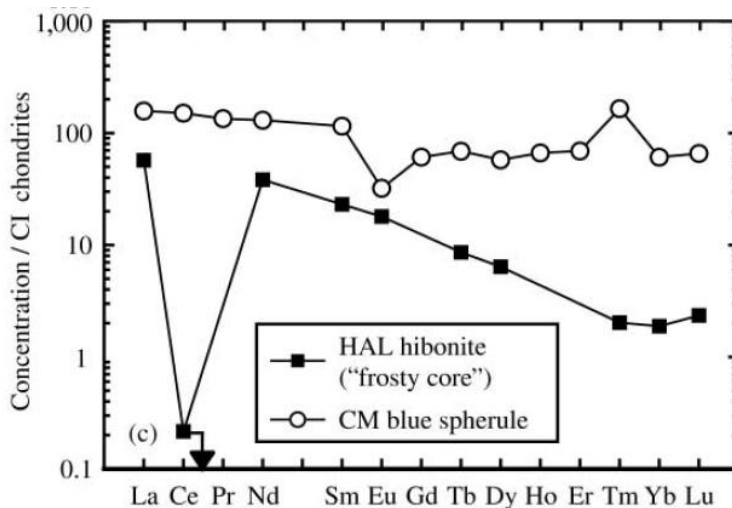
Figure 16. Type II REE pattern ,with characteristic HREE depletion, observed in CAIs (HAL = **H**ibonite **AL**lende. Figure adapted from MacPherson 2003.

Oxygen isotope abundances provide important constraints on the origin of CAIs. The ^{16}O-rich compositions of CAIs first discovered by Clayton et al. 1973, were for a long time attributed to presolar grains, however, ^{16}O-rich presolar grains preserved in CAIs have yet to be discovered (MacPherson et al. 2003). For this reason ^{16}O enrichment in CAIs is thought by many authors, including Clayton 2002, to be the result of mass independent fractionation processes in the early solar nebula. The oxygen isotope compositions of CAIs tend to fall on the carbonaceous chondrite anhydrous minerals (CCAM) mixing line (See Fig. 1.17), suggesting that CAIs sampled the same single ^{16}O-rich reservoir having a composition of δ^{18}O ~ δ^{17}O ~ -50‰ to -60‰ (MacPherson 2003; Guan et al. 2000). This ^{16}O-rich reservoir is thought to be the nebular

gases in which the CAIs formed and equilibrated based on oxygen isotopic studies of magnesian

olivines interpreted to be primary nebular condensates (MacPherson et al. 2003).
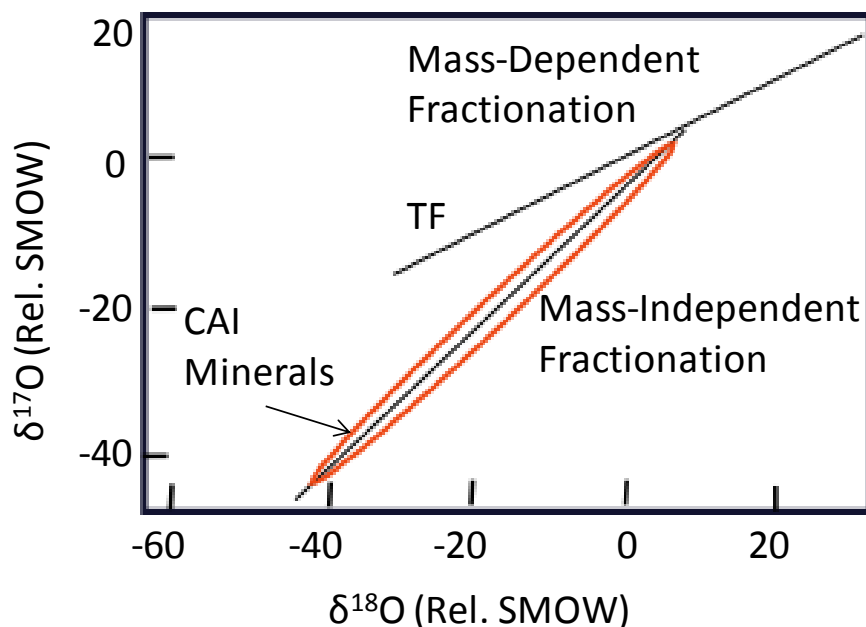
Figure 1.17. Oxygen isotopic compositions of CAI minerals (i.e. spinel, pyroxene, anorthite, melilite) plotted on a three isotope diagram. Both axes are given in delta notation (i.e. $\delta^{18}O = [((^{18}O/^{16}O)_{sample}/(^{18}O/^{16}O)_{standard})-1]x1000$). Diagram adapted from McSween & Huss 2010.

Because CAIs from different chondrite groups have variations in mineralogy and isotope

chemistry, it is possible that CAI formation took place at different times in the CAI formation

region under various physiochemical conditions (i.e. gas/dust ration, peak temperature, cooling

rate, etc.) (Scott & Krot 2003). Although most CAIs have similar oxygen isotope compositions,

there are oxygen isotope variations within single CAIs. In CAIs from CV chondrites; spinel,

hibonite, and pyroxene are ^{16}O enriched whereas melilite and anorthite are ^{16}O depleted (Scott &

Krot 2003). Furthermore, some igneous CAIs from Allende and Efromovka contain both ^{16}O

enriched and ^{16}O depleted melilite, anorthite, and fassaite as well as fassaite with ^{16}O zonation

(Scott & Krot 2003). These observations suggest that CAIs from CV chondrites were initially

[16]O rich and underwent subsequent oxygen isotope exchange(s) with a nebular gas depleted in

[16]O while partly molten (Fagan et al. 2002a). In CO chondrites, the oxygen isotope compositions

are a function of thermal metamorphism. Spinel, hibonite, melilite, diopside, anorthite, and

olivine from most CAIs in CO 3.0 are [16]O enriched whereas melilite and secondary nepheline

from more metamorphosed (Table 1.4) CO chondrites (i.e. Kainaz (CO 3.2) and Ornans (CO

3.2)) are [16]O depleted relative to spinel and diopside (Scott & Krot 2003).

Table 1.4. Petrologic Classification of Carbonaceous Chondrites (Table after McSween 1999).

Petrologic Types					
1	2	3	4	5	6
Aqueous Alteration ⟵				⟶ Thermal Metamorphism	
CI1					
	CM2				
	CR2				
		CV3			
		CO3			
			CK4		

This observation suggests that oxygen isotope exchange is due to fluid-rock interaction, possibly

in an asteroidal setting (Scott & Krot 2003). Finally, isotope compositions in CAIs from CR, CH

(High metal content), CB (Becubbin), CM, Ordinary, and enstatite chondrites are fairly uniform

with oxygen isotope compositions falling within 3-4 ‰ (Scott & Krot 2003). Some CAIs from

primitive CH, CR, and CB show a depleted but still uniform oxygen isotope composition as well

as igneous textures, suggesting that oxygen isotope exchange took place during melting (Scott &

Krot 2003).

The geochemical characteristics discussed above describe most CAIs, however, a group of CAIs known as FUN CAIs have a more anomalous geochemistry. FUN CAIs are rare inclusions occurring in CV and CM chondrites as well as Djhala and H3. They are characterized by Fractionation and Unidentified Nuclear (FUN) isotopic anomalies such as enrichment in neutron rich isotopes including ^{48}Ca and ^{50}Ti (Hutchinson 2004). The exact definition of FUN inclusion, however, has become blurred as there are inclusions have large nuclear anomalies but no mass dependent fractionation (UN CAI) or vice versa (F CAI) (MacPherson 2003). One feature present in all FUN inclusions, however, is that they have little or no excess ^{26}Mg (the decay product of ^{26}Al), indicating that FUN inclusions had little or no ^{26}Al (MacPherson 2003). One controversial explanation for the lack of ^{26}Al in FUN inclusions could be that FUN inclusions formed or were reprocessed later than normal CAIs, if ^{26}Al is assumed to have been evenly distributed in the solar nebula. This explanation however, difficult to reconcile with the large presolar isotopic anomalies preserved in FUN inclusions (MacPherson et al. 2003). Alternatively, if ^{26}Al was not uniformly distributed in the solar system, FUN inclusions formed in isotopically distinct reservoirs separate from regular CAIs.

Another important geochemical characteristic of FUN inclusions is the anomalous oxygen isotope fractionation. Unlike normal CAIs that have undergone mass-independent fractionation, FUN inclusions have undergone mass-dependent fractionation and their oxygen isotopic compositions fall off the CCAM line (Fig. 1.18). The data in Fig. 1.18 suggest that FUN CAIs once had a ^{16}O-rich composition similar to normal CAIs but this composition later evolved through melt distillation and Raleigh-type isotope fractionation to produce a slope-1/2 array (approximated by Line A in Fig. 1.18) (Clayton et al. 1984). Subsequent exchange with a ^{16}O-poor gas resulted in oxygen isotopic compositions occurring above line A (MacPherson et al.

1984). Ion microprobe analysis of individual phases such as olivine, pyroxene, and spinel in a

FUN CAI from Vigarano shows that their isotopic compositions (Line B in Fig. 1.18) follow

Line A, supporting the melt distillation and Raleigh fractionation hypothesis of Clayton et al.

1984.
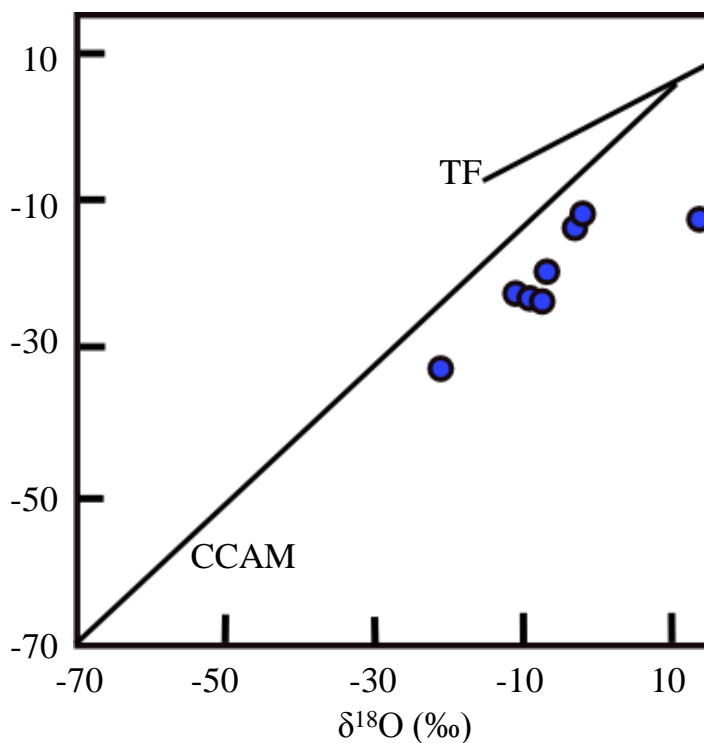
Figure 1.18. Oxygen isotope plot of CV3 FUN and F CAIs. CCAM is the carbonaceous chondrite amorphous mineral mixing line, TF is terrestrial fractionation. Figure adapted from MacPherson et al. 2003.

1.3.3. Textures

Many CAIs, particularly in CV chondrites, have distinct rims ~ 20-50 μm thick. These

rims are known as Wark – Lovering rims after Wark and Lovering who in 1977 first described

rims surrounding CAIs from the Allende CV chondrite (Fig. 1.19) (MacPherson 2003). Wark-

Lovering rims consist of thin (5-10 μm), multilayered bands each with a different mineralogy

(Brearley & Jones 1998). An idealized mineralogy for Wark-Lovering rims is as follows:

- Innermost layer: spinel + perovskite +/- hibonite +/- fassaite

- Melilite or its alteration products + anorthite +/- nepheline +/- sodalite

- Pyroxene that changes from fassaite to Al-diopside outwards through the rim

- Outermost: hedenbergite +/- andradite or olivine +/- spinel

(Brearley and Jones 1998)

Figure 1.19. Image could not be Wark-Lovering sequence around a Type A CAI in Vigarano (Al-diop = Al-Diopside, Hib = Hibonite, Mel = Melilite, Sp = spinel, Pv = perovskite, Fo = forsterite, Kir = Kirschtenite, Mtx = Matrix). Figure adapted from Krot et al. 2009.
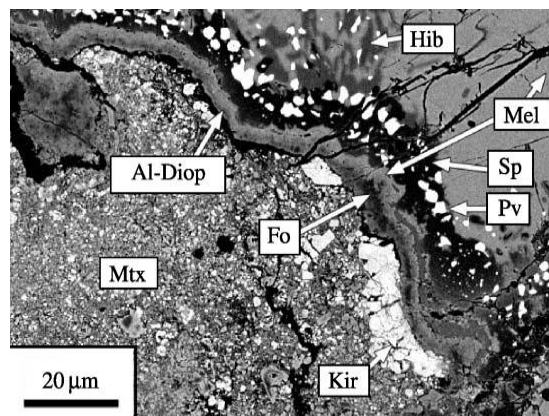
Although the mineralogy and complexity of Wark-Lovering rims is variable their structures tend to have these features: 1) they consist of one or more mono- or bi-mineralic layers; 2) the layers maintain a fairly constant thickness even on irregularly shaped CAIs; 3) fractures are continuous through CAIs and rims. The latter structural feature suggests that the rims did not form from within the chondrite matrix (MacPherson 2003).

The mineralogical sequences of Wark-Lovering rims are different for the different types of CAIs implying that are differences in how the types of CAIs are processed. There is still uncertainty as to the origin of Wark-Lovering rims. Wark and Lovering (1977) suggested that the layers within the rims reflect successive condensation events in the solar nebula. The presence of refractory elements that occur in both the rims and the host CAI support such a

theory (Brearley and Jones 1998). An alternative theory by MacPherson et al. (1981) is that

Wark-Lovering rims represent different degrees of alteration of the host inclusion.

References

Abragam, A. (1961) *The Principles of Nuclear Magnetism*, Clarendon Press, Oxford.

Amelin Y., Krot A. N., Hutcheon I. D. and Ulyanov A. A. (2002) *Lead isotopic ages of chondrules and calcium–aluminum-rich inclusions*. Science, **Vol.** 297, 1678-1683.

Bouvier, A. and Wadhwa, M. (2010) *The age of the Solar System redefined by the oldest Pb-Pb age of a meteoritic inclusion*. Nature Geoscience, **Vol.** 3, 637-641.

Bovey, F.A. (1987) *Nuclear Magnetic Resonance Spectroscopy*, Academic Press, New York.

Brearley, A.J. & Jones, R.H. (1998) *Chondritic Meteorites*. Rev. Min., **Vol.** 36, Chapter 3.

Connelly J. N., Amelin Y., Krot A. N. and Bizzarro M. (2008) *Chronology of the Solar System's oldest solids*. Astrophys. J., **Vol.** 675, L121-L124.

Clayton, R.N. (2002) *Self-Sheilding in the solar nebula*. Nature, **Vol.** 415, 860-861.

Clayton, R.N., MacPherson, G.J., Hutcheon, I.D., Davis, A.M., Grossman, L., Mayeda, T.K., Molini-Velsko, C., and Allen, J.M. (1984) *Two Forsterite-bearing FUN inclusions in the Allende Meteorite*. Geochim. Cosmochim. Acta., **Vol.** 48, 535-548.

Clayton, R.N., Grossman, L., and Mayeda, T.K., (1973) *A component of the primitive nuclear composition in carbonaceous chondrites*. Science, **Vol.** 182, 485-488.

Deer, W.A., Howie, R.A. and Zussman, J. (1978) *Rock-Forming Minerals: Single Chain Silicates 2nd edition*, **Vol**. 2A, Longman Group Ltd. pp 399-414.

Dowty, E., & Clark, J.R. (1973) *Crystal Structure Refinement and Optical Properties of a Ti^{3+} Fassaite from the Allende Meteorite*. Am. Min., **Vol.** 58, 230-242.

Duer, M.J. (2002) *Solid-State NMR Spectroscopy: Principles and Applications*, Blackwell Science, Oxford.

Ernst R.R., Bodenhausen G. and Wokaun, A. (1987) *Principles of Nuclear Magnetic Resonance in One and Two Dimensions*, Claredon Press, Oxford.

Fagan T. J., Yurimoto H., Krot A. N. and Keil K. (2002a) *Contrasting oxygen isotopic evolution of fine and coarse refractory inclusions from the CV3 Efremovka*. NIPR Antarct. Symp. Meteorit., **Vol.** 27, 15-17.

Fyfe, C.A. (1983) *Solid State NMR for Chemists*, CFC Press, Guelph.

Frydman, L. and Harwood, J.S. (1995) *Isotropic Spectra of Half-Integer Quadrupolar Spins from Bidimensional Magic-Angle Spinning NMR*. J. Am. Chem. Soc., **Vol.** 117, 5367-5368.

Grant, D.M. and Harris, R.K. (1996) *Encylcopedia of Nuclear Magnetic Resonance*, Wiley, New York.

Grossman, L. (1975) *Petrography and mineral chemistry of Ca-rich inclusions in the Allende meteorite.* Geochimica et Cosmochimica Acta, **Vol.** 39, 433-454.

Grossman, L. (1972) *Condensation in the primitive solar nebula*. Geochimica et Cosmochimica, Acta, **Vol.** 49, 2433-2444

Guan Y., McKeegan K. D. and MacPherson G. J. (2000) *Oxygen isotopes in calcium–aluminum-rich inclusions from enstatite chondrites: new evidence for a single CAI source in the solar nebula*. Earth Planet. Sci. Lett., **Vol.** 181, 271-277.

Hutchinson R. (2004) *Meteorites: A Petrologic, Chemical and Isotopic Synthesis*. Cambridge University Press. pp 75-84.

Ihinger P. D. and Stolper E. (1986) *The color of meteoritic hibonite: an indicator of oxygen fugacity*. Earth Planet. Sci. Lett., **Vol.** 78, 67-79.

Ireland T. R. and Fegley B., Jr. (2000) *The solar system's earliest chemistry: systematics of refractory inclusions*. Int. Geol. Rev., **Vol.** 42, 865-894.

Kirkpatrick, J. (1988) *MAS NMR Spectroscopy of Minerals and Glasses*. Rev. Min., **Vol.** 18, 341.

Kentgens, A.P.M. (1997) *A Pratical Guide to Solid-State NMR of half Integer Quadrupolar Nuclei with Some Applications to Disordered Systems*. Geoderma, **Vol.** 80, 271-306.

Krot A. N., Amelin Y., Cassen P. and Meibom A. (2005a) *Young chondrules in CB chondrites from a giant impact in the early Solar System*. Nature **Vol.** 436, 989–992.

Krot, A.N. et al. (2004) *Amoeboid olivine aggregates and related objects in carbonaceous chondrites : records of nebular and asteroid processes*. Chemie der Erde, **Vol.** 64, 185-239.

Krot, A.N. et al. (2009) *Origin and chronology of chondritic components: A review*. Geochimica et Cosmochimica Acta , **Vol.** 73, 4963-4997.

Lauretta, D.S. and McSween, H.Y. (2002) *Meteorites and the Early Solar System II*. University of Arizona Press.

MacPherson G. J. and Grossman L. (1981) *A once-molten,coarse-grained, Ca-rich inclusion in Allende*. Earth Planet. Sci. Lett., **Vol.** 52, 16–24.

Macpherson, G.J. (2003) *Calcium – Aluminum-rich Inclusions in Chondritic Meteorites. Treatise on Geochemitsry1*, 201-246 Elsevier Pergamon.

McSween, H.Y. and Huss, G.R. (2010) *Cosmochemistry*. Cambridge University Press.

McSween, H.Y. (1999) *Meteorites and Their Parent Planets 2nd edition*. Cambridge University Press.

Medek, A., Harwood, J.S., and Frydman, L. (1995) *Multiple-Quantum Magic-Angle Spinning NMR: A New Method for the Study of Quadrupolar Nuclei in Solids*. J. Am. Chem. Soc., **Vol.** 117, 12779-12787.

Mehring, M. (1980) *Principles of High-Resolution NMR in Solids, 2nd ed.*, Springer-Verlag, Heidelberg.

Peacor, D.R. (1967) *Refinement of the Crystal Structure of a Pyroxene of Formula $M_IM_{II}(Si_{1.5}Al_{0.5})O_6$*. Am. Min. **Vol.** 52, 31-41.

Phillips, B.L., Allen, F.M., and Kirkpatrick, J.R. (1987) *High-resolution Solid-state ^{27}Al NMR spectroscopy of Mg-rich Vesuvianite.* Am. Min., **Vol.** 72, 1190-1197.

Sanders, J.K.M. and Hunter B.K. (1987) *Modern NMR Spectroscopy: A Guide for Chemists*. Oxford University Press.

Sani, A., Delmotte, L., Marichal, C., Gabelica, Z., and Forte, C. (2001) *^{29}Si, ^{27}Al, and ^{23}Na MAS NMR Study of the natural zeolite barrerite and its dehydrated phases*. Eur. J. Mineral., **Vol.** 13, 101 -111.

Scott, E.R.D. and Krot, A.N. (2003) *Chondrites and their Components*. Treatise on Geochemitsry1, 143-200 Elsevier Pergamon.

Shu F. H., Shang H., Gounelle M., Glassgold A. E. and Lee T. (2001) *The origin of chondrules and refractory inclusions in chondritic meteorites*. Astrophys. J., **Vol.** 548, 1029-1050.

Shu F. H., Shang H., Glassgold A. E. and Lee T. (1997) *X-rays and fluctuating x-winds from protostars*. Science, **Vol.** 277, 1475-1479.

Slichter C.P., (1990) *Principles of Magnetic Resonance, 3rd ed.*, Springer, Berlin.

Wark D. A. and Lovering J. F. (1977) *Marker events in the early solar system: evidence from rims on Ca–Al-rich inclusions in carbonaceous chondrites*. Proc. 8th Lunar Sci. Conf. 95-112.

Wark D.A., Boynton, W.V., Keays, R.R., and Palme, H. (1987) *Trace element and petrologic clues to the formation of forsterite – bearing Ca-Al-rich inclusions in the Allende meteorite*. Geochim. Cosmochim. Acta. **Vol.** 51, 607-622.

Chapter 2. Methods

2.1. Samples

TS62B

TS62B is a Type B1 CAI from the Allende CV meteorite and was provided by Dr.L. Grossman & Dr. S. Simon at the University of Chicago. This CAI is ~ 1 cm in diameter and consists of melilite, fassaite, anorthite, and spinel.
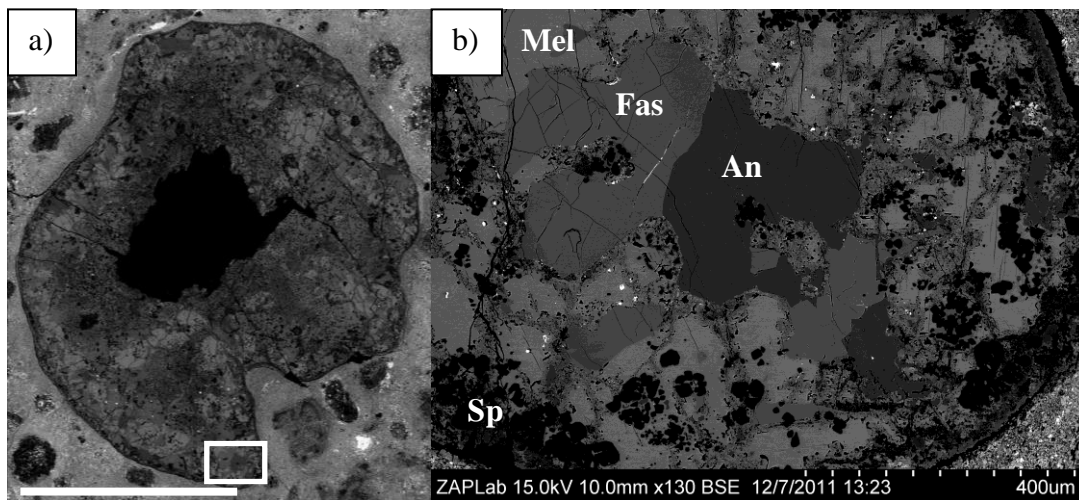
Figure 2.1. a) Electron back scatter image of Allende CAI TS62B with scale bar representing 4 mm. The dark region in the center of the CAI is where fassaite was removed. b) Close up enclosed area showing melilite (mel), fassaite (fas), anorthite (an),

USNM3529

USNM3529 is another type B CAI from the Allende CV meteorite as was provided by

Dr. T. McCoy at the Smithsonian. This CAI is ~ 5 mm in diameter and is coarse grained with

grain sizes ~ 0.5 mm in diameter. Similar to sample TS62B, the main phases in USNM3529

include melilite, fassaite, anorthite, and spinel.
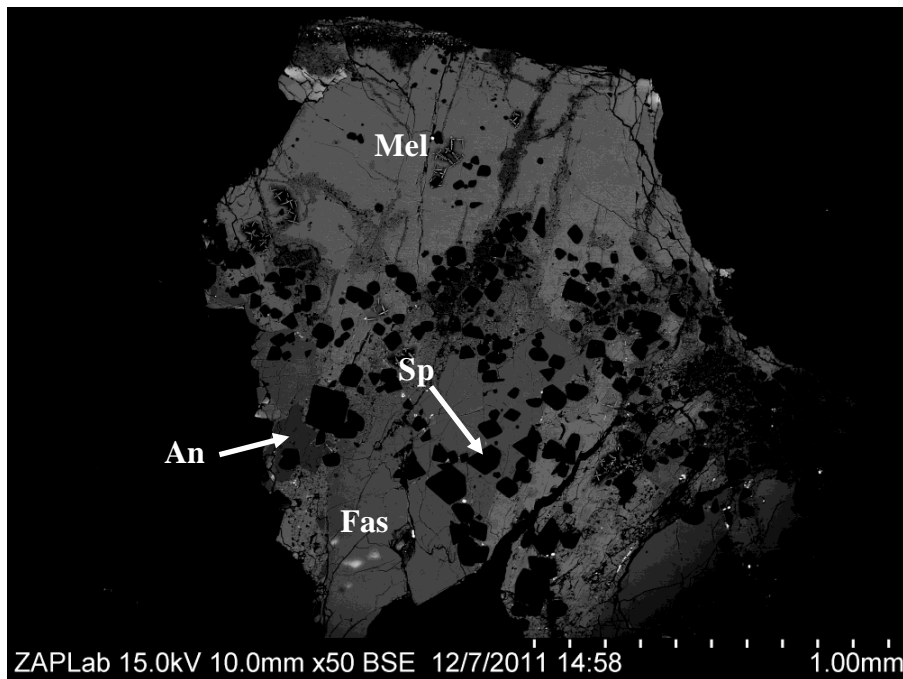
Figure 2.2. Electron back scatter image of Allende CAI USNM 3529 with phases including
melilite (mel), fassaite (fas), anorthite (an), and spinel (sp).

Fassa Valley Fassaite (M5964)

Fassa Valley Fassaite is a terrestrial fassaite from Fassa Valley in Italy, the type locality for this mineral. Approximately 50 mg of fassaite was provided by Dr. Kim Tait at the Royal Ontario Museum for this study. The Fassa Valley Fassaite sample is coarse grained with grain sizes between 1 to 5 mm in diameter.
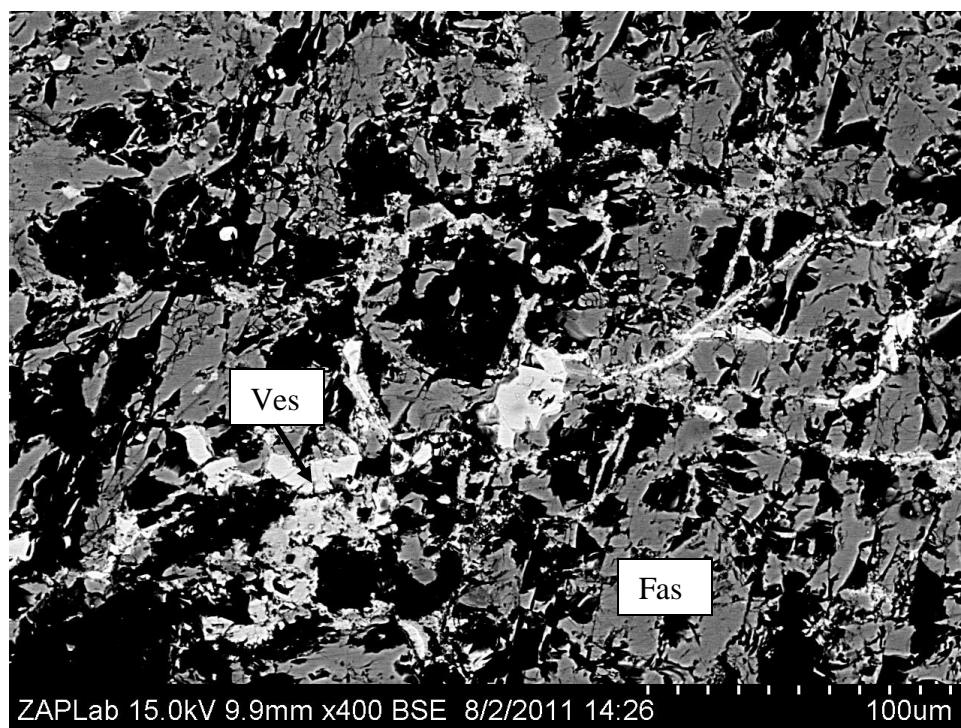
Figure 2.3. Electron sack scatter image of Fassa Valley fassaite where dark regions are voids, the grey phase is fassaite (fas), and the bright phase is vesuvianite (ves).

Table 2.1. Summary of Samples and Methods Used.

Sample Name	μ-XRD	SEM-EDS	EPMA	Single Crystal XRD	^{29}Si MAS NMR (600 MHz)	^{27}Al MAS NMR (600 MHz)	^{29}Si MAS NMR (900 MHz)	^{27}Al MAS NMR (900 MHz)	^{27}Al 3QMAS NMR (900 MHz)
Allende TS62B	✓	✓	✓	✓	N/A	N/A	✓	✓	✓
Allende USNM 3529	✓	✓	✓	✓	N/A	N/A	✓	✓	✓
IOM CAI 1	✓	✓	✓	N/A	✓	N/A	N/A	N/A	N/A
IOM CAI 2	✓	✓	✓	N/A	✓	N/A	N/A	N/A	N/A
Fassa Valley fassaite	✓	✓	✓	✓	✓	✓	✓	✓	✓

2.2 Micro-XRD

The purity of Fassa Valley fassaite was determined using a Bruker Discover micro X-ray diffractometer with theta-theta geometry (allowing a horizontal and stationary sample), with Co Kα radiation (λ = 1.7892 Å) and a nominal beam diameter of 300 μm operating at 35 KV and 45 mA. The data was collected using a 2dimensional Hi-star detector and General Area Detector diffraction system (GADDS) software, using two frames with 2θ at 37.5 and 70°, using a rotating optics method (omega scan) with rotation through 15 and 25° for the two frames, respectively. A total of eight points from Fassa Valley fassaite were X-rayed and the 2 dimensional X-ray patterns were integrated using GADDS (General Area Detector Diffraction System). Due to its coarse grained nature, the Fassa Valley fassaite sample had to be powdered before X-ray analysis to produce microcrystals which allow for the collection of a more representative X-ray pattern. Identification of fassaite in the USNM 3529 CAI was completed using the same experimental paramerters as Fassa Valley fassaite.   Similar to Fassa Valley fassaite, a total of eight points on the USNM 3529 CAI were X-rayed. The X-ray patterns of the two samples were integrated using GADDS and mineralogical identification was performed using the International Centre for Diffraction Data (ICDD), accessed via Bruker's EVA® interface. Micro – XRD analysis was not completed on CAI TS62B, as the fassaite was already identified and extracted by Drs. Simon and Grossman from the University of Chicago, who loaned us the sample for this study.

2.3 SEM-EDS

Initial qualitative chemical analysis of the Fassa Valley and Allende fassaite samples were performed on a Hitachi SU6600 Field Emisson Gun Scanning Electron Microscope (FEG-SEM) with a voltage of 15.0 KV (See Appendix 3).

2.4 EPMA

Final quantitative chemical analysis was collected, on carbon coated grain mounts, by Electron Probe Microanalysis (EPMA) using a JEOL JXA-733 Superprobe with an accelerating voltage of 15 KV and a beam current of 11 nA. The count times for major elements (e.g. Fe, Mg, Si, Ca) were 20 s on peak and 10 s (on each side) for background measurements. For trace elements (Ti, Ni, Mn, Na) both peak and background times were 50 s. A set of microbeam standards from SPI and natural minerals from the Smithsonian Institution were used for calibration (Jarosewich, 1980 and 2002). The standards used were Hot Springs Arizona quartz (Si), Ilmen Mountains ilmentite (Ti), synthetic corundum (Al), Tiebaghi Mine chromite (Cr), Ivigtut Greenland siderite (Fe), manganotantalite (Mn), Oberdorf Austria dolomite (Mg), microcline (K), calcite (Ca), and albite (Na). The elements Na, K, Mn, Fe, and Cr were sought but not detected in significant amounts (i.e. < 1 wt %).

2.5 Single Crystal XRD

X-ray intensity data were then collected for the samples using a Bruker Kappa Apex II single crystal diffractometer with Mo Kα radiation and a sample to detector distance of 4.0 cm. Crystals ~ 100 μm in diameter and displaying no twinning were selected from the terrestrial fassaite for intensity data collection. All reflections from the X-ray intensity data were then

merged using XPREP and a solution and structure refinement was determined using SHELX-97. The solution was determined using direct methods, with scattering curves and anomalous scattering factors from Cromer & Mann (1968) and Cromer & Liberman (1970).

2.6 MAS NMR and MQMAS NMR at 900 MHz

^{27}Al and ^{29}Si MAS NMR experiments at 21.1 T were performed on a Bruker Avance II NMR instrument (National Ultrahigh-Field NMR Facility for Solids, Ottawa, ON, Canada) using a 2.5 mm H/X MAS Bruker probe.

The ^{29}Si MAS NMR spectra of the Allende and Fassa Valley fassaite samples were recorded at a resonance frequency of 178.8 MHz employing a simple single-pulse sequence. A 90° radio frequency (RF) pulse of 4 μs was used with a relaxation delay time of 30 s. Relaxation delay times were determined using a relaxation delay test. The ^{29}Si MAS NMR experiments were calibrated with tetramethylsilane (TMS). A total of 3072 scans were acquired for Fassa Valley fassaite at frequency of 31.25 kHz while a total of 6144 scans were acquired for Allende 3529 sample at 31.25 kHz MAS, and 7524 scans were acquired for Allende CAI TS62B sample at 20 kHz MAS. All ^{29}Si NMR chemical shifts were referenced to external TMS at 0 ppm.

^{27}Al MAS NMR spectra were collected at a resonance frequency of 234.5 MHz using a single –pulse sequence with a spinning frequency of 31.25 kHz. A 90° pulse of 3 μs was used with a relaxation delay time of 1s for Fassa Valley fassaite and a relaxation delay time of 5s for Allende TS62B and USNM 3529 fassaite. The ^{27}Al MAS NMR experiments were calibrated using 0.5M aqueous solution of $AlCl_3$. A total of 4096 scans were acquired for Fassa Valley fassaite while 2048 scans were acquired for Allende TS62B and USNM 3529 fassaite. All ^{27}Al NMR chemical shifts were referenced to the 0.5 M aqueous solution of $AlCl_3$ at 0 ppm.

The 27Al 3QMAS NMR spectra were acquired for the Allende fassaite samples and Fassa Valley fassaite rotor were collected using spectral widths of 31.25 kHz or 62.50 kHz respectively in the F1 dimenstion. The spectral widths in the F2 dimension for Allende fassaite and Fassa Valley fassaite were 100 kHz and 200 kHz respectively. In all 3QMAS experiments P1 excitation pulse was 2.6 μs, P2 conversion pulse was 0.9 μs, and P3 90-degree soft selective pulse was 10 μs. For Fassa Valley fassaite, 8160 scans were acquired using 0.5 s relaxation delay. For Allende CAI TS62B sample, 2160 scans were accumulated using 2 s relaxation delay. Finally, for Allende CAI USNM 3529 sample 960 scans were accumulated using 2 s relaxation delay. Shearing transformation was used for processing of 3QMAS spectra.

References

Bruker AXS. (Bruker AXS, Karlsruhe, Germanu, 2005).

Cromer, D.T., and Liberman, D. (1970) *Relativistic calculation of anomalous scattering factors for X rays.* J. Phys. Chem., **Vol.** 53, 1891-1898.

Cromer, D.T., and Mann, J.B. (1968) *X-ray scattering factors computed from numerical Hartree-Frock wave functions.* Acta Crystallogr. **Vol.** A24, 321-324.

Flemming, R.L. (2007) *Micro X-ray Diffraction (μXRD): A versatile technique for characterization of Earth and planetary materials.* Canadian Journal of Earth Scien ICDD (2001). PDF-2 2001 (Database), International Centre for Diffraction Data, Newton Square, PA, USA.

Jarosewich (2002), Journal of Research of the National Institute of Standards and Technology, **Vol.** 107, Number 6, November-December 2002, pp. 681-685.

Sheldrick, G.M. (1997): SHELXL-97: *A computer program for the Refinement of Crystal Structures.* Univ. of Göttingen, Göttingen, Germany.

Chapter 3: ²⁹Si MAS NMR, ²⁷Al MAS NMR and ²⁷Al 3QMAS NMR Study of Al-Rich, Ti-bearing Diopside From Fassa Valley, Italy

Abstract

Al-,Ti-rich diopside, referred to in this paper as fassaite occurs in both terrestrial and extraterrestrial environments. Fassaite has a composition intermediate between diopside ($CaMgSi_2O_6$) and Ca-Tschermak pryroxene ($CaAl_2SiO_6$).   This study focuses on single crystal XRD and NMR spectroscopy of natural fassaite from Fassa Valley, Italy.   Fassa Valley fassaite has an average composition of $Ca_{1.02}(Mg_{0.69}Al_{0.15}Fe_{0.12}Ti_{0.02})_{\Sigma=0.98}(Si_{1.76}Al_{0.24})_{\Sigma=2}O_6$. The unit cell parameters from single crystal X-ray diffraction were determined to be a 9.753(2) Å, b 8.888(2) Å, c 5.286(1) Å, β 105.96(3)°, and V = 440.54(2) Å^3 with a space group of $C2/c$ which are consistent with the fassaite unit cell parameters from past studies. The ²⁹Si MAS NMR spectrum of Fassa Valley fassaite contains only a single broad asymmetric peak centered at ~85 ppm. The ²⁷Al MAS and 3QMAS NMR spectra contain two sets of peaks at ~80 to ~45 ppm and ~20 to ~-15 ppm corresponding to tetrahedral and octahedral peaks, respectively. Broad poorly-resolved peaks in the NMR spectra of Fassa Valley fassaite suggest that this sample has a disordered Al/Si cation arrangement, which is consistent with its $C2/c$ symmetry. The Al/Si disorder in Fassa Valley fassaite is likely a reflection of thermal equilibration at relatively high temperatures (above the order disorder transition temperature). A long-range-ordered fassaite has yet to be discovered in nature thus the order disorder transition temperature is unknown.

3.1 Introduction

Calcium - rich pyroxene is a single chain silicate mineral, ubiquitous in both terrestrial and extra terrestrial environments as is reflected by its stability over a wide range of temperatures and pressures. In this study, we focus on an aluminous calcic-pyroxene known as Al-rich Ti-bearing diopside which will be referred to as fassaite. Although the name "fassaite" has been discredited by the International Mineralogical Association (IMA), the name fassaite is used for brevity to describe Al-rich Ti-bearing diopside. Fassaite is a name first introduced to describe a light to dark green pyroxene from an augite syenite-limestone contact in Fassa valley, Trentino, Italy (Deer et al. 1987). Recently this name has been more often used to describe aluminum – rich and sodium – poor pyroxene usually occurring in metamorphosed limestones and dolomites as well as eclogitic inclusions from kimberlites (Deer et al. 1987, Benna et al. 1988). The structure of fassaite was determined by Peacor in 1967 from samples of a carbonatite complex in Oka, Quebec, Canada. Peacor (1967) determined the unit cell of fassaite to be *a* 9.794, *b* 8.906, *c* 5.319Å, and β 105.90° with spacegroup *C*2/*c*, similar to the unit cell of diopside. Besides octahedral Mg and Al, the crystal structure of fassaite may include additional cations in the octahedral site M1 such as Fe^{3+}, Fe^{2+}, Ti^{4+} resulting in a range of unit cell dimensions (Benna et al. 1988, Oberti et al. 1982, Coleman 1962).

An important solid solution, in calcium – rich clinopyroxene (General formula: XYT_2O_6) occurs between diopside ($CaMgSi_2O_6$) and Ca-Tschermak's molecule (CaTs) ($CaAl_2SiO_6$). Incorporation of Al into the diopside structure is due to Tschermak reactions such as (Si^{4+}) + $[Mg^{2+}] \leftrightarrow (Al^{3+})$ + $[Al^{3+}]$ where () is tetrahedrally coordinated and [] is octahedrally coordinated (Etzel, & Bensiek 2008, Etzel et al. 2007, Flemming & Pawsey 2007). Intermediate members of

this solid solution are referred to as fassaite ($Ca(Mg,Al)(Si,Al)_2O_6$) (Deer et al. 1987, Benna et al. 1988). Pyroxene containing only octahedral aluminum include jadeite ($NaAlSi_2O_6$) and omphacite ($(Ca,Na)(Mg,Al)Si_2O_6$) (Deer et al. 1987). Tschermak reactions may result in these pyroxenes having a considerable Tschermak component. The incorporation of Al into the structure of pyroxene is an important process as the amount of Al incorporated increases with temperature and pressure. For this reason aluminous pyroxene is useful in geobarometers and geothermometers (Flemming 2012).

Intermediate compositions in the diopside-CaTs solid solution, due to significant replacement in tetrahedral and octahedral sites by Al, have the potential for Si/Al and Mg/Al disordering. At high temperatures, pyroxene with a high CaTs component, has a $C2/c$ symmetry which implies complete disorder along the tetrahedral chain (Okamura et al. 1974). Upon cooling the crystal structure of the CaTs pyroxene undergoes a phase transition from $C2/c$ symmetry to lower symmetry. Four possible low symmetry space groups have been proposed including $C2$, $C1$, $P2/n$, or $P2_1/n$, where there is complete ordering along the tetrahedral chain (Okamura et al. 1974). A study by Bosenick et al. 2001 suggests that the transition between $C2/c$ and $P2_1/n$ occurs at 727 °C. No long-range ordered CaTs pyroxene samples discovered to date however, locally-ordered domains with the structure of CaTs pyroxene may exist (Cohen & Burnham 1985; Grove & Burnham 1974). In the crystal structure of fassaite, the replacement of Si by Al is between 0.25 and 0.50 per mole, making fassaite useful for Al/Si cation ordering studies (Deer et al. 1987).

Aluminum/silicon cation ordering on the tetrahedral chain may only be inferred indirectly from bond length variations when using X-ray methods. This is due to Si and Al having similar scattering behaviour such that they are indistinguishable by X-rays. Instead of X-ray techniques,

nuclear magnetic resonance (NMR) spectroscopy allows one to observe short-range ordering directly. Recent NMR techniques such as magic angle spinning nuclear magnetic resonance (MAS NMR) spectroscopy provide high resolution spectra of solids allowing for more accurate interpretations of cation ordering (especially Si ordering) in solids. A study by Flemming and Luth (2002) directly observed Si-Al ordering in synthetic aluminous pyroxene using ^{29}Si MAS NMR. Flemming and Luth (2002) also found that the ^{29}Si spectrum of the pyroxene was affected by Al substitution in the octahedral site. Therefore ^{29}Si MAS NMR may be used to indirectly observe the octahedral environment in pyroxene whereas ^{27}Al MAS NMR allows for direct observation of both tetrahedral and octahedral sites. In addition to ^{27}Al MAS NMR, ^{27}Al MQ (Multiple Quantum) MAS NMR may be used, since Al is a quadrupolar nuclei with I=5/2, to get additional information on site distortion. In this study we report crystal structure data of a terrestrial fassaite, from the type locality of Fassa Valley, Italy, by single crystal X-ray diffraction (XRD). In addition, we report cation ordering data of this fassaite sample, by ^{29}Si and ^{27}Al MAS NMR and ^{27}Al MQMAS NMR.

3.2 Methods

The purity of Fassa Valley fassaite was determined using a Bruker Discover micro X-ray diffractometer with theta-theta geometry (allowing a horizontal and stationary sample), with Co Kα radiation (λ = 1.7892 Å) and a nominal beam diameter of 300 μm operating at 35 KV and 45 mA. The data were collected using omega scan mode, using two frames with 2θ at 37.5 and 70̊ and omega angles of 15 and 25̊, respectively. A total of eight points from Fassa Valley fassaite were X-rayed and the 2 dimensional X-ray patterns were integrated using GADDS (General Area Detector Diffraction System). Mineral identification was performed using comparison to

the International Centre for Diffraction Data (ICDD) database. Due to its coarse grained nature, the Fassa Valley fassaite sample had to be powdered before X-ray analysis.

Initial qualitative chemical analysis was performed on a Hitachi SU6600 Field Emisson Gun Scanning Electron Microscope (FEG-SEM) with a voltage of 15.0 KV. Final quantitative chemical analysis was collected, on a carbon coated grain mount, by Electron Probe Microanalysis (EPMA) using a JEOL JXA-733 Superprobe with an accelerating voltage of 15 KV and a beam current of 11 nA. A set of microbeam standards from Structure Probe Inc. (SPI) and natural minerals from the Smithsonian Institution were used for calibration (Jarosewich, 1980 and 2002).

X-ray intensity data were then collected for the samples using a Bruker Kappa Apex II single crystal diffractometer with MoKα radiation and a sample to detector distance of 4.0 cm. Crystals ~ 100 μm in diameter and showing no twinning were selected from the terrestrial fassaite for intensity data collection. All reflections from the X-ray intensity data were then merged using XPREP and a solution and structure refinement was determined using SHELX-97. The solution was determined using direct methods, with scattering curves and anomalous scattering factors from Cromer & Mann (1968) and Cromer & Liberman (1970).

Table 3.1. Miscellaneous Data for Fassa Valley fassaite.			
a (Å)	9.753(2)	Monochromator	Graphite
b (Å)	8.888(2)	Intensity-data collection criterion for observed reflections	θ:2θ Fo> 4σ(Fo)
c (Å)	5.286(1)	GOF	1.293
β (°)	105.96(3)	Total No. of reflections	5343
Space Group	C2/c	No. Unique reflections	549
Z	2	R (%)	2.02
Diffractometer	Bruker Kappa Apex II	wR^2 %	6.94
Radiation	MoKα (50 KV, 40mA)		

The ^{29}Si and ^{27}Al MAS NMR spectra were collected on approximately 4 to 7 mg of Fassa Valley fassaite (packed in 2.5 mm MAS rotors), using a 21.1 T (^{1}H at 900 MHz) Bruker Avance II NMR Spectrometer at the National Ultrahigh - Field NMR Facility for Solids, in Ottawa, ON. For all NMR experiments, the fassaite sample was spun at a frequency of 31, 250 Hz. ^{29}Si spectra for the samples were collected using a 90° pulse width of 4.0 μs over a spectra width of 20 KHz. The ^{29}Si spectra for Fassa Valley fassaite involved acquisition of 3072 scans, with a relaxation delay time of 30 s between scans. Chemical shifts for ^{29}Si NMR spectroscopy were referenced to tetramethlysilane (TMS) (Si(CH$_3$)$_4$). ^{27}Al spectra for the samples were collected with a 90° pulse width of 0.5 μs over a spectral width of 200 KHz. The ^{27}Al spectra for Fassa Valley fassaite involved 4000 scans with a delay time of 1 s between scans. The ^{27}Al 3QMAS spectra for Fassa Valley fassaite involved acquisition of 8160 x 36 scans each with a relaxation delay time of 0.5 s. ^{27}Al 3QMAS NMR data was collected over a spectra width of 62.5 kHz. Chemical shifts for ^{27}Al NMR spectroscopy were referenced to 0.5 mol aqueous AlCl$_3$.

The ^{27}Al MAS NMR spectrum of the Fassa Valley sample was collected using spectral widths of 62.5 kHz respectively in the F1 dimension and spectral widths of 200 kHz in the F2

dimension. In all 3QMAS experiments P1 excitation pulse was 2.6 us, P2 conversion pulse was 0.9 us, and P3 90-degree soft selective pulse was 10 us. For Fassa Valley fassaite, a total of 8160 scans were acquired using 0.5s relaxation delay. Shearing transformation was used for processing of 3QMAS spectra.

3.3 Results

3.3.1 Electron Probe Micro Analysis (EPMA)

The average chemical composition of Fassa Valley fassaite is presented below in Table 3.2. From the average chemical composition, the empirical formula $Ca_{1.02}(Mg_{0.69}Al_{0.15}Fe_{0.12}Ti_{0.02})_{\Sigma=0.98}(Si_{1.76}Al_{0.24})_{\Sigma=2}O_6$ was derived for the fassaite sample. This chemical composition is broadly similar to Tschermak's substitution reactions between diopside and CaTs end-members, where the general formula for intermediate members is $\{Ca\}[Mg_{1-x}Al_x](Si_{2-x}Al_x)O_6$ (Flemming & Luth 2002) ($\{\}$ = 8 coordinated site, [] = octahedral site, () = tetrahedral site) . Cations were apportioned to the tetrahedral and octahedral sites by assuming the tetrahedral site contained all the Si as well as some Al such that the sum of cations in the tetrahedral site was equal to two. The remaining Al was placed in the octahedral site along with Mg, Fe, and Ti. If the ^{27}Al MAS NMR of Fassa Valley fassaite spectrum is assumed to be quantitative, roughly 51% of the Al is found in the tetrahedral site while 49% of the Al is in the octahedral site. The discrepancy between the EPMA data and the NMR spectra may be due to small amounts of vesuvianite in the sample contributing to the intensity of the octahedral Al peak.

Table 3.2. EPMA data (wt. % oxides) and Cations per Formula Unit					
	1	2	3	average	St. Dev.
SiO_2	48.46	48.73	45.9	47.70	1.56
TiO_2	0.69	0.77	0.9	0.79	0.11
Al_2O_3	8.00	9.07	10.31	9.13	1.16
Cr_2O_3	0.01	0.03	0.00	0.01	0.02
FeO_{tot}	3.72	3.75	4.43	3.97	0.40
MgO	12.98	12.03	12.94	12.65	0.54
MnO	0.06	0.00	0.02	0.03	0.03
K_2O	0.11	0.07	0.06	0.08	0.03
CaO	26.08	25.79	25.91	25.93	0.15
Na_2O	0.06	0.05	0.02	0.04	0.02
NiO	0.00	0.00	0.00	0.00	0.00
SUM	100.17	100.29	100.49	100.32	0.16
Si	1.79	1.79	1.70	1.76	0.04
Al_{tet}	0.21	0.21	0.30	0.24	0.04
Al_{oct}	0.14	0.18	0.15	0.15	0.01
Ti	0.02	0.02	0.03	0.02	0.00
Cr	0.00	0.00	0.00	0.00	0.00
Fe	0.12	0.12	0.14	0.12	0.01
Mn	0.00	0.00	0.00	0.00	0.00
Mg	0.71	0.66	0.71	0.70	0.03
Ca	1.03	1.01	1.03	1.02	0.01
K	0.01	0.00	0.00	0.00	0.00
Na	0.00	0.00	0.00	0.00	0.00
Ni	0.00	0.00	0.00	0.00	0.00
O	6	6	6	6	0.00

3.3.2 X-ray Diffraction (XRD)

Micro-XRD indicated that the Fassa Valley fassaite sample is nearly pure except for small amounts of vesuvianite (($Ca, Na)_{19}(Al, Mg, Fe^{3+})_{13}(B, Al, Fe^{3+})_5(Si_2O_7)_4(SiO_4)_{10}(OH, F,O)_{10}$) (Fig. 3.1 & 3.6). The relatively pure nature and large crystal size of the Fassa Valley fassaite sample made it ideal for single – crystal XRD. From single crystal XRD, Fassa Valley fassaite was found to be monoclinic with the Space Group *C*2/*c* and the unit cell dimensions as listed in Table 3. This result is consistent with past structure refinements of fassaite by Peacor (1967) and Dowty & Clark (1973) (Table 3.3).
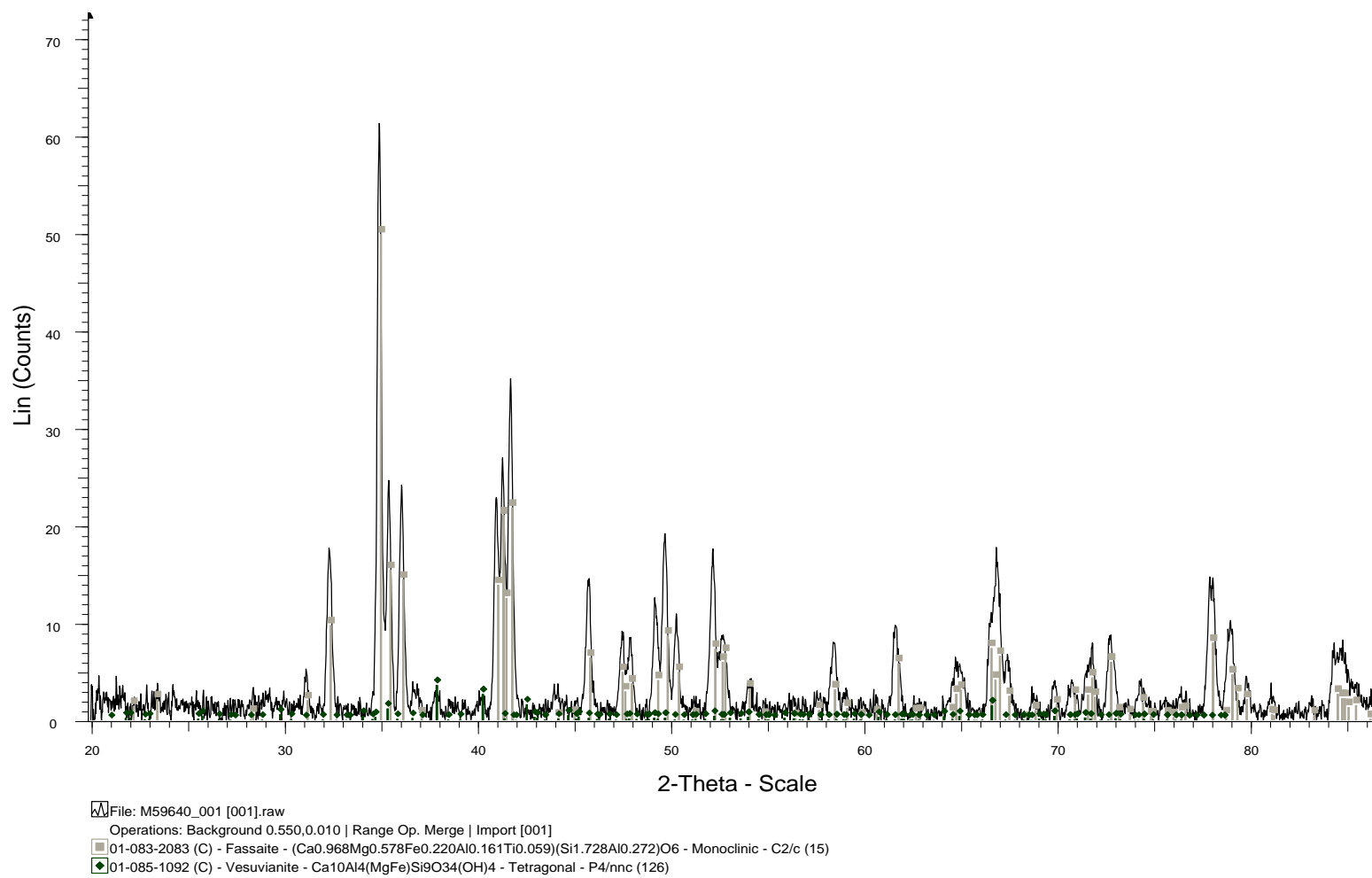
Figure 3.1. Micro-XRD pattern Fassa Valley fassaite (grey) with small amounts of vesuvianite (black). XRD pattern by Monika Haring.

The final error on the Fassa Valley fassaite structure solution converged to R = 2.02 % and wR2

= 6.94% with the residual electron density peaks on the Fourier map being less than $1e^-/Å^3$.

Table 3.3. Unit cell parameters of Fassa Valley Fassaite compared with past studies.			
	Fassa Valley Fassaite (this study)	Allende Fasasite (Dowty 1973)	Oka Quebec Fassaite (Peacor 1967)
a (Å)	9.753(2)	9.80(1)	9.794(5)
b (Å)	8.888(2)	8.85(1)	8.906(5)
c (Å)	5.286(1)	5.36(5)	5.319(3)
β (°)	105.96(3)	105.37(1)	105.90(3)
V (Å^3)	440.56(2)	448.25(1)	446.21(3)
Sym.	$C2/c$	C2/c	C2/c

In the crystal structure of Fassa Valley fassaite, individual sites were found for Ca, Mg,

and Si whereas three sites where found for oxygen (Table 3.4). During the initial refinement of

the crystal structure, the site occupancy factors (SOFs) for Mg and Si were found to be less than

the ideal SOFs of 0.5 and 1.0 respectively for those sites. This indicated the presence of

additional cations in the Mg and Si sites. From EPMA data (see above) Al and to a lesser extent,

Fe and Ti substitutes for Mg while significant amount Al substitutes for Si. Magnesium, silicon,

and aluminum are very close in atomic number and as such have similar scattering powers

making these elements difficult to distinguish from one another using X-ray methods. Since Mg,

Si and Al are difficult to distinguish using X-ray methods, the SOFs (Table 3.4) of the cations on

the Mg and Si sites were fixed based on EPMA results (Table 3.2). The additional octahedral

octahedral cations (Al1, Fe, and Ti) were refined into the Mg site using the "SUMP" command.

Using the SUMP command, the total occupancy of the octahedral site was fixed at one and the

site occupancy factors of Mg, Al1, Fe, and Ti were allowed to refine such that they summed to

one. The bond valence sums (Table 3.5) for the Ca, Mg, and Si cations as well as the O atoms

were found to be consistent with their respective charges.

Table 3.4. Atomic and Displacement Parameters for Fassa Valley fassaite

ATOM	x	y	z	SOF	U11	U22	U33	U23	U13	U12	Ueq
Ca	0	0.1965	1/4	1/2	0.0107	0.0062	0.0068	0	0.0004	0	0.0083
		0.0001			0.0003	0.0003	0.0003		0.0002		0.0002
Mg	0	0.5922	1/4	0.345	0.0081	0.0083	0.0074	0	0.0019	0	0.0080
		0.0001			0.0004	0.0004	0.0004		0.0003		0.0002
Al1				0.075	0.0081	0.0083	0.0074	0	0.0019	0	0.0080
					0.0004	0.0004	0.0004		0.0003		0.0002
Fe				0.06	0.0081	0.0083	0.0074	0	0.0019	0	0.0080
					0.0004	0.0004	0.0004		0.0003		0.0002
Ti				0.02	0.0081	0.0083	0.0074	0	0.0019	0	0.0080
					0.0004	0.0004	0.0004		0.0003		0.0002
Si	0.2867	0.4066	0.2268	0.88	0.0046	0.0050	0.0051	0.0003	0.0015	0	0.0049
	0.0001	0.0001	0.0001		0.0003	0.0003	0.0003	0.0002	0.0002		0.0002
Al2				0.12	0.0046	0.0050	0.0051	0.0003	0.0015	0	0.0049
					0.0003	0.0003	0.0003	0.0002	0.0002		0.0002
O1	0.3519	0.5186	0.4924	1	0.0069	0.0083	0.0095	-0.0031	0.0017	-0.0002	0.0084
	0.0001	0.0002	0.0003		0.0006	0.0007	0.0006	0.0005	0.0005	0.0005	0.0003
O2	0.1138	0.4132	0.1383	1	0.0061	0.0087	0.0082	0.0004	0.0024	-0.0002	0.0076
	0.0002	0.0002	0.0003		0.0006	0.0007	0.0007	0.0005	0.0005	0.0005	0.0003
O3	0.3619	0.2470	0.3189	1	0.0104	0.0078	0.0085	0.0002	0.0022	0.0008	0.0090
	0.0001	0.0002	0.0003		0.0006	0.0007	0.0006	0.0005	0.0005	0.0005	0.0003

Note: The atomic displacement and thermal parameters for Al1, Fe and Ti are equivalent to those of Mg whereas the atomic displacement and thermal parameters for Al2 are equivalent to those of Si

Table 3.5. Bond Valence Table (v.u.) for Fassa Valley fassaite

	Ca	Mg	Si	Σ
O1	$0.206^{x2\downarrow}$		0.897	2.099
O1	$0.141^{x2\downarrow}$		0.855	
O2	$0.330^{x2\downarrow}$	$0.399^{x2\downarrow}$	0.994	2.072
O2		$0.348^{x2\downarrow}$		
O3	$0.345^{x2\downarrow}$	$0.385^{x2\downarrow}$	1.021	1.751
Σ	2.044	2.300	3.768	

Note: Bond valences for Mg determined using a mixed site occupancy of Mg = 0.345, Al = 0.075, Fe = 0.06 and Ti = 0.02. The bond valences for Si were also determined using a mixed occupancy of Si = 0.88 and Al = 0.12

Table 3.6. Atoms per Formula Unit (APFU) Vs. Electrons per Formula Unit

cation	apfu	atomic #	epfu	epfu/site
Ca	1.024	20	20.473	
Na	0.003	11	0.033	
K		19	0.004	20.510
Mg	0.695	12	8.336	
Al	0.154	13	2.006	
Ti	0.022	22	0.477	
Cr	0.000	24	0.000	
Fe	0.122	26	3.181	
Mn	0.001	25	0.025	14.025
Si	1.758	12	21.092	
Al	0.242	13	3.150	24.242

The CaO_8 polyhedron and MgO_6 octahedron in Fassa Valley fassaite have normal Ca-O and Mg-O bond lengths ranging from 2.361(2) to 2.692(2) and 2.028(2) to 2.115(2) Å respectively (Table 3. 7). The SiO_4 tetrahedron on the other hand shows a wide range of Si-O bond lengths ranging from 1.610 to 1.695 Å, indicating significant replacement of Si by Al in the tetrahedral site (Benna et al. 1988, Oberti et al. 1982, Hazen & Finger 1977) (Table 3.7). Smith and Bailey (1963), after studying Si-O bond lengths of various mineral structures, found that there is a positive linear correlation between average overall Si-O bond lengths and the percentage of Al substituting for Si in the tetrahedral site. If the average overall Si-O bond length (1.651 Å) of Fassa Valley fassaite is used in conjunction with the predicted Si-O bond variation as a function of Al content (Fig. 3.2), the amount of Al expected to be in the tetrahedral site of Fassa Valley fassaite is ~ 17 %, in good agreement with 15 mol% tetrahedral Al as determined from EPMA (see chemical formula). The SiO_4 tetrahedra, in fassaite, share corners with two neighbouring tetrahedra to form chains of tetrahedra. The tetrahedral chains are linked together by CaO_8 polyhedra and MgO_6 octahedra.
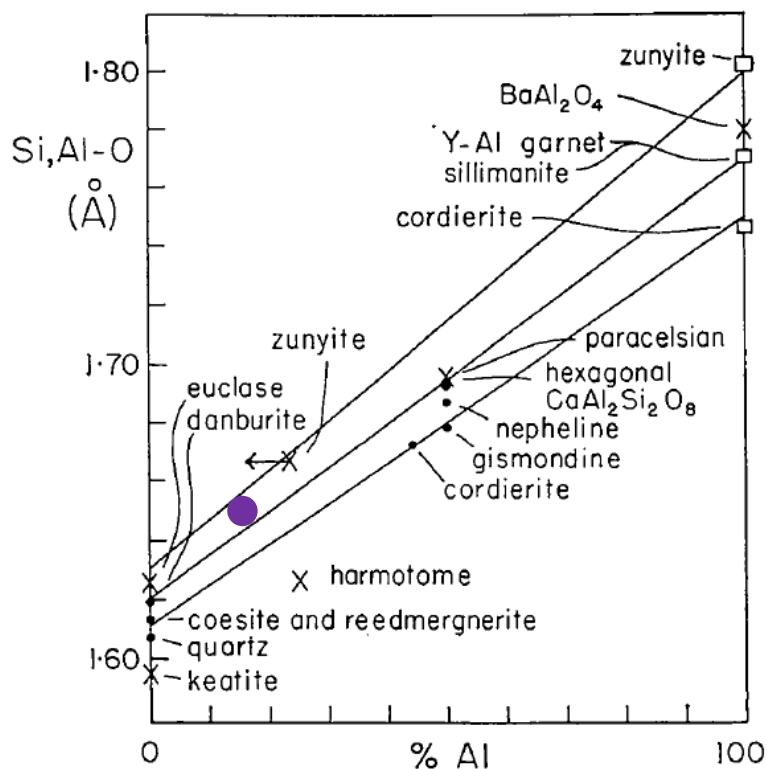
Figure 3.2. Average Si-O bond length of Fassa Valley fassaite (purple) plotted on an average Si-O bond length vs. % tetrahedral Al chart. The diagonal lines in order of increasing Si-O bondlength represent theoretical trends for framework, ring, and nesosilicates. Chart is adapted from Smith and Bailey (1963).

Table 3.7. Interatomic distances (Å) in Fassa Valley fassaite

CaO$_8$ polyhedron			SiO$_4$ Tetrahedron		
Ca	-O3x2	2.361(2)	*Si*	-O3	1.610(2)
	-O2x2	2.377(1)		-O2	1.623(2)
	-O1x2	2.552(2)		-O1	1.677(2)
	-O1x2	2.692(2)		-O1	1.695(2)
<Ca	-O>	2.496	*<Si*	-O>	1.651

MgO$_6$ Octahedron		
Mg	-O3x2	2.028(2)
	-O2x2	2.048(2)
	-O2x2	2.115(2)
<Mg	-O>	2.064
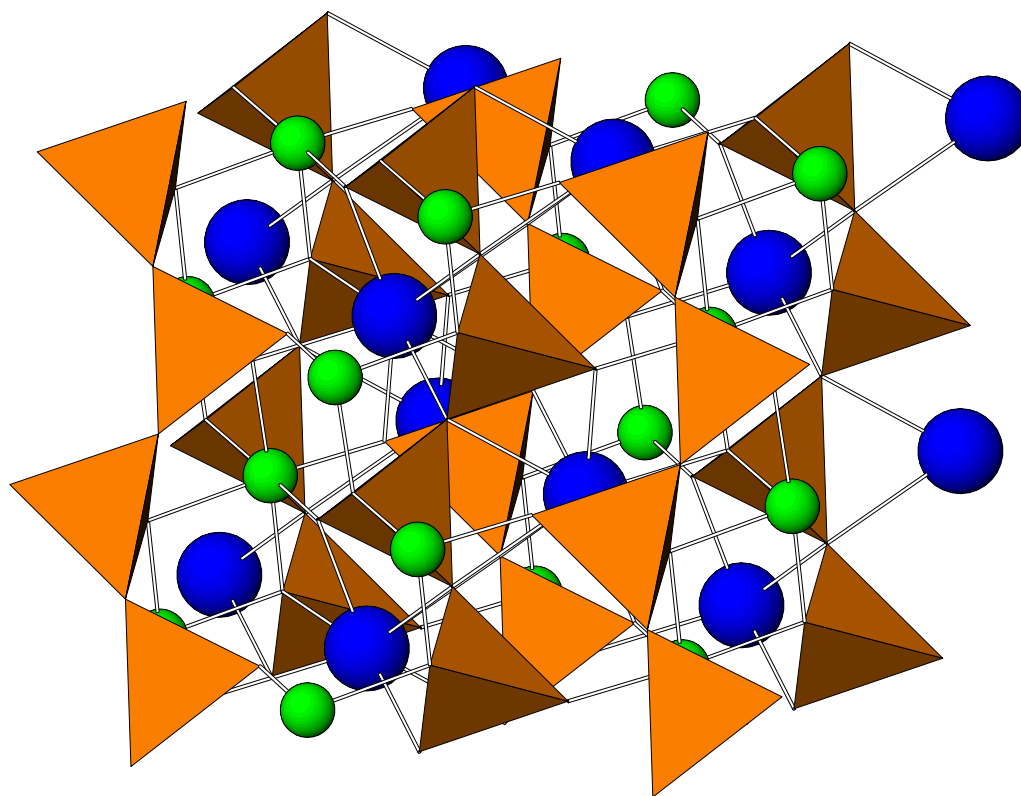
Figure 3.3. Crystal structure of Fassa Valley fassaite viewed along (110). The orange tetrahedra are Si, the green spheres are Mg, and the blue spheres are Ca.

3.3.3 ^{29}Si MAS NMR

The ^{29}Si MAS NMR spectrum of Fassa Valley fassaite is shown in Figure. 3.4, together with the spectrum of synthetic $Di_{75}CaTs_{25}$. The Fassa Valley fassaite spectrum has one broad poorly resolved peak from which no distinct Si bonding sites can be resolved. This may be due to local Al/Si disordering on the tetrahedral chain as a result of high temperature as cation disordering is highly temperature dependent (Etzel et al. 2007). Another explanation for the broad unresolved peak in the Fassa Valley fassaite (M5964) spectrum is the iron content. Evidence for this is seen from the spectrum of synthetic $Di_{75}CaTs_{25}$ (RM009D Flemming and Luth 2002) which has a similar composition to Fassa Valley fassaite, but lacks iron.
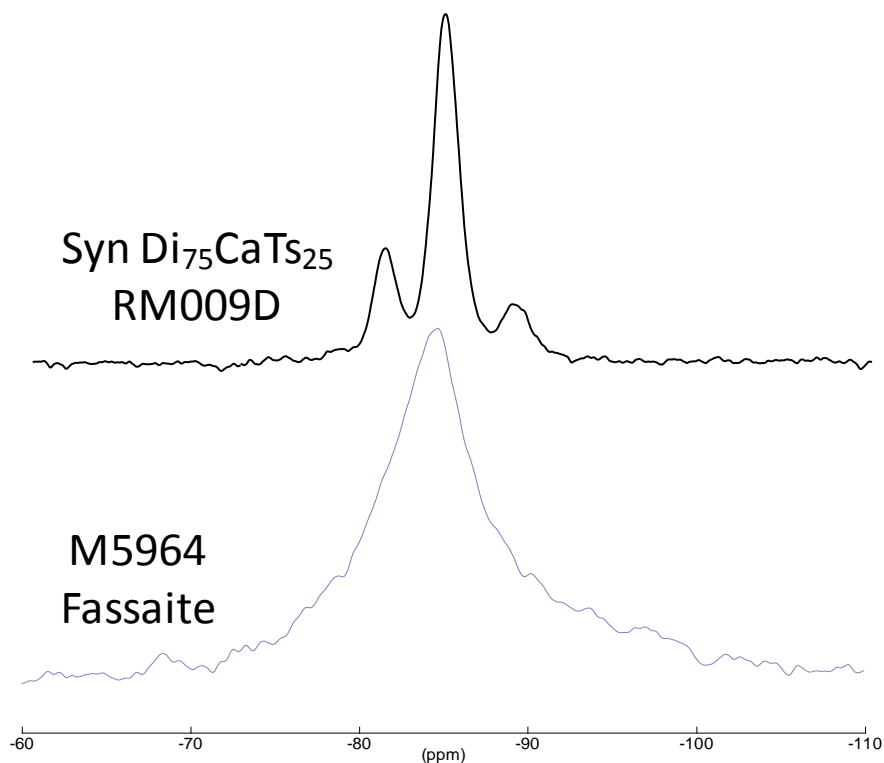
Figure 3.4. ^{29}Si NMR spectrum of Fassa Valley fassaite (M5964) as compared to synthetic Di_{75}-$CaTs_{25}$ (reproduced from Flemming and Luth 2002). The Fassa Valley fassaite spectrum was acquired at 21.1 Tesla. The spectrum for the synthetic sample was collected at 7.05 Tesla (on a Bruker AM-R 300).

3.3.4 ^{27}Al MAS NMR

The ^{27}Al MAS NMR spectrum for Fassa Valley fassaite is shown below in Figure 3.5 along with the ^{27}Al spectra for synthetic CaTs. These spectra are broadly similar and have two sets of peaks at ~80 to ~45 ppm and ~20 to ~-15 ppm, which correspond to tetrahedral sites and octahedral sites respectively. The tetrahedral sites for Fassa Valley fassaite and synthetic CaTs are each represented by a broad peak in which specific tetrahedral aluminum sites are poorly resolved. This may be due to disordering of the tetrahedral sites in synthetic CaTs and Fassa Valley fassaite. The tetrahedral peak in the ^{27}Al MAS NMR spectrum of Fassa Valley fassaite contains no contributions from vesuvianite within the sample as vesuvianite lacks tetrahedral

sites. Vesuvianite could however, contribute to the octahedral peaks in Fassa Valley fassaite

because vesuvianite like fassaite has an octahedral peak at ~ 0 ppm (Phillips et al. 1987). In

synthetic CaTs and Fassa Valley fassaite (M5964) spectra, two octahedral sites are resolved

occuring at ~5 and ~ 0 ppm. This is due to the octahedral aluminum sites resolved in the Fassa

Valley fassaite and synthetic CaTs spectrum having a similar local atomic environment.
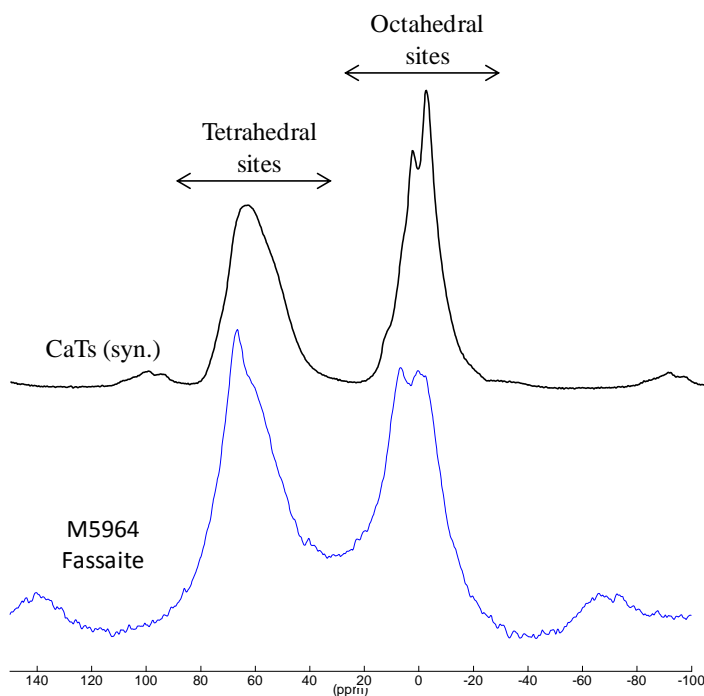
Figure 3.5. Comparison of the ^{27}Al MAS NMR spectra for synthetic CaTs and
terrestrial fassaite (M5964). All spectra were collected at 21.1 T.

3.3.5 ^{27}Al 3QMAS NMR

The ^{27}Al MQMAS NMR spectrum of Fassa Valley fassaite acquired at 21.1 T is shown below in Figure 3.6. Note the MAS NMR dimension (F2) is shown at the top of the figure and the isotropic chemical shift dimension (F1) is shown on the y-axis; both dimensions are in ppm. There are three distinct peaks resolved in the ^{27}Al MQMAS NMR spectrum of Fassa Valley fassaite. The peak located in the bottom left corner of the spectrum represents tetrahedral sites while the peak in the top right corner of the spectrum represents octahedral sites. An additional peak occurring between the tetrahedral and octahedral peaks is attributed to small amounts of vesuvianite in the sample. The presence of vesuvianite is confirmed by micro-XRD and a chemical shift of ~38 ppm is consistent with the chemical shift of five-coordinated Al in the vesuvianite crystal structure (Phillips et al. 1987).
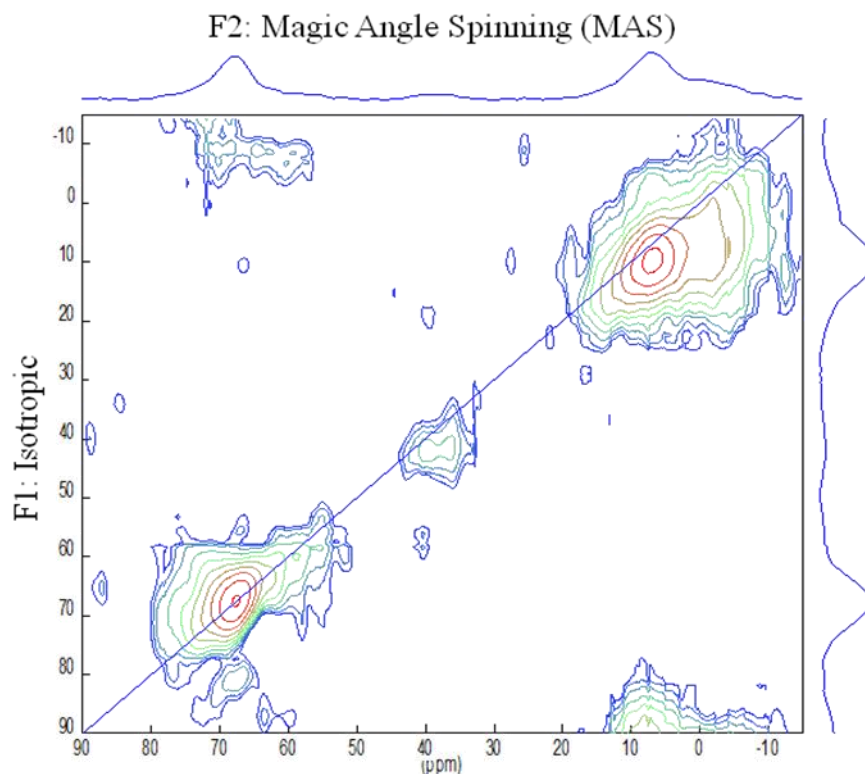
Figure 3.6. [27]AL MQMAS NMR spectrum of Fassa Valley fassaite acquired at 21.1 T. The 1:1 (F1 = F2) correspondence line is shown.

3.4 Discussion

In the ^{29}Si and ^{27}Al MAS NMR spectra of Fassa Valley fassaite, the peaks are broadened and poorly resolved such that assigning specific tetrahedral and octahedral sites is difficult. The broadening observed in the spectra of Fassa Valley fassaite may be attributed in part to its Fe content (avg. Fe_{tot} = 3.97 wt. %), because as little as 1-2 wt.% Fe is enough to cause broadening in NMR spectra (Kirkpatrick 1988).   Another contribution to peak broadening is the disordering of cations within the crystal structure (Kirkpatrick 1988, Flemming & Luth, 2002, Flemming et al. in prep).   Ordering/ disordering refer to the distribution of cations in the crystal structure. In the case of fassaite, Al-O-Al-O-Al and Si-O-Si-O-Si linkages in the tetrahedral chain are considered to be disordered cation arrangements whereas Si-O-Al-O-Si linkages are considered to be ordered   (Flemming & Luth 2002, Flemming et al. (in prep)). Studies of Al/Si cation

ordering in synthetic CaTs have been completed by Flemming & Luth (2002), Flemming et al. (in prep), and Flemming & Pawsey (2007). Because the composition of Fassa Valley fassaite contains ~ 25% CaTs component, cation ordering in CaTs will be a useful approximation of cation ordering in Fassa Valley fassaite.

3.4.1 Tetrahedral sites

Although no distinct tetrahedral environments for Al and Si could be resolved in the ^{29}Si MAS NMR and ^{27}Al MAS NMR spectra of Fassa Valley fassaite, the ^{27}Al 3QMAS NMR for Fassa Valley fassaite suggests the presence of Al/Si disordering along the tetrahedral chain. The tetrahedral peak in the ^{27}Al 3QMAS NMR spectrum of Fassa Valley fassaite follows the 1:1 correspondence line (Fig. 3.6), similar to that observed for one of the tetrahedral peaks in synthetic CaTs (Flemming and Pawsey 2007). Broadening along the 1:1 correspondence line is likely due to a distribution of chemical shifts consistent with disordering of Si and Al cations on the tetrahedral site (Flemming et al. in prep.). Because most of the peak intensity of the tetrahedral peak lies on the 1:1 correspondence line (Fig. 3.6), there is very little second order quadrupolar effect acting on the tetrahedral site, indicating that it is fairly undistorted from regular symmetry (Flemming et al. in prep., Kentgens 1997). The cation arrangement on the tetrahedral site in pyroxene has a significant effect on the octahedral site, as shown by Flemming (Flemming and Wu, 2002, Flemming & Pawsey 2007, Flemming et al. in prep).

3.4.2 Octahedral Sites

As described above, the crystal structure of fassaite consists of chains of SiO_4 tetrahedra linked together by the M2 site as well as the octahedral M1 site. The octahedral site in fassaite is linked to six neighbouring SiO_4 tetrahedra through shared corner oxygens and as such any

ordering/disordering of cations in the tetrahedral chain affects the NMR spectra of the octahedral site (Flemming et al. (2012)). Assuming that the tetrahedral chain is completely ordered (i.e. Al – O – Si – O – Al) Flemming & Pawsey (2007) & Flemming et al. (in prep.) came up with three possible Al/Si arrangements in the six tetrahedral sites surrounding M1: 2Al+4Si, 3Al+3Si, and 4Al+2Si. These arrangements have a unique chemical shift and can occur simultaneously resulting in multiple octahedral peaks.

In the ^{27}Al MAS NMR spectrum of Fassa Valley fassaite, it is possible to resolve two octahedral peaks at roughly the same chemical shift as the octahedral peaks for synthetic CaTs. Similar to synthetic CaTs these two octahedral peaks at ~ 0 and 8 ppm represent 2Al+4Si and 3Al+3Si respectively (Flemming et al. in prep.). Alternatively the peak at ~0 ppm may be representative of vesuvianite which also has an octahedral peak at ~0 ppm (Phillips et al. 1987).

3.4.3 Cation Ordering in Fassa Valley Fassaite

As observed by peak broadening in Fig. 3.4 and 3.5., Fassa valley fassaite shows peak broadening which can be attributed to cation disorder. Cation ordering is highly temperature dependent (Etzel et al. 2007) and disorder reflects a high temperature thermal history of the Fassa Valley fassaite sample. The temperature at which the structure of fassaite transitions from an disordered to a fully ordered structure has been determined , by Monte Carlo simulations, to be just under 1000 K (Warren et al. 2001, Bosenick et al. 2001). Fassa Valley fassaite has long-range disorder as is reflected in its $C2/c$ symmetry (Okamura et al. 1974). A long-range ordered fassaite sample has yet to be discovered as the transition temperature from a disordered to ordered arrangement is predicted to be so low as to be kinetically inhibited (Cohen & Burnham 1985).

References

Benna, P., Tribaudino, M., and Bruno, E. (1988) *Crystal structure of Di50CaTs50 synthetic clinopyroxene (CaMg0.5AlSi1.5O6). Crystal chemistry along the Di-CaTs join.* Mineralogy and Petrology, **Vol.** 38, 189-200.

Bosenick, A., Dove, M.T., Myers, E.R., Palin, E.J., Sainz-Diaz, C.I., Guiton, B.S., Warren, M.C., Craig, M.S., and Redfern, S.A.T. (2001) *Computational methods for the study of energies of cation distributions: applications to cation-ordering phase transitions and solid solutions.* Min. Mag., **Vol.** 65, 193-219.

Cohen, R.E. and Burnham, C.W. (1985) Energetics of ordering in aluminous pyroxenes. Am. Min., **Vol.** 70, 559-567.

Cromer, D.T. and Liberman, D. (1970): *Relativistic calculation of anomalous scattering factors for X rays.* J. Phys. Chem. **Vol.** 53, 1891-1898.

Deer, W.A., Howie, R.A. and Zussman, J. (1978) *Rock-Forming Minerals: Single Chain Silicates 2nd edition*, **Vol**. 2A, Longman Group Ltd. pp 399-414.

Dowty, E. and Clark, J.R. (1973) *Crystal Structure Refinement and Optical Properties of a Ti^{3+} Fassaite from the Allende Meteorite*. Am. Min. **Vol.** 58, 230-242

Etzel, K. And Bensiek, A. (2008) *Thermodynamic mixing behavior of synthetic Ca-Tschermak-diopside pyroxene solid solutions: III. An analysis of IR line broadening and heat of mixing behavior.* Phys. Chem. Mineral. **Vol.** 35, 399-407.

Etzel, K., Bensiek, A., Dachs, E. And Cemic, L. (2007) *Thermodynamic mixing behavior of synthetic Ca-Tschmak-Diopside pyroxene solid solutions: I. Volume and Heat Capacity.* Phys. Chem. Mineral. **Vol.** 34, 733-746.

Flemming, R.L., Teskikh, V. and Ye, E.(2012). *Aluminum environments in Ca-Tschermak's clinopyroxene (CaTs) from ^{27}Al MAS NMR and ^{27}Al 3QMAS NMR*. In Preparation.

Flemming, R.L. and Pawsey, S. (2007) *^{27}Al 3QMAS NMR Spectroscopy of Aluminous Clinopyroxene ay 11.7 and 21.1 Tesla.* National Research Council Canada Annual Report 2006-2007.

Flemming, R.L. and Luth, R.W. (2002) *^{29}Si MAS NMR study of diopside – Ca-Tschermak clinopyroxenes: Detecting both tetrahedral and octahedral Al*. Am. Min, **Vol.** 87, 25-36.

Frydman, L. and Harwood, J.S., (1995)*Isotropic Spectra of Half-Integer Quadrupolar Spins from Bidimensional Magic-Angle Spinning NMR*. J. Am. Chem. Soc., **Vol.** 117, 5367-5368.

Hazen, R.M. and Finger, L.W. (1977) *Crystal Structure and Compositional Variation of Angra Dos Reis Fassaite.* Earth and Planetary Science Letters, **Vol.** 35, 357-362.

Jarosewich (2002), Journal of Research of the National Institute of Standards and Technology, **Vol.** 107 Number 6, November-December 2002, pp. 681-685.

Kirkpatrick, J. (1988) *MAS NMR Spectroscopy of Minerals and Glasses*. Rev. Min. **Vol.** 18, 341.

Kentgens, A.P.M. (1997) *A Pratical Guide to Solid-State NMR of half Integer Quadrupolar Nuclei with Some Applications to Disordered Systems*. Geoderma, **Vol.** 80, 271-306.

Oberti, R., Munno, R., Foresti, E. and Krajewsky, A. (1982) *A Crystal-Chemical Strudy on Six Fassaites From the Predazzo-Monzoni Area.* Soc. Ital. Min. Petr. **Vol.** 38, 649-655.

Okamura, F.P., Ghose, S. and Ohashi, H. (1974) Structure and crystal chemistry of calcium Tschermak's pyroxene, $CaAlAlSiO6$. Am. Min., **Vol** 59, 549-557.

Peacor, D.R. (1967) *Refinement of the Crystal Structure of a Pyroxene of Formula $M_I M_{II}(Si_{1.5}Al_{0.5})O_6$.* Am. Min. **Vol.** 52, 31-41.

Phillips, B.L., Allen, F.M., and Kirkpatrick, J.R., (1987) *High-resolution Solid-state ^{27}Al NMR spectroscopy of Mg-rich Vesuvianite.* Am. Min. **Vol.** 72, 1190-1197.

Sheldrick, G.M. (1997): SHELXL-97: *A computer program for the Refinement of Crystal Structures.* Univ. of Göttingen, Göttingen, Germany.

Smith, J.V. and Bailey S.W. (1963) *Second Review of Al-O and Si-O Tetrahedral Distances*. Acta. Cryst. **Vol.** 16, 801-811.

Warren, M.C., Dove, D.T., Myers, E.R., Bosenick, A., Palin, E.J., Sainz-Diaz, C.I., Guiton, B.S. and Redfern, S.A.T. (2001). *Monte Carlo methods for the study of cation ordering in minerals.* Min. Mag. **Vol**. 65, 221-248.

Chapter 4: Al/Si Cation Ordering in Allende Fassaite: A combined single Crystal XRD and ^{27}Al and ^{29}Si NMR Spectroscopy Study

Abstract

Al- rich Ti-bearing diopside, referred to here as "fassaite" occurs in both terrestrial and extraterrestrial environments. Unlike terrestrial fassaite, extraterrestrial fassaite contains more titanium and less iron than terrestrial fassaite making them ideal for NMR spectroscopy studies. Here we present crystal structure data by single crystal XRD and Al/Si cation ordering data by ^{29}Si and ^{27}Al MAS NMR and ^{27}Al MQMAS NMR spectroscopy. The unit cells for Allende TS62B fassaite and Allende USNM 3529 fassaite were found to be a 9.770(2), b 8.840(2), c 5.340(1) Å, β 105.90(3) °, and V = 443.55(2) Å^3 and a 9.715(3) b 8.823(3) c 5.301(2) Å, β 106.04(1) °, and V = 436.70(3) Å^3 respectively consistent with past structure refinements of fassaite. Both fassaite samples have $C2/c$ symmetry consistent with long range Al/Si disorder within the crystal structure. The empirical formulas derived by EPMA analysis of the two fassaite samples were determined to be $Ca_{1.01}(Mg_{0.55}Al_{0.2}Ti_{0.17})_{\Sigma=0.92}(Si_{1.43}Al_{0.57})_{\Sigma=2}O_6$ and $Ca_{1.01}(Mg_{0.50}Al_{0.27}Ti_{0.17})_{\Sigma=0.94}(Si_{1.44}Al_{0.56})_{\Sigma=2}O_6$. ^{29}Si MAS NMR spectra from the two fassaite samples contained three well resolved peaks narrow (FWHM 3 ppm) occurring at ~ -81, -84, and -89 ppm representing Si(2Al)[1Al], Si(1Al)[1Al], and Si(0Al)[1Al] sites respectively where ( ) is tetrahedral next nearest neighbours (NNN) and [ ] is an octahedral NNN. ^{27}Al MAS NMR spectra of the two Allende fassaite samples contained two sets of peaks at 80 to 50 ppm and 20 and -15 ppm representing tetrahedral and octahedral peaks respectively. The octahedral peaks in the ^{27}Al MAS NMR spectra contained two well resolved, narrow peaks occurring at 13 and -4 ppm representing 4Al+2Si and 1Al+5Si tetrahedral environments surrounding the octahedral Al sites. ^{27}Al 3QMAS NMR spectroscopy of the two fassaites resolved at least five tetrahedral sites

- four of which represent tetrahedral Al sites in fassaite and one represents small amounts of melilite in the samples. The well resolved narrow peaks in the NMR spectra of the fassaite samples indicate the presence of ordered domains within the long range disordered crystal structure of fassaite. These ordered domains are interpreted as short range cation ordering occurring above disordered to ordered transition temperature for fassaite. The cation ordering data for the Allende fassaite samples likely reflect conditions on the Allende parent body.

4.1 Introduction

Al-rich, Ti-bearing diopside occurs in both terrestrial and extraterrestrial environments. Extraterrestrial dark green, highly pleochroic Al-rich, Ti-bearing diopside was first discovered in calcium aluminum inclusions (CAIs) from the Allende and Vigarano CV carbonaceous chondrites (Marvin et al. 1970, Clark et al. 1973, Fuchs 1971, and Michel-Levy et al. 1970). This Al-, Ti-rich diopside was referred to as fassaite after a crystal structure refinement of Allende Al-, Ti-rich diopside by Dowty and Clark (1973) showed that it was structurally similar to terrestrial fassaite (Brearley & Jones 1998). The name fassaite was discredited in 1988 by the Interational Mineralogical Association (IMA), in favour of Al-rich, Ti-bearing diopside, however, the name "fassaite" will be used throughout this paper for brevity.

Fassaite is a common primary phase in CAIs (Brearley & Jones 1998) and is suggested to have condensed at ~1435 K, based on the calculated equilibrium condensation sequence by Lattimer et al. 1978 and Grossman 1972. Although fassaite is a primary phase in CAIs, its abundance and composition varies between CAI types. Fassaite is a rare phase in Type A CAIs making up less than 5 vol. % of the CAI. (Grossman 1975). If present, fassaite in Type A CAIs is restricted to thin (~ 5 μm) rims around the CAI. The composition of fassaite in Type A

CAIs tends to be < 9% Al_2O_3 and <0.7 % Ti (Grossman 1975). Unlike Type A CAIs, fassaite is a major phase in Type B CAIs making up 35 to 60 vol. % of the CAI. Fassaite in Type B CAIs occurs as coarse crystals, usually 1 mm in diameter or larger. Compositionally, fassaite from Type B CAIs contains more Al_2O_3 (> 15 wt. %) and Ti (>1.8 wt. %) than fassaite from Type A CAIs (Grossman 1975). Finally, fassaite in Type C CAIs makes up ~ 10 to 30 vol. % of the CAI and has a variable composition with 1-25 wt % Al_2O_3 and 1-13 wt % TiO_2 (Brearley & Jones 1998, Wark 1987).

Besides CAIs in carbonaceous chondrites, Fassaite occurs in angrite achondrites. Fassaite is a dominant phase in angrites where it occurs as a fine grained (100 μm) ground mass or as large grains often 1 mm in diameter (Mittlefehldt et al. 2002, Brearley & Jones 1998). The coarse-grained fassaite commonly joins in triple junctions and may also poikialitically enclose fine-grained fassaite as well as other phases such as spinel and whitlockite (Brearley & Jones 1998). The composition of fassaite from angrites is comparable to that of fassaite from CAIs with 3.91 to 11.8 wt % Al_2O_3 and 0.83 to 4.75 wt % TiO_2. Unlike fassaite from CAIs, fassaite from angrites contains significant FeO_{tot} (6.70 to 27.4 wt %) (Mittlefehldt et al. 2002, Brearley & Jones 1998).

Fassaite crystals from both Type B CAIs and angrites show compositional zonation (Mittlefehldt et al. 2002, Brearley & Jones 1998). The wide variation seen in Al and Ti compositions in Type B CAI fassaite (5 to 10 wt % TiO_2 and 15 to 21 wt % Al_2O_3; Grossman 1975, Brearley & Jones 1998) can be attributed to the presence of compositional concentric and sector zoning within the fassaite crystals (Simon et al. 1991, Grossman 1975). Zoned fassaite crystals commonly have cores rich in Al and Ti relative to the rims, where the variation in Al is less than that for Ti (Simon et al. 1991). Fassaite from angrites, especially A-881371, LEW

87051, and D'Orbigny, show compositional variation in Mg and Fe as well as Al and Ti, which

can also be attributed to compositional concentric and sector zoning (Mittlefehldt et al. 2002,

Brearley & Jones 1998).

Crystal structure refinements of both terrestrial and extraterrestrial fassaite have

consistently shown that they both have $C2/c$ symmetry as well as unit cell parameters where $a \sim$

9.7, $b \sim 8.8$, $c \sim 5.3$ Å and $\beta \sim 105$ ° (Peacor 1967, Dowty & Clark 1973, Mittlefehldt et al. 2002,

Hazen & Finger 1977). Whereas terrestrial and extraterrestrial fassaites are structurally similar,

there are important differences in their compositions. Terrestrial fassaite contains significant Fe

(> 1 wt.%) in both the Fe^{3+} and Fe^{2+} valence states and has little or no TiO_2 (Deer et al. 1987,

Oberti et al. 2007, Peacor 1967). Fassaite from angrites contains significant Fe, however, it

occurs only in the Fe^{2+} valence state (Hazen & Finger 1977). Fassaite from both CAIs and

angrites contains significant Ti and, in the case of CAI fassaite, Ti occurs as Ti^{4+} and Ti^{3+}

(Dowty & Clark 1973, Hazen & Finger 1977, Mittlefehldt et al. 2002, Simon et al. 1991,

Grosman 1975, Brearley & Jones 1998). The fassaite from the CAIs differs from both terrestrial

fassaite and angrite fassaite by its lack of iron. Fassaite from CAIs contains <0.6 wt % FeO

(Brearley & Jones 1998) and thus lends itself to cation ordering studies using Nuclear Magnetic

Resonance (NMR) spectroscopy.

Fassaite can be considered as having an intermediate composition along the diopside (Di)

– Ca-Tschermak (CaTs) solid solution ($CaMgSi_2O_6$ – $CaAl(AlSi)O_6$) where significant

replacement of Si^{4+} in tetrahedral site and Mg^{2+} in the octahedral site by Al^{3+} results in Si/Al and

Mg/Al order/disorder. At high temperatures, pyroxene with a high CaTs component, has a $C2/c$

symmetry which implies complete disorder along the tetrahedral chain (Okamura et al. 1974).

Upon cooling the crystal structure of the CaTs pyroxene undergoes a phase transition from $C2/c$

symmetry to lower symmetry representing a more ordered structure. A fully ordered fassaite structure obeys the Al – avoidance principle and consists of alternating Si and Al tetrahedral whereas a disordered structure will have Al-O-Al or Si-O-Si linkages (Flemming & Luth 2002). The Al – avoidance principle first proposed by Lowenstein in 1954 assumes a non-random distribution of Al and Si tetrahedral where Al-O-Al linkages are avoided due to electrostatic considerations (Cohen & Burnham 1985). In the crystal structure of fassaite, the replacement of Si by Al is between 0.25 and 0.50 per mole, making fassaite useful for Al/Si cation ordering studies (Deer et al. 1987).

Aluminum/silicon cation ordering on the tetrahedral chain may only be inferred indirectly from bond length variations when using X-ray methods. This is due to Si and Al having similar scattering behaviour such that they are indistinguishable by X-rays. Instead of X-ray techniques, nuclear magnetic resonance (NMR) spectroscopy allows one to observe short-range ordering directly. Recent NMR techniques such as magic angle spinning nuclear magnetic resonance (MAS NMR) spectroscopy provide high resolution spectra of solids allowing for more accurate interpretations of cation ordering (especially Si ordering) in solids. A study by Flemming and Luth (2002) directly observed Si-Al ordering in synthetic aluminous pyroxene using ^{29}Si MAS NMR. Flemming and Luth (2002) also found that the ^{29}Si MAS NMR spectrum of the pyroxene was affected by Al substitution in the octahedral site. Therefore ^{29}Si MAS NMR may be used to indirectly observe the octahedral environment in pyroxene, whereas ^{27}Al MAS NMR allows for direct observation of both tetrahedral and octahedral sites. In addition to ^{27}Al MAS NMR, [27]Al MQ (Multiple Quantum) MAS NMR may be used, because Al is a quadrupolar nucleus with I=5/2, to get additional information about site distortion. In this study we report crystal structure data for two fassaite samples from the Allende CV3 chondrite, by single crystal X-ray diffraction

(XRD). In addition, we report cation ordering data for these fassaite samples, by ^{29}Si and ^{27}Al

MAS NMR and ^{27}Al MAS and MQMAS NMR. Such a study has never been performed on an

extraterrestrial fassaite sample and could provide constraints on the cooling history of the

Allende meteorite.

4.2 Methods

Identification of fassaite in the USNM 3529 CAI was completed using a Bruker Discover

micro X-ray diffractometer with Co Kα radiation and a nominal beam diameter of 300 μm. The

data was collected using a 2dimensional Hi-star detector and General Area Detector diffraction

system (GADDS) software, using two frames with 2θ at 37.5 and 70°, using a rotating optics

method (omega scan) with rotation through 15 and 25° for the two frames, respectively. A total

of 8 points from USNM 3529 were X-rayed and the X-ray patterns were integrated using

GADDS and mineralogical identification was performed using the International Centre for

Diffraction Data (ICDD), accessed via Bruker's EVA® interface. Micro – XRD analysis was not

completed on CAI TS62B, as the fassaite was already identified and extracted by Drs. Simon and

Grossman from the University of Chicago, who loaned us the sample for this study.

Initial qualitative chemical analysis was performed on a Hitachi SU6600 Field Emisson

Gun Scanning Electron Microscope (FEG-SEM) with a voltage of 15.0 KV. Final quantitative

chemical analysis was collected by Electron Probe Microanalysis (EPMA), by Renaud

Geological Consulting, using a JEOL JXA-733 Superprobe with an accelerating voltage of 15

KV and a beam current of 11 nA. A set of microbeam standards from SPI (Structure Probe Inc.)

and natural minerals from the Smithsonian Institution were used for calibration (Jarosewich,

1980 and 2002). The standards used were Hot Springs Arizona quartz (Si), Ilmen Mountains

ilmenite (Ti), synthetic corundum (Al), Tiebaghi Mine chromite (Cr), Ivigtut Greenland siderite

(Fe), manganotantalite (Mn), Oberdorf Austria dolomite (Mg), microcline (K), calcite (Ca), and

albite (Na). The elements Na, K, Mn, Fe, and Cr were sought but not detected in significant

amounts (i.e. < 1 wt %). X-ray intensity data was then collected for the samples using a Bruker

Kappa Apex II single crystal diffractometer with MoKα radiation and a sample to detector

distance of 4.0 cm. Crystals ~ 100 μm in diameter and showing no twinning were selected from

the terrestrial fasaite and Allende fassaite for intensity data collection. All reflections from the

X-ray intensity data were then merged using XPREP and a solution and structure refinement was

determined using SHELX-97. The solution was determined using direct methods, with

scattering curves and anomalous scattering factors from Cromer & Mann (1968) and Cromer &

Liberman (1970).

Table 4.1. Miscellaneous Data for Allende fassaite TS62B.			
a (Å)	9.770 (2)	Monochromator	Graphite
b(Å)	8.840(2)	Intensity-data collection criterion for observed reflections	θ:2θ Fo> 4σ(Fo)
c(Å)	5.340(1)	GoOF	1.149
β(°)	105.90(3)	Total No. of Reflections	4367
Space Group	$C2/c$	No. of unique reflections	505
Z	2	R (%)	2.62
Diffractometer	Bruker Kappa Apex II	wR^2%	4.89
Radiation	MoKα (50 KV, 40mA)		

Table 4.2. Miscellaneous Data for Allende fassaite USNM 3529.			
a (Å)	9.715 (3)	Monochromator	Graphite
b(Å)	8.823(3)	Intensity-data collection criterion for observed reflections	θ:2θ Fo> 4σ(Fo)
c(Å)	5.301(2)	GoOF	1.149
$β$(°)	106.04(1)	Total No. of Reflections	10087
Space Group	$C2/c$	No. of unique reflections	1372
Z	2	R (%)	1.79
Diffractometer	Bruker Kappa Apex II	wR^2%	7.35
Radiation	MoKα (50 KV, 40mA)		

^{29}Si and ^{27}Al MAS NMR spectra were collected on both Allende fassaite samples. NMR spectra were collected on approximately 4 to 7 mg (packed in 2.5mm MAS rotors) of TS62B and USNM 3529 using a 21.1 T (^{1}H at 900 MHz) Bruker Avance II NMR Spectrometer at the Canadian National Ultrahigh - Field NMR Facility for Solids. ^{29}Si spectra for the samples were collected with a 90° pulse width of 2.0 μs over a sweep width of 20 KHz. The ^{29}Si spectra for TS62B and USNM 3529 involved 7524 and 6144 scans respectively, each with relaxation delay times of 30 s between scans. Chemical shifts for the ^{29}Si NMR experiments were referenced to tetramethlysilane (TMS) (Si(CH$_3$)$_4$). ^{27}Al spectra for the samples were collected with a 90° pulse width of 0.5 μs over a sweep width of 100 KHz. The ^{27}Al spectra for both TS62B and USNM 3529 involved 2000 scans, each with a relaxation delay time of 5 s between scans. The ^{27}Al 3QMAS spectra for Allende TS62B and USNM 3529 fassaite samples involved 2160 and 960 scans respectively, each with a relaxation delay time of 2 s. ^{27}Al 3QMAS NMR data were

collected over a sweep width of 31.2 kHz.   Chemical shifts for ^{27}Al NMR spectroscopy were referenced to 0.5 mol aqueous $AlCl_3$.

4.3 Results

4.3.1 Electron Probe Micro Analysis (EPMA)

The average chemical compositions of Allende TS62B and USNM 3529 fassaite are presented below in Tables 4.3 and 4.4. From the average chemical composition, the empirical formulae $Ca_{1.01}(Mg_{0.55}Al_{0.2}Ti_{0.17})_{\Sigma=0.92}$ $(Si_{1.43}Al_{0.57})_{\Sigma=2}O_6$ and

$Ca_{1.01}(Mg_{0.50}Al_{0.27}Ti_{0.17})_{\Sigma=0.94}(Si_{1.44}Al_{0.56})_{\Sigma=2}O_6$ were derived for the Allende TS62B and USNM 3529 fassaite samples based on 35 and 26 analyses respectively (see appendix 4). Cations were apportioned to the tetrahedral and octahedral sites by assuming the tetrahedral site contained all the Si as well as some Al such that the sum of cations in the tetrahedral site was equal to two. The remaining Al was placed in the octahedral site along with Mg, Fe, and Ti. If the ^{27}Al MAS NMR of the two Allende fassaite spectra are assumed to be quantitative, roughly 51% of the Al is found in the tetrahedral site while 49% of the Al is in the octahedral site. The discrepancy between the EPMA data and the NMR spectra may be due to small amounts of melilite in the sample contributing to the intensity of the octahedral Al peak.

These chemical compositions are consistent with Tschermak's substitution reactions between diopside and CaTs end-members, where the general formula for intermediate members is $\{Ca\}[Mg_{1-x}Al_x](Si_{2-x}Al_x)O_6)$ ({} = 8 coordinated site, [] = octahedral site, () = tetrahedral site) (Flemming & Luth 2002).

Table 4.3. Representative EPMA data (wt. % oxides) for TS62B fassaite.						
	1	2	3	4	5	6
SiO_2	37.49	38.06	40.85	43.44	42.42	37.94
TiO_2	7.66	6.17	4.83	4.1	3.33	6.58
Al_2O_3	18.9	20.75	15.61	13.94	15.5	19.51
Cr_2O_3	0.08	0.11	0.03	0.02	0.05	0.04
FeO_{tot}	0.06	0.07	0.08	0.04	0.01	0.06
MgO	9.84	8.88	12.27	12.58	12.81	9.94
MnO	0.1	0.09	0.02	0.02	0	0.14
K_2O	0.01	0.04	0.03	0.05	0.07	0
CaO	26.1	25.84	26.1	25.83	25.64	25.63
Na_2O	0.01	0	0.03	0.04	0	0.01
SUM	100.25	100.01	99.85	100.06	99.83	99.85

Table 4.4. Representative EPMA data (wt. % oxides) for Allende USNM 3529 fassaite.						
	1	2	3	4	5	6
SiO2	40.49	38.99	38.55	41.37	37.71	40.33
TiO2	6.06	4.62	7.15	5.53	7.91	5.43
Al2O3	18.10	20.61	18.65	15.84	20.27	17.49
Cr2O3	0.08	0.05	0.14	0.07	0.07	0.04
FeO	0.05	0.02	0.00	0.03	0.00	0.29
MgO	10.16	10.96	9.79	11.17	8.25	10.24
MnO	0.00	0.12	0.00	0.00	0.02	0.00
K2O	0.04	0.02	0.01	0.02	0.07	0.06
CaO	25.19	25.39	25.83	25.86	25.84	25.81
Na2O	0.02	0.01	0.00	0.02	0.02	0.08
SUM	100.19	100.79	100.12	99.91	100.16	99.77

4.3.2 X-ray Diffraction (XRD)

Micro-XRD indicated that the Allende USNM 3529 fassaite sample contained significant finely crystalline to coarse grained fassaite as well as small amounts of melilite, spinel, and anorthite (Fig. 4.1).

From single crystal XRD, the Allende TS62B and USNM 3529 fassaite crystals were found to be monoclinic with the space group $C2/c$ and the following unit cell dimensions: a 9.770(2), b 8.840(2), c 5.340(1) Å, β 105.90(3)°, and V = 443.55 Å^3 and a 9.715(3), b 8.823(3), c 5.301(2) Å, β 106.04(1) °, and V = 436.70 Å^3 respectively. These results are consistent with past structure refinements of fassaite by Peacor (1967), Dowty & Clark (1973), and Hazen & Finger (1977) (Table 4.5).

Table 4.5. Unit Cell Paramters of Fassa Valley Fassaite Compared with Past Studies.						
	Fassa Valley fassaite (this study)	Allende fassaite TS62B	Allende fassaite USNM 3529 (this study)	Allende Fasasite (Dowty & Clark 1973)	Angra Dos Reis Fassaite (Hazen & Finger 1977)	Oka Quebec Fassaite (Peacor 1967)
a (Å)	9.753(2)	9.770(2)	9.715(3)	9.80(1)	9.738(1)	9.794(5)
b (Å)	8.888(2)	8.840(2)	8.823(3)	8.85(1)	8.874(2)	8.906(5)
c (Å)	5.286(1)	5.340(1)	5.301(2)	5.36(5)	5.2827(5)	5.319(3)
β (°)	105.96(3)	105.90(3)	1.06.04(1)	105.37(1)	105.89(1)	105.90(3)
V (Å^3)	443.55(2)	443.56(2)	436.70(3)	448.25(1)	439.1(1)	446.21(3)
Sym.	$C2/c$	$C2/c$	$C2/c$	$C2/c$	$C2/c$	$C2/c$
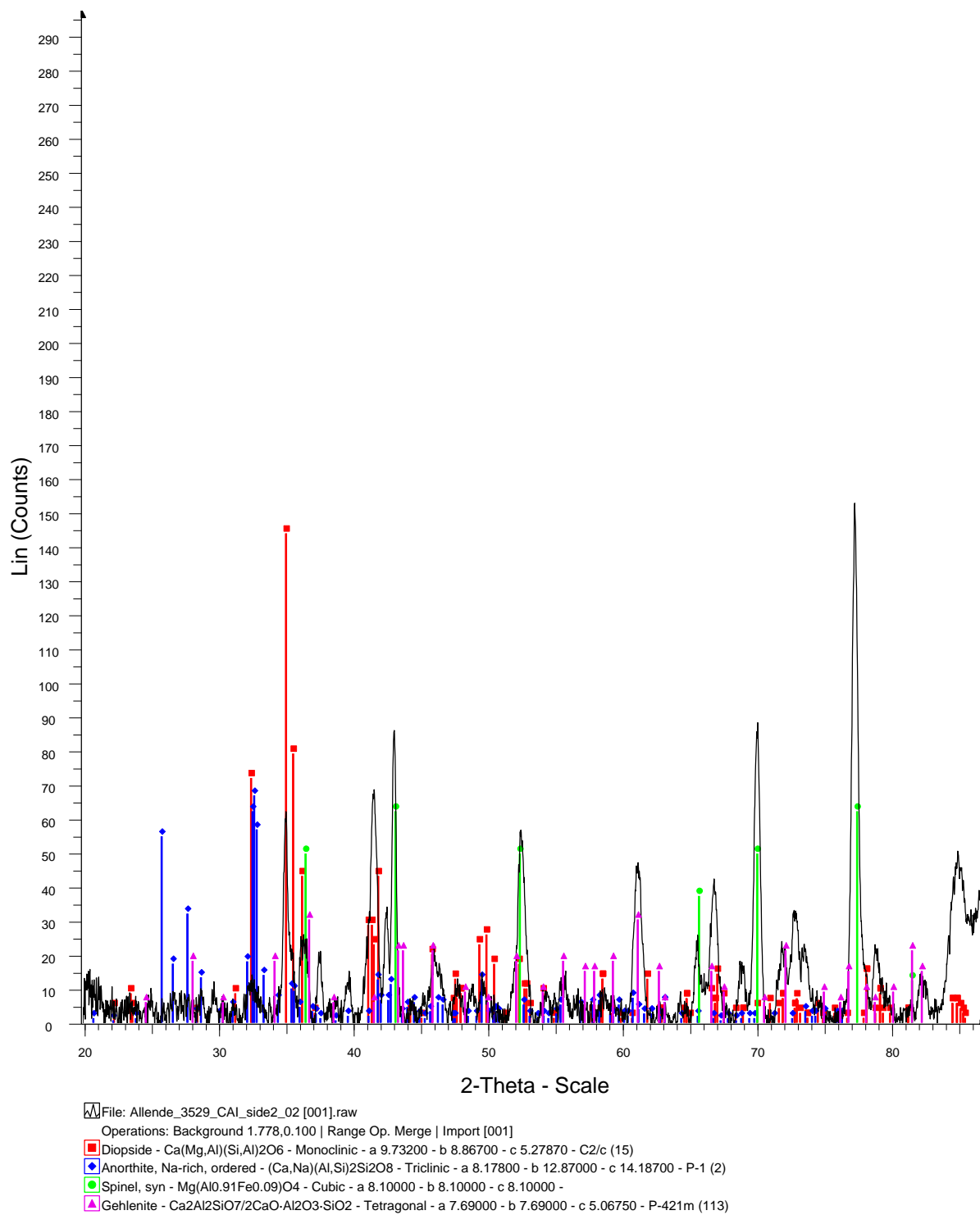
Figure 4.1. Micro-XRD pattern for Allende fassaite USNM 3529.

In the crystal structures of both Allende fassaite samples, individual sites were found for Ca, Mg, and Si whereas three sites where found for oxygen (Tables 4.6 & 4.7). During the initial refinement of the crystal structures, the site occupancy factors (SOFs) for Mg and Si were found to be less than the ideal SOFs of 0.5 and 1.0 respectively for those sites. This indicated the presence of additional cations in the Mg and Si sites. From EPMA data (see above) Al and to a lesser extent, Ti, substitute for Mg while significant amount Al substitutes for Si. Magnesium, silicon, and aluminum are very close in atomic number and as such have similar scattering powers making these elements difficult to distinguish from one another using X-ray methods. Since Mg, Si and Al are difficult to distinguish using X-ray methods, the SOFs (Tables 4.6 & 4.7) of the cations on the Mg and Si sites were fixed based on EPMA results (Tables 4.3 & 4.4). The additional octahedral octahedral cations (Al1 and Ti) were refined into the Mg site using the "SUMP" command. Using the SUMP command, the total occupancy of the octahedral site was fixed at one and the site occupancy factors of Mg, Al1, and Ti were allowed to refine such that they summed to one.

Table 4.6. Atomic and Displacement Parameters for Allende fassaite TS62B

Atom	x	y	z	SOF	U11	U22	U33	U23	U13	U12	Ueq
Ca	0	0.1946	1/4	1/2	0.0136	0.0087	0.0083	0	0.0008	0	0.0106
		0.0001			0.0006	0.0006	0.0006		0.0005		0.0003
Mg	0	0.5923	1/4	0.275	0.0068	0.0073	0.0049	0	0.0013	0	0.0064
		0.0002			0.0008	0.0009	0.0008		0.0006		0.0004
*Al*1				0.125							
Ti				0.085							
Si	0.2874	0.4062	0.2248	0.715	0.0061	0.0069	0.0068	0.0011	0.0020	-0.0002	0.0066
	0.0001	0.0001	0.0002		0.0006	0.0006	0.0006	0.0005	0.0004	0.0005	0.0003
*Al*2				0.285							
*O*1	0.3525	0.4811	-0.0089	1	0.0115	0.0144	0.0140	0.0027	0.0023	-0.0004	0.0135
	0.0003	0.0003	0.0005		0.0015	0.0017	0.0016	0.0012	0.0012	0.0013	0.0009
*O*2	0.1117	0.4141	0.1348	1	0.0144	0.0150	0.0169	0.0017	0.0059	-0.0006	0.0151
	0.0003	0.0003	0.0005		0.0017	0.0018	0.0017	0.0013	0.0013	0.0012	0.0010
*O*3	0.3629	0.2439	0.3180	1	0.0219	0.0153	0.0132	-0.0004	0.0063	-0.0005	0.0165
	0.0003	0.0003	0.0006		0.0017	0.0018	0.0017	0.0013	0.0013	0.0013	0.0009

Note: The atomic displacement and thermal parameters for Al1, Fe and Ti are equivalent to those of Mg
whereas the atomic displacement and thermal parameters for Al2 are equivalent to those of Si

Table 4.7. Atomic and Displacement Parameters for Allende fassaite USNM 3529

ATOM	X	y	z	SOF	U11	U22	U33	U23	U13	U12	Ueq
Ca	0	0.19442	1/4	1/2	0.0121	0.0091	0.0083	0	0.0003	0	0.0103
		0.00003			0.0001	0.0001	0.0001		0.0001		0.0001
Mg	0	0.59240	1/4	0.27	0.0060	0.0069	0.0058	0	0.0006	0	0.0064
		0.00004			0.0002	0.0002	0.0002		0.0001		0.0001
Al1				0.128							
Ti				0.087							
Si	0.28746	0.40620	0.22478	0.713	0.0055	0.0072	0.0062	0.0004	0.0012	-0.0002	0.0064
	0.00003	0.00003	0.00005		0.0001	0.0001	0.0001	0.0001	0.0001	0.0001	0.0001
Al2				0.287							
O1	0.3528	0.4811	-0.0097	1	0.0088	0.0118	0.0110	0.0027	0.0019	-0.0002	0.0107
	0.0001	0.0001	0.0001		0.0002	0.0003	0.0003	0.0002	0.0002	0.0002	0.0001
O2	0.1116	0.4142	0.1351	1	0.0084	0.0125	0.0121	0.0013	0.0031	-0.0007	0.0109
	0.0001	0.0001	0.0001		0.0003	0.0003	0.0003	0.0002	0.0002	0.0002	0.0001
O3	0.3627	0.2431	0.3178	1	0.0149	0.0111	0.0110	0.0006	0.0027	-0.0009	0.0125
	0.0001	0.0001	0.0001		0.0003	0.0003	0.0003	0.0002	0.0002	0.0002	0.0001

Note: The atomic displacement and thermal parameters for Al1, Fe and Ti are equivalent to those of Mg whereas the atomic displacement and thermal parameters for Al2 are equivalent to those of Si

The CaO_8 polyhedron and MgO_6 octahedron in both Allende TS62B and USNM 3529 fassaite have normal Ca-O and Mg-O bond lengths ranging from 2.375 to 2.6762 and 1.985 to 2.102 Å respectively (Tables 4.7 & 4.8). The SiO_4 tetrahedron in both Allende fassaite structures shows a wide range of Si-O bond lengths ranging from 1.627 to 1.7105 Å, indicating significant replacement of Si by Al in the tetrahedral site (Benna et al. 1988, Oberti et al. 1982, Hazen & Finger 1977) (Tables 4.8 & 4.9). Smith and Bailey (1963), after studying Si-O bond lengths of various mineral structures found that there is a positive linear correlation between average overall Si-O bond lengths and the percentage of Al substituting for Si in the tetrahedral

site. If the average overall Si-O bond length of Allende TS62B fassaite (1.669 Å) and Allende

USNM 3529 fassaite (1.662) are used in conjunction with the predicted Si-O bond variation as a

function of Al content (Fig. 4.2), the amount of Al expected to be in the tetrahedral sites of

Allende TS62B and USNM 3529 fassaite is ~ 25-27% , in good agreement with 28% tetrahedral

Al determined from the empirical formula (Smith & Bailey 1963). Comparing the average

overall Si-O bond length (1.662 Å) of Allende USNM 3529 fassaite with the predicted Si-O

bond variation as a function of Al content, the amount of Al expected to be in the tetrahedral site

of Allende USNM 3529 fassaite is ~ 25%, in good agreement with 28.5% tetrahedral Al

determined from the empirical formula (Smith & Bailey 1963). In the crystal structure of

fassaite, the SiO_4 tetrahedra, share corners with two neighbouring tetrahedra to form chains of

SiO_4 tetrahedra, referred to as the tetrahedral chain. The tetrahedral chains are then linked

together by CaO_8 polyhedra and MgO_6 octahedra. The final error on the Allende TS62B and

USNM 3529 fassaite structure solution converged to R = 2.62 %, wR2 = 4.89 % and R = 1.79 %,

wR2 = 7.35 %, respectively. In both crystal structure solutions, the residual electron density

peaks on the final Fourier map were less than $1e^-/Å^3$.
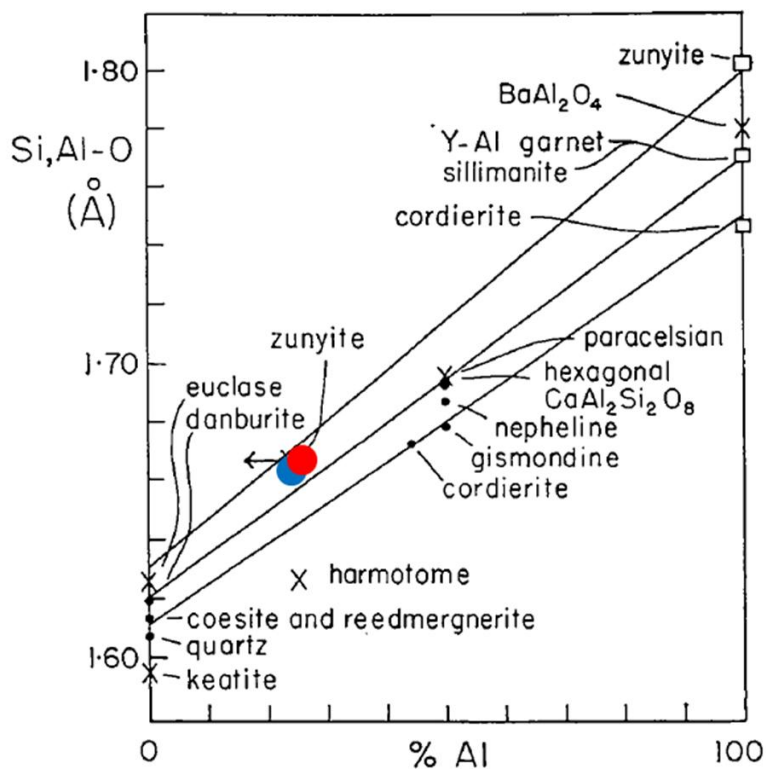
Figure 4.2. Average Si-O bond length of Allende TS62B (red) and USNM 3529 (blue) fassaite. plotted on an average Si-O bond length vs. % tetrahedral Al chart. The diagonal lines in order of increasing Si-O bondlength represent theoretical trends for framework, ring, and nesosilicates. Chart adapted from Smith and Bailey (1963).

Table 4.8. Interatomic distances (Å) in Allende fassaite
TS62B

CaO$_8$ Polyhedron			SiO$_4$ Tetrahedron		
Ca	-O2x2	2.388(3)	*Si*	-O3	1.627(3)
	-O3x2	2.391(3)		-O2	1.653(3)
	-O1x2	2.542(3)		-O1	1.684(3)
	-O1x2	2.676(3)		-O1`	1.710(3)
<Ca	-O>	2.499	*<Si*	-O>	1.669

MgO$_6$ Octahedron

Mg	-O3x2	1.998(3)
	-O2x2	2.046(3)
	-O1x2	2.102(3)
<Mg	-O>	2.049

Table 4.9. Interatomic distances (Å) in Allende fassaite USNM
3529

CaO$_8$ Polyhedron			SiO$_4$ Tetrahedron		
Ca	-O3x2	2.375(1)	*Si*	-O3	1.628(1)
	-O2x2	2.381(1)		-O2	1.644(1)
	-O1x2	2.529(1)		-O1	1.679(1)
	-O1x2	2.659(1)		-O1`	1.697(1)
<Ca	-O>	2.486	*<Si*	-O>	1.662

MgO$_6$ Octahedron

Mg	-O3x2	1.985(1)
	-O2x2	2.031(1)
	-O2x2	2.094(1)
<Mg	-O>	2.037

4.3.3 ²⁹Si MAS NMR

Three peaks, were resolved in the ²⁹Si MAS NMR spectrum of Allende TS62B fassaite, at -81.4, -84.4, and -90.1 ppm, consistent with spectra for synthetic Di-CaTs samples (Flemming & Luth 2002). When fitted using a full width half maximum (FWHM) of 3 ppm, relative peak intensities show that 54 % of Si atoms in Allende fassaite have one Al next nearest neighbor (NNN) on the tetrahedral single chain, 34% of Si alternate with Al in the chain (2 Al NNN), and 12% of Si have no Al NNN.
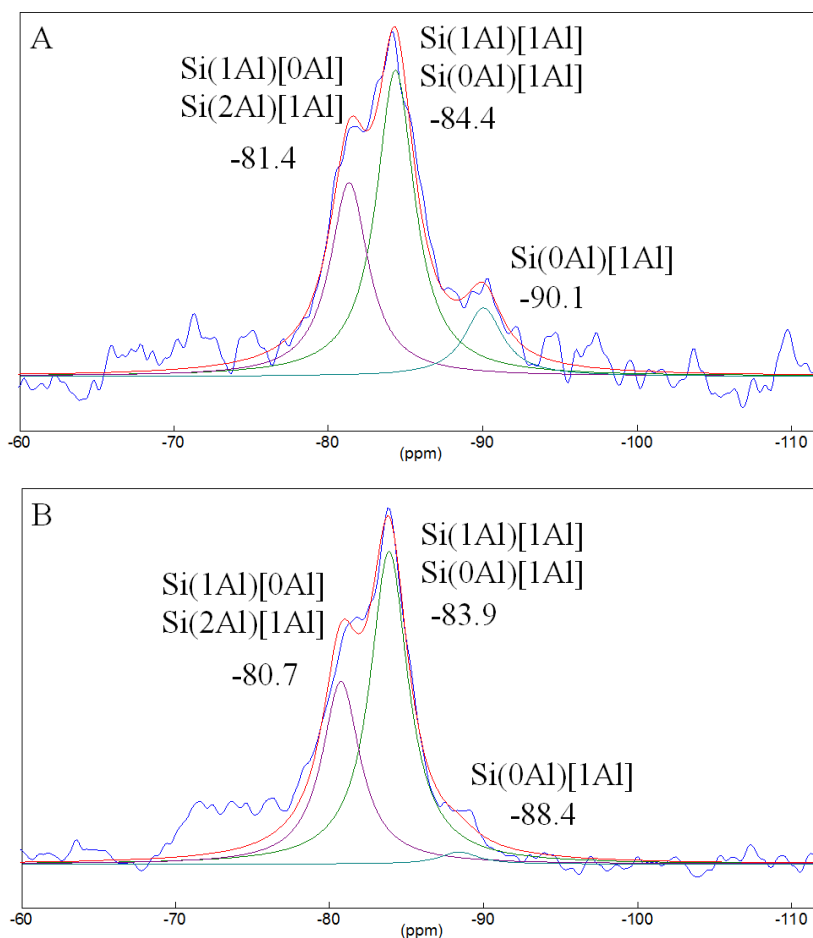
Figure 4.3. a)TS62B fassaite and b) USNM 3529 fassaite with deconvolution and peak assignments. ( ) and [ ] represent tetrahedral and octahedral NNN, respectively. Terminology for the site assignments is adopted from Flemming and Luth (2002).

Table 4.10. ^{29}Si MAS NMR peak parameters for Allende TS62B and USNM 3529 fassaite.			
Allende TS62B fassaite			
Peak Interpretation	Position (ppm)	FWHM (ppm)	Amplitude
Si(1Al)[0Al] + Si(2Al)[1Al]	-81.4	3	21.8
Si(1Al)[1Al] + Si(0Al)[1Al]	-84.4	3	34.4
Si(0Al)[1Al]	-90.1	3	7.7
Allende USNM 3529 fassaite			
Si(1Al)[0Al] + Si(2Al)[1Al]	-80.7	3	39.15
Si(1Al)[1Al] + Si(0Al)[1Al]	-83.9	3	66.81
Si(0Al)[1Al]	-88.4	3	7.8

Table 4.11. Percentage of Si with two, one, and no tetrahedral Al next nearest neighbours (NNN) in Allende TS62B and USNM 3529 fassaite.

Fassaite Sample	% Si with 2 tetrahedral Al NNN	% Si with 1 tetrahedral Al NNN	% Si with 0 tetrahedral Al NNN
Allende TS62B	34	54	12
Allende USNM 3529	36	62	2

The ^{29}Si MAS NMR spectrum of USNM 3529 fassaite was very similar to that of the Allende fassaite with three peaks at -80.7, -83.9, and -88.4 ppm each with a FWHM of 3 ppm. Relative peak intensities show that 62% of Si atoms in USNM 3529 fassaite have at least one Al next nearest neighbour on the tetrahedral single chain, 36% of Si alternate with Al in the chain (2Al NNN), and 2% of Si have no Al NNN. These results indicate the presence of short range disorder on the tetrahedral chain consistent with the $C2/c$ symmetry of the fassaite samples.
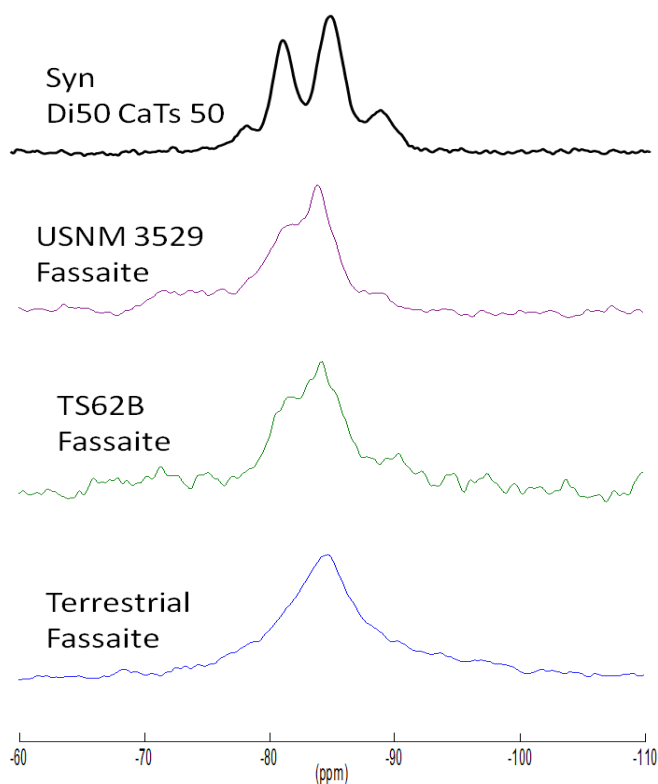
Figure 4.4. ^{29}Si MAS NMR spectra for synthetic $Di_{50}CaTs_{50}$ fassaite, Allende
TS62B and USNM 3529 fassaite, and terrestrial fassaite from Fassa Valley
Italy (Chapter 3). All spectra were collected at 21.1 Tesla except for synthetic
$Di_{50}CaTs_{50}$ which was collected by Flemming & Luth (2002) at 7.05 Tesla.

Both ^{29}Si MAS NMR spectra from the Allende TS62B and USNM 3529 fassaite are

broadly similar to the ^{29}Si NMR spectrum $Di_{50}CaTs_{50}$, a synthetic fassaite (Flemming and Luth

2002) which has a composition similar to the two Allende samples. The ^{29}Si NMR spectra of

Allende TS62B and USNM 3529 both have better resolution than the ^{29}Si NMR spectrum for

terrestrial fassaite likely due to cation ordering or compositional differences (see terrestrial

fassaite Chapter 3).

4.3.4 ^{27}Al MAS NMR

The ^{27}Al MAS NMR spectra of both the TS62B and USNM fassaite show two distinct

sets of peaks, broadly similar to synthetic CaTs (Flemming et al. in prep). In both Allende

fassaite samples the two sets of peaks occur in regions at ~ 50 to 80 ppm and ~ 15 to -20 ppm

and represent tetrahedral and octahedral sites, respectively, as is well documented (Kirkpatrick

1988). The two narrow octahedral peaks demonstrate cation ordering in the six tetrahedral sites

bonded to octahedral Al. Due to quadrupolar broadening effects, accurate deconvolution of the

tetrahedral sites in the MAS spectrum could not be completed
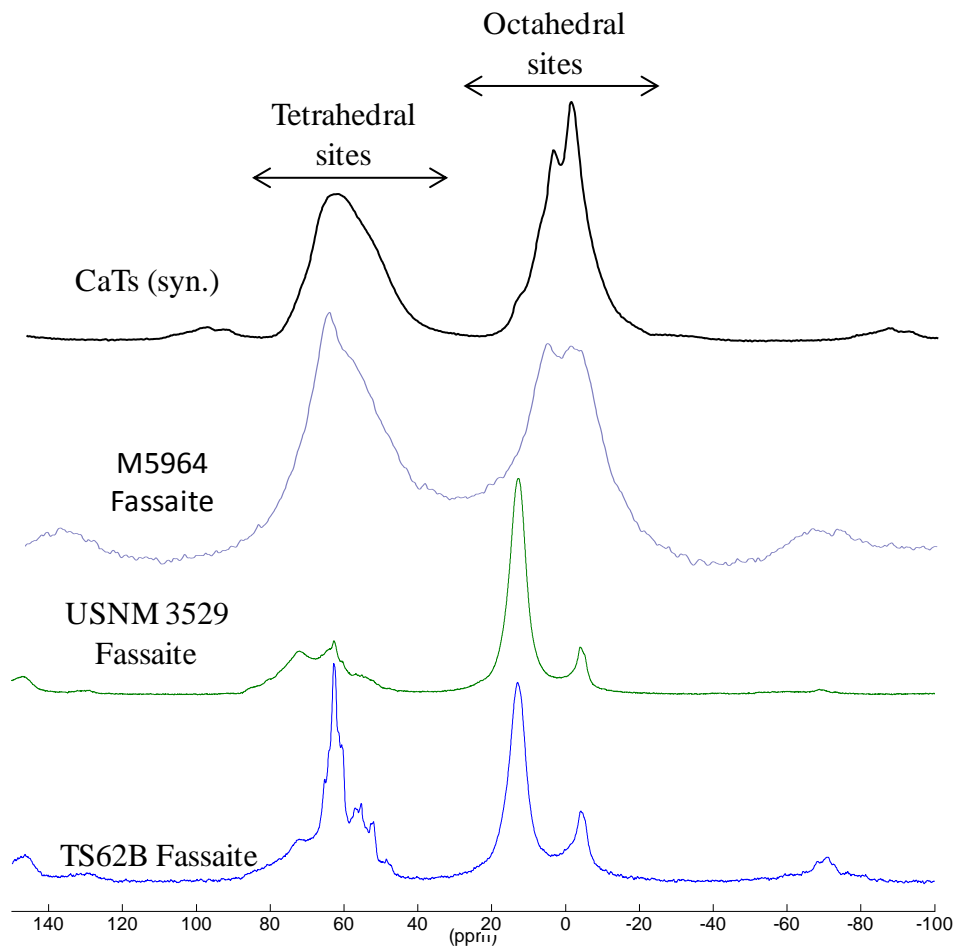
Figure 4.5. Comparison of ^{27}Al MAS NMR spectra of synthetic CaTs (Flemming et al., in prep), Fassa Valley fassaite (M5964 fassaite), USNM fassaite, and TS62B fassaite.

4.3.5 ^{27}Al MQMAS NMR

The ^{27}Al MQMAS NMR spectra of the two Allende fassaite samples taken at 21.1 T is shown below in Figure 4.6. Note the MAS NMR dimension (F2) is shown at the top of the figure and the isotropic chemical shift dimension (F1) is shown on the y-axis; both dimensions are in ppm. The ^{27}Al 3QMAS NMR spectrum of the two Allende fassaite samples provides additional resolution of the tetrahedral sites showing at least five peaks in 2D. The five peaks

represent five different tetrahedral aluminum sites and have narrow peak widths along the F1 dimension, indicating ordering on the tetrahedral site. In addition, the five tetrahedral peaks show broadening along the F2 dimension such that their intensities do not follow the 1:1 correspondence line (where F1 = F2). This indicates significant quadrupolar effects on the tetrahedral sites implying that they are highly distorted from regular symmetry (having a high electric field gradient) consistent with the recorded Si-O bondlengths (Tables 4.7 & 4.8). Slices through the 5 tetrahedral peaks have been made (See Appendix 5) in order to fit the quadrupolar parameters using DMFit (Massiot 2011). The fitted parameters are given in Tables 4.12 and 4.13.
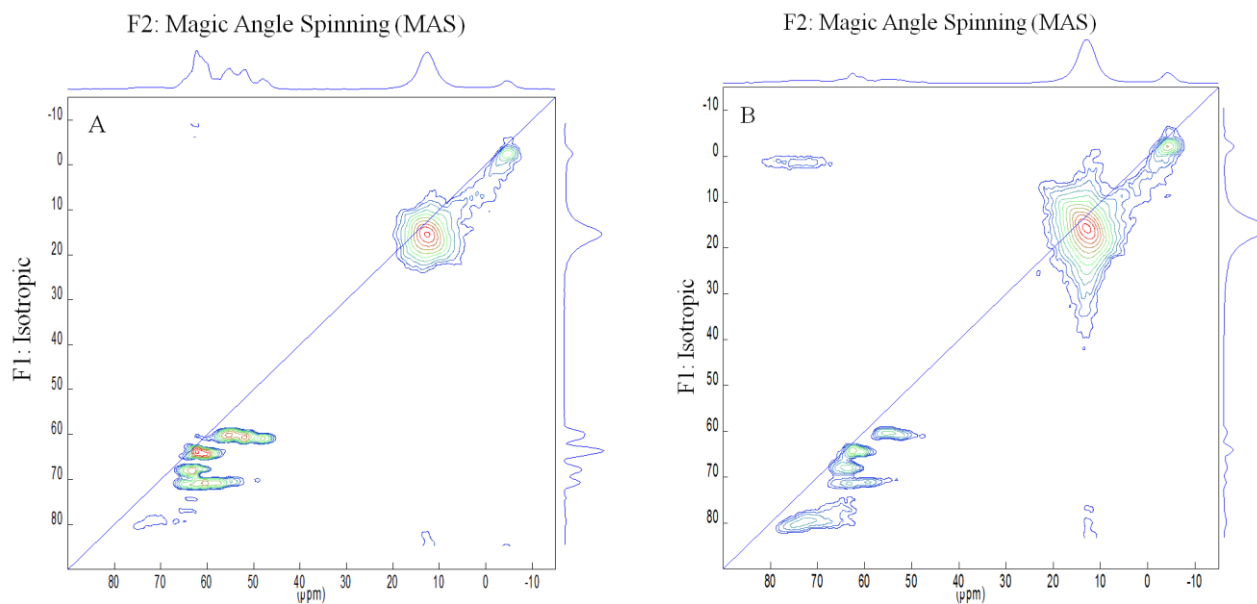
Figure 4.6. ^{27}Al MQMAS spectra for a) TS62B fassaite and b) USNM 3529 fassaite.

Table 4.12. Peak Parameters for tetrahedral peaks from Allende TS62B fassaite.				
Peak #	Position (ppm)	Amplitude	CQ (kHz)	etaQ
1	58.37	264.48	6634.75	0.25
2	63.96	531.04	4692.50	0.30
3	66.20	253.54	4809.92	0.90
4	66.68	210.63	7477.52	0.65
5	79.27	31.99	9242.45	0.50
Peak Parameters for octahedral peaks from Allende TS62B fassaite.				
Peak #	Position (ppm)	Amplitude	Width (ppm)	xG/(1-x)L
1'	12.62	225.38	4.50	0.50
2'	-4.63	52.59	3.24	0.50

Table 4.13. Peak Parameters for tetrahedral peaks from Allende USNM 3529 fassaite.				
Peak #	Position (ppm)	Amplitude	CQ (kHz)	etaQ
1	58.87	159.19	6487.55	0.35
2	64.29	379.68	4548.09	0.30
3	67.33	212.40	5525.99	0.40
4	68.32	130.37	7766.00	0.40
5	79.00	`118.59	8930.92	0.30
6	87.23	74.28	10202.43	0.48
Peak #	Position (ppm)	Amplitude	Width	xG/(1-x)L
1'	12.94	807.60	4.23	0.50
2'	-4.31	195.04	2.97	0.50
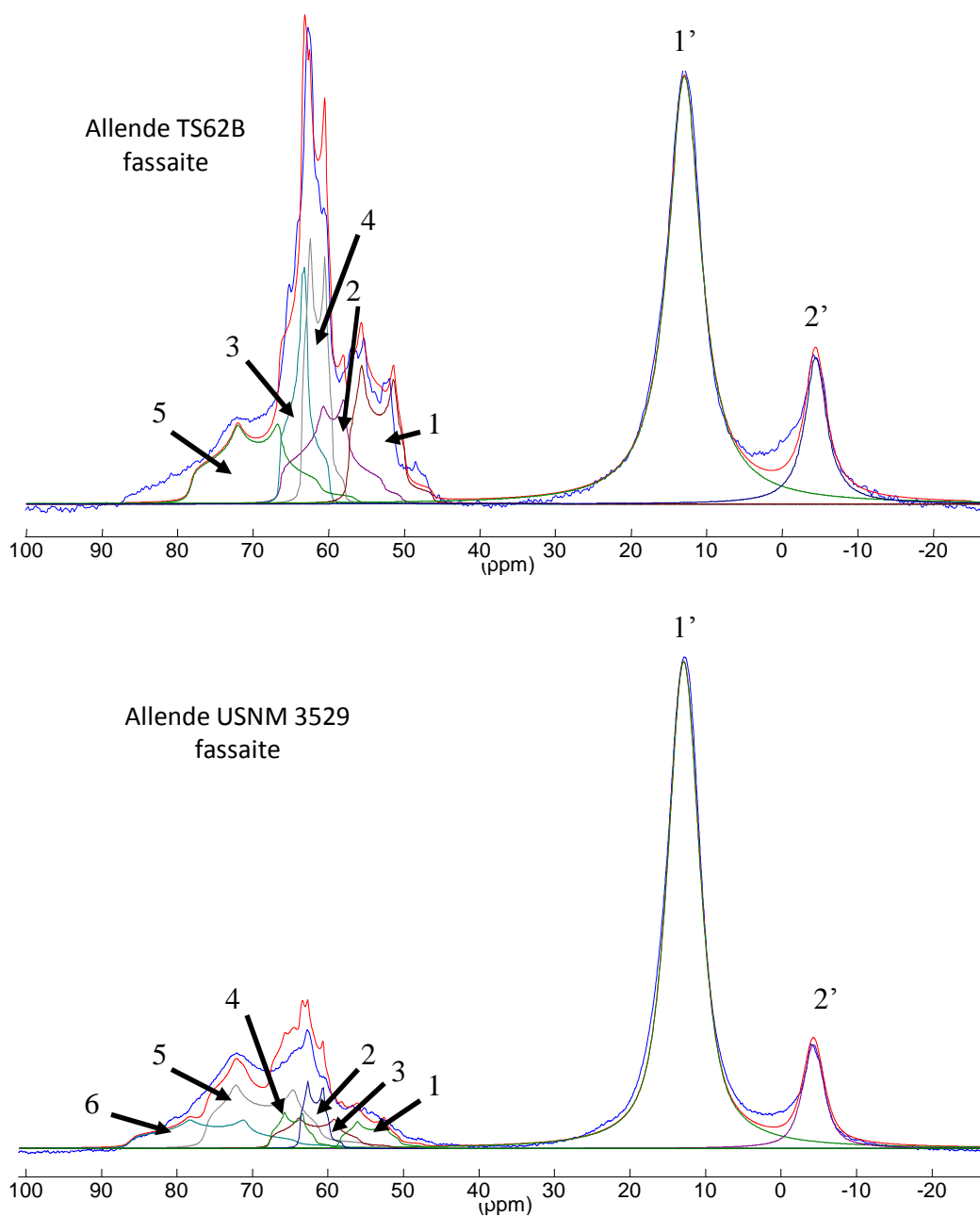
Figure 4.7 ^{27}Al MAS NMR spectra for Allende TS62B and USNM 3529 fassaite with fitted peaks. The peak parameters are listed in tables 4.12 and 4.13.

4.4 Discussion

4.4.1 Octahedral sites

For both Allende TS62B and USNM 3529 fassaite, two well-resolved octahedral peaks are observed in both the ^{27}Al MAS NMR and ^{27}Al 3Q MAS NMR spectra. Because the octahedral sites in fassaite are linked through shared corners to the tetrahedral chain, any Al/Si cation ordering will likely have an effect on the octahedral sites resulting in multiple octahedral peaks in ^{27}Al NMR spectra. This coupling of octahedral and tetrahedral sites was directly observed by Flemming & Luth (2002) who found that substitution of Mg by Al on the octahedral site has an effect on the ^{29}Si MAS NMR spectra of synthetic fassaite and CaTs pyroxene ($CaAl(AlSi)O_6$). Each octahedral site in fassaite is linked to six tetrahedral sites through shared corners as well as two neighbouring octahedral sites through shared edge (see Figure 3.1 in Chapter 3). If the tetrahedral chain in fassaite is fully ordered (i.e. alternating Al and Si : Al-O-Si-O-Al-O-Si) then there are three possible environments around the octahedral site: 4Si + 2Al, 3Si + 3Al, 2Si + 3Al (Flemming et al. in prep). Flemming & Luth 2002 found that the tetrahedral chains in CaTs pyroxene are 70% ordered (i.e. 70% of the Si atoms have two Al next nearest neighbours (NNN)) however, it was also found that the tetrahedral chains contained 13% Al-O-Al linkages indicating that there is some disordering as well on the tetrahedral chain. If disordering on the tetrahedral chain is considered, then there are as many as 15 possible environments around the octahedral site including a 5Al + 1Si environment (Flemming et al. in preparation). Both Allende fassaite samples exhibit two octahedral peaks, occurring at ~ 13 and -4 ppm. The peak at 13 ppm for both Allende samples is consistent with the 4Al + 2Si environment found in the ^{27}Al NMR spectrum of synthetic CaTs by Flemming et al. (in prep.).

Substituting Al for Si in neighbouring tetrahedral sites deshields the octahedral Al resulting in octahedral peaks occurring at a more positive ppm (Flemming et al. in prep., Kirkpatrick 1988). Based on this, the second octahedral peak occurring at ~ -4 ppm is the result of a highly shielded octahedral Al; therefore the possible surrounding environment could be 1Al + 5Si. The 1Al + 5Si environment indicates that there is still some Al/Si disordering on the tetrahedral chain [or does it indicate simply more silicon than aluminum in the structure?] however, the lower intensity of the disordered 1Al + 5Si environment relative to the intensity of the ordered 4Al + 2Si environment indicates that the tetrahedral chains surrounding the octahedral sites are mostly ordered. In addition, the narrow octahedral peaks (FWHM ~ 4.5 ppm) are an indication of Al/Si ordering on the tetrahedral environments. These site assignments in the Allende fassaite samples are approximations based on the study of synthetic CaTs by Flemming et al. (in prep). In CaTs, all octahedral sites are occupied by Al (fully ordered) and therefore octahedral order/disorder does not contribute to multiple octahedral peaks (Flemming et al. in prep), however, fassaite octahedral sites may be occupied by Mg or Al resulting in potential Mg/Al order/disorder. A Monte Carlo simulation by Warren et al. (2001) suggested that alternating Mg and Al octahedra is the most favourable configuration in fassaite containing a 50% CaTs component. Because the Allende fassaite samples contain a considerable CaTs (~ 50% CaTs) component, synthetic CaTs serves as a reasonable comparison to Allende fassaite. To understand the effects of Mg/Al ordering in octahedral sites, further ^{27}Al NMR studies of fassaite with variable CaTs components is necessary.

4.4.2 Tetrahedral Sites

At least five well-resolved peaks are visible in the [27]3QMAS NMR spectra of the Allende fassaite samples, representing tetrahedral aluminum environments. Fassaite is often found

intergrown with melilite (Ca_2AlSiO_7) in CAIs (Brearley & Jones 1998). The tetrahedral peaks in

fassaite occur at ~ 80 to 50 ppm whereas the tetrahedral peaks of melilite occur at ~ 90 to 40

ppm (Florian et al. 2012) therefore there is some contribution from melilite to the tetrahedral

fassaite peaks. A recent ^{27}Al MQMAS NMR study of melilite found that higher proportions of

Si NNN around tetrahedral Al results in tetrahedral peaks occurring at lower ppm (Florian et al.

2012). Assuming this chemical shift also occurs in the tetrahedral sites of fassaite, the four peaks

centered at ~ 60, 65, 68, and 71 ppm (along F1) likely represent Al(2Si)[0Al], Al(1Si)[0Al] +

Al(2Si)[1Al], Al(0Si)[0Al] + Al(1Si)[1Al], and Al(0Si)[1Al] respectively, where ( ) is a

tetrahedral NNN and [ ] is an octahedral NNN (Fig 4.8). The fifth peak centered at ~ 80 ppm

along F1 is consistent with peaks in the ^{27}Al MQMAS NMR spectra of both melilite (Florian et

al. 2012) and CaTs pyroxene (Flemming et al. in prep) (Fig. 4.8). Due to the lower intensity of

this fifth peak relative to the first four peaks, it is most likely that the fifth peak is from melilite.

The spectrum of Allende USNM 3529 fassaite contains a sixth tetrahedral peak at ~ 96 ppm

along F1, which is also consistent with a peak in the ^{27}Al MQMAS NMR spectrum of melilite

(Florian et al. 2012, Warren et al. 2001). The four tetrahedral peaks associated with fassaite are

narrow along the F1 dimension indicating local ordering of the tetrahedral aluminum sites.
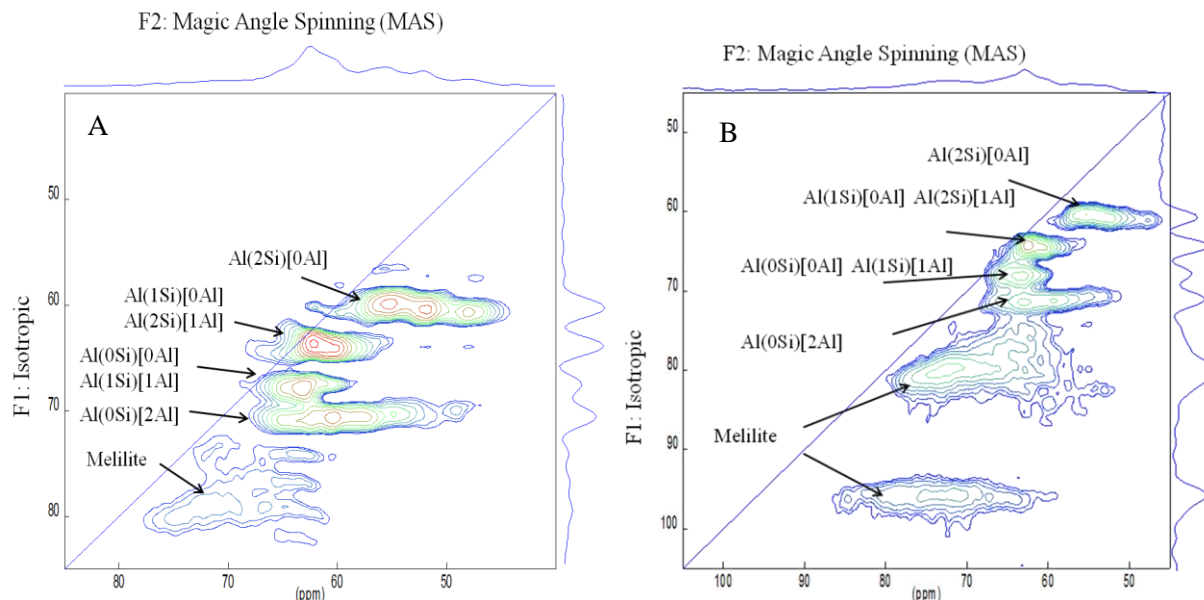
Figure 4.8. Close up of tetrahedral peaks from the ^{27}Al 3QMAS NMR spectra of a) Allende TS62b and b) Allende USNM 3529 fassaite.

4.4.3 Allende Fassaite Vs. Fassa Valley Fassaite

As observed in Fig. 4.4 and Fig. 4.5, the peaks in the ^{29}Si and ^{27}Al MAS NMR spectra of Allende fassaite are sharper and better resolved than those of Fassa Valley fassaite. This could be a reflection of the different composition of the two fassaite samples.   Fassaite samples from meteorites like Allende tend to have very little or no Fe (Brearley & Jones; thus NMR peaks undergo less broadening. Another important consideration is that Fassa Valley fassaite and Allende fassaite have had very different thermal histories. Cation ordering is highly temperature dependent (Etzel et al. 2007) and will likely reflect the different thermal histories of the fassaite samples. From the ^{27}Al MAS NMR spectra (Fig. 4.5) of Fassa Valley fassaite and Allende fassaite, Allende fassaite appears to have more short range cation ordering than Fassa Valley fassaite as is reflected in the sharper better resolved peaks for Allende fassaite. Both fassaite samples however, have long-range disordering as is reflected in their *C*2/*c* symmetry (Okamura et al. 1974).

4.4.4 Al/Si Cation ordering in Allende Fassaite

Allende TS62B and USNM 3529 fassaite have $C2/c$ symmetry, consistent with long range Al/Si cation disorder within their crystal structures (Okamura et al. 1974). From the ^{29}Si and ^{27}Al NMR results discussed above, the two Allende fassaite samples have locally ordered Al/Si domains as is suggested by Cohen & Burnham 1985 and Grove & Burnham 1974. Long range ordered fassaite has yet to be discovered in nature or synthesized in a lab. Monte Carlo simulations by Bosenick et al. (2001) and Warren et al. (2001) indicate that fassaite undergoes a transition from a disordered to ordered arrangement at just under 1000 K. Assuming complete Al-avoidance, there are four fully ordered crystal structures possible for fassaite including $C1$, $C\bar{1}$, $P2/n$, and $P2_1/n$ of which $P2_1/n$ is the most energetically favourable (Bosenick et al. 2001, Warren et al. 2001, Okamura et al. 1974). A possible explanation for the lack of fully ordered fassaite structures is that the temperature at which ordered fassaite is stable coincides with the stability field of grossular and corundum (Warren et al. 2001). At temperatures within the stability field of grossular and corundum, Gasparik (1984) found that CaTs pyroxene (an important component of fassaite) is unstable and breaks down according to the following equation: $3CaAl_2SiO_6 \leftrightarrow Ca_3Al_2Si_3O_{12} + 2Al_2O_3$. The ordered domains within the Allende fassaite samples most likely represent cation ordering above the transition temperature (under 1000 K) to a fully ordered fassaite structure. The Allende meteorite is hypothesized by Elkins-Tanton et al. (2011) to have come from the crust a parent body ~ 200 km in radius where it was exposed to temperatures of ~ 870 K. At ~870 K, the Allende meteorite was subjected to temperatures close to the transition to a fully ordered structure to allow for locally ordered domains to form within the disordered ($C2/c$) Allende fassaite samples.

References

Benna, P., Tribaudino, M., and Bruno, E. (1988) *Crystal structure of Di50CaTs50 synthetic clinopyroxene (CaMg0.5AlSi1.5O6). Crystal chemistry along the Di-CaTs join.* Mineralogy and Petrology, **Vol.** 38, 189-200.

Bosenick, A., Dove, M.T., Myers, E.R., Palin, E.J., Sainz-Diaz, C.I., Guiton, B.S., Warren, M.C., Craig, M.S., and Redfern, S.A.T. (2001) *Computational methods for the study of energies of cation distributions: applications to cation-ordering phase transitions and solid solutions.* Min. Mag., **Vol.** 65, 193-219.

Brearley, A.J. & Jones, R.H. Chondritic Meteorites. Rev. Min. 36, Chapter 3 (1998).

Cohen, R.E. and Burnham, C.W. (1985) Energetics of ordering in aluminous pyroxenes. Am. Min., **Vol.** 70, 559-567.

Cromer, D.T. & Liberman, D. (1970) *Relativistic calculation of anomalous scattering factors for X-rays.* J. Phys. Chem. **Vol.** 53, 1891-1898.

Deer, W.A., Howie, R.A., & Zussman, J. (1978) *Rock-Forming Minerals: Single Chain Silicates 2nd edition*, **Vol**. 2A, Longman Group Ltd. pp 399-414.

Dowty, E., & Clark, J.R (1973) *Crystal Structure Refinement and Optical Properties of a Ti^{3+} Fassaite from the Allende Meteorite*. Am. Min. **Vol.** 58, 230-242

Elkins-Tanton, L., Weiss, B.P., & Zuber, M.T. (2011) *Chondrites as samples of differentiated planetesimals.* Earth and Planetary Science Letters, doi:10.1016/j.epsl.2011.03.010.

Etzel, K., & Bensiek, A. (2008) *Thermodynamic mixing behavior of synthetic Ca-Tschermak-diopside pyroxene solid solutions: III. An analysis of IR line broadening and heat of mixing behavior.* Phys. Chem. Mineral. **Vol.** 35, 399-407.

Etzel, K., Bensiek, A., Dachs, E., & Cemic, L. (2007) *Thermodynamic mixing behavior of synthetic Ca-Tschmak-Diopside pyroxene solid solutions: I. Volume and Heat Capacity.* Phys. Chem. Minerals. **Vol.** 34, 733-746.

Flemming, R.L., Teskikh, V., Ye, E., and Wu, G. (2012). *Aluminum environments in Ca-Tschermak's clinopyroxene (CaTs) from ^{27}Al MAS NMR and ^{27}Al 3QMAS NMR*. In Preparation.

Flemming, R.L. & Pawsey, S. (2007) *^{27}Al 3QMAS NMR Spectroscopy of Aluminous Clinopyroxene ay 11.7 and 21.1 Tesla.* National Research Council Canada Annual Report 2006-2007.

Flemming, R.L. and Luth, R.W. (2002) *^{29}Si MAS NMR study of diopside – Ca-Tschermak clinopyroxenes: Detecting both tetrahedral and octahedral Al*. Am. Min, **Vol.** 87, 25-36.

Florian, P., Vernon, E., Green, T.F.G., Yates, J.R., and Massiot, D. (2012) *Elucidation of the Al/Si Ordering in Gehlenite Ca2Al2SiO7 by combined ^{29}Si and ^{27}Al NMR Spectroscopy/Quantum Chemical Calculations.* Chem. Mat. In Press.

Frydman, L. And Harwood, J.S., (1995)*Isotropic Spectra of Half-Integer Quadrupolar Spins from Bidimensional Magic-Angle Spinning NMR*. J. Am. Chem. Soc., **Vol.** 117, 5367-5368.

Gasparik, T. (1984) *Experimentally determined stability of clinopyroxene + garnet + corundum in the system $CaO-MgO-Al_2O_3-SiO_2$.* Am. Min. **Vol.** 69, 1025-1035.

Grossman, L. (1975) *Petrography and mineral chemistry of Ca-rich inclusions in the Allende meteorite*. Geochim. Cosmochim. Acta. **Vol.** 39, 433-454.

Hazen, R.M. & Finger, L.W. (1977) *Crystal Structure and Compositional Variation of Angra Dos Reis Fassaite.* Earth and Planetary Science Letters, **Vol.** 35, 357-362.

Kirkpatrick, J. (1988)*MAS NMR Spectroscopy of Minerals and Glasses*. Rev. Min. **Vol.** 18, 341.

Kentgens, A.P.M., (1997) *A Pratical Guide to Solid-State NMR of half Integer Quadrupolar Nuclei with Some Applications to Disordered Systems*. Geoderma, **Vol.** 80, 271-306.

Marvin, U.B., Wood, J.A., and Dickey Jr., J.S.(1970) *Ca-Al rich phases in the Allende meteorite.* Earth and Planetary Science Letters. **Vol.** 70, 346-350.

Mittlefehld, D.W., Killgore, M., and Lee, M.T. (2002) *Petrology and geochemistry of D'Orbigny, geochemistry of Sahara 99555, and the origin of angrites*. Meteoritics and Planetary Science, **Vol.** 37, 345-369.

Oberti, R., Munno, R., Foresti, E., & Krajewsky, A. (1982) *A Crystal-Chemical Strudy on Six Fassaites From the Predazzo-Monzoni Area.* Soc. Ital. Min. Petr. **Vol.** 38, 649-655.

Okamura, F.P., Ghose, S., and Ohashi, H. (1974) *Structure and crystal chemistry of calcium Tschermak's pyroxene, $CaAlAlSiO_6$.* Am. Min., **Vol** 59, 549-557.

Peacor, D.R. (1967)*Refinement of the Crystal Structure of a Pyroxene of Formula $M_IM_{II}(Si_{1.5}Al_{0.5})O_6$.* Am. Min. **Vol.** 52, 31-41.

Phillips, B.L., Allen, F.M., and Kirkpatrick, J.R., (1987) *High-resolution Solid-state ^{27}Al NMR spectroscopy of Mg-rich Vesuvianite.* Am. Min. **Vol.** 72, 1190-1197.

Sheldrick, G.M. (1997): SHELXL-97: *A computer program for the Refinement of Crystal Structures.* Univ. of Göttingen, Göttingen, Germany.

Simon, S.B., Grossman, L., & Davis, A.M. (1991) *Fassaite composition trends during crystallization of Allende Type B refractory inclusion melts*. Geochim. Cosmochim. Acta. **Vol.** 55, 2635-2655.

Smith, J.V., & Bailey S.W. (1963) *Second Review of Al-O and Si-O Tetrahedral Distances*. Acta. Cryst. **Vol.** 16, 801-811.

Warren, M.C., Dove, D.T., Myers, E.R., Bosenick, A., Palin, E.J., Sainz-Diaz, C.I., Guiton, B.S., and Redfern, S.A.T. (2001). *Monte Carlo methods for the study of cation ordering in minerals.* Min. Mag. **Vol**. 65, 221-248.

CHAPTER 5: Conclusions

From single crystal XRD and crystal structure refinements, the space group symmetry of the Fassa Valley fassaite and the two Allende fassaite samples was determined to be C2/c, consistent with long range cation disorder (Okamura et al. 1974). ^{29}Si and ^{27}Al NMR spectroscopy methods were used to determine local Al/Si cation ordering in the fassaite samples. The ^{29}Si MAS NMR spectra of Fassa Valley fassaite contained one broad (FWHM ~ 10 ppm) peak centered at ~ 84 ppm. The broadness of this peak may indicate the presence of Si/Al cation disordering in the form of Al-O-Al linkages along the tetrahedral chain of Fassa Valley fassaite. ^{27}Al MAS NMR and ^{27}Al 3QMAS NMR spectra show poorly-resolved, broadened tetrahedral peaks that are also consistent with the presence of Al/Si cation disordering in the tetrahedral sites of Fassa Valley fassaite. Although the tetrahedral peaks in the ^{27}Al MAS NMR and ^{27}Al 3QMAS NMR spectra of Fassa Valley fassaite are poorly resolved, two octahedral Al peaks are observed and are inferred to be surrounded by 2Al+4Si and 3Al+3Si tetrahedral environments.

The ^{29}Si and ^{27}Al NMR spectra of the two Allende fassaite samples were better resolved than the spectra from Fassa Valley fassaite. The ^{29}Si MAS NMR spectra of the two Allende samples were very similar and contained three narrow (FWHM ~ 3 ppm) peaks at ~ -81, -84, and -89 ppm. From the intensities of these peaks, the tetrahedral chain in Allende TS62B fassaite was found to be 34% ordered (i.e. 34% of the Si cations have two Al NNN) whereas the tetrahedral chain in Allende USNM 3529 Fassaite was found to be 36% ordered (i.e. 36% of the Si cations have two Al NNN). The ^{27}Al MAS NMR spectra of Allende TS62B and Allende USNM 3529 fassaite contained 5 and 6 tetrahedral peaks respectively, at least one of which was attributed to small amounts of melilite that could be separated from the fassaite. Although some melilite was found in the fassaite samples, the narrow widths of the tetrahedral peaks along the

F1 dimension are consistent with Al/Si ordering domains in the tetrahedral sites. In addition to the five to six tetrahedral sites, two well resolved octahedral peaks were observed in the ^{27}Al MAS and 3QMAS NMR spectra of Allende TS62B and USNM 3529 fassaite. The two octahedral peaks are consistent with the 1Al + 5Si and 4Al + 2Si tetrahedral environments surrounding octahedral Al proposed by Flemming et al. (in prep). While the 1Al + 5Si environment indicates the presence of disordering (or more silicon than aluminum on the tetrahedral chain), the peak representing 4Al + 2Si has a higher intensity thus more ordered environments are inferred to surround octahedral Al. This is consistent with past studies of CaTs pyroxene by Flemming & Luth (2002) where the tetrahedral environments in CaTs were found to be 70% ordered. The effects on NMR spectra due to substitution of Al for Mg on the octahedral site in fassaite is still uncertain and will require further study of fassaite with varying amounts of Mg and Al on the octahedral site.

The differences in cation ordering between the terrestrial Fassa Valley fassaite and the two Allende fassaite samples may be a reflection of their differing environments of formation as well as compositions. The two Allende fassaite samples are suggested to have been subjected to temperatures of ~ 870 K (Elkins-Tanton et al. 2011) close to the transition temperature of under 1000 K (Warren et al. 2001, Bosenick et al. 2001), where fassaite goes from a long range disordered to long-range ordered structure. Based on this, it is likely that the ordered domains in the Allende fassaite represent short range cation ordering above the transition temperature to a fully ordered crystal structure. Unlike the Allende fassaite samples, the NMR spectra for the Fassa Valley fassaite contained poorly resolved peaks indicating the presence of local Al/Si cation disordering in addition to long range disordering as implied by the $C2/c$ space group symmetry. Since cation ordering is highly temperature dependant, with crystal structures

becoming more ordered at higher temperatures (Etzel et al. 2007), it is likely that the Fassa

Valley fassaite was subjected to higher temperatures than the Allende fassaite sample. In

addition Al/Si cation ordering on octahedral and tetrahedral sites in crystal structure of fassaite is

affected by pressure.   At high temperatures, Al is more likely to substitute for Si on tetrahedral

sites resulting in disordering of tetrahedral sites due to more Al-O-Al linkages but at high

pressure, Al is more likely to substitute for Mg in octahedral sites (Okamura & Ghose 1974).

Because Al is more likely to substitute for octahedral Mg and high pressure, there will be less Al

in tetrahedral sites and therefore more ordering of the tetrahedral sites due to fewer Al-O-Al

linkages on the tetrahedral chain. Disordering of the tetrahedral sites as suggested by broad

peaks in the ^{27}Al and ^{29}Si NMR spectra of Fassa Valley fassaite suggests that it crystallized at

relatively low pressures consistent with the contact metamorphic origin of fassaite in localities

similar to Fassa Valley Italy (Deer et al. 1978, Oberti et al. 1982) An accurate interpretation of

cation ordering in Fassa Valley fassaite, however is made difficult due to the iron content (avg.

FeO_{tot} = 3.97 wt %) which is enough to cause broadening in NMR peaks. Fully ordered fassaite

has yet to be discovered both in nature and in a lab setting, however, this study shows that it is

possible to observe ordered domains in natural fassaite using NMR spectroscopy provided that

the fassaite contains very little iron.

References

Deer, W.A., Howie, R.A., & Zussman, J. (1978) *Rock-Forming Minerals: Single Chain Silicates 2nd edition*, **Vol**. 2A, Longman Group Ltd. pp 399-414.

Elkins-Tanton, L., Weiss, B.P., & Zuber, M.T. (2011) *Chondrites as samples of differentiated planetesimals.* Earth and Planetary Science Letters, doi:10.1016/j.epsl.2011.03.010.

Etzel, K., Bensiek, A., Dachs, E., & Cemic, L. (2007) *Thermodynamic mixing behavior of synthetic Ca-Tschmak-Diopside pyroxene solid solutions: I. Volume and Heat Capacity.* Phys. Chem. Minerals. **Vol.** 34, 733-746.

Flemming, R.L., Teskikh, V., Ye, E., and Wu, G. (2012). *Aluminum environments in Ca-Tschermak's clinopyroxene (CaTs) from ^{27}Al MAS NMR and ^{27}Al 3QMAS NMR*. In Preparation.

Flemming, R.L. and Luth, R.W. (2002) ^{29}*Si MAS NMR study of diopside – Ca-Tschermak clinopyroxenes: Detecting both tetrahedral and octahedral Al*. Am. Min, **Vol.** 87, 25-36.

Oberti, R., Munno, R., Foresti, E., & Krajewsky, A. (1982) *A Crystal-Chemical Study on Six Fassaites From the Predazzo-Monzoni Area.* Soc. Ital. Min. Petr. **Vol.** 38, 649-655.

Okamura, F.P., Ghose, S., and Ohashi, H. (1974) *Structure and crystal chemistry of calcium Tschermak's pyroxene, CaAlAlSiO$_6$.* Am. Min., **Vol** 59, 549-557.

Appendix 1

Separating CAIs from the Allende meteorite

In addition to Fassa Valley fassaite and Allende TS62B and USNM 3529 fassaite, a 13 g piece of the Allende meteorite containing several CAIs was provided by the Institute of meteoritics. The CAIs were separated from the Allende Cr.3.7c sample using freeze-thaw disaggregation at the University of Toronto. Before extracting the CAIs, Allende Cr.3.7c was soaked in distilled water for five days prior to disaggregation. Disaggregation of Cr3.7.c involved freeze-thaw cycles lasting 21.5 minutes each in which the sample, placed within a Teflon container and covered with distilled water, was soaked in warm (80 °C) water for 14 minutes, rested in air of 30 seconds and was then soaked in liquid nitrogen for 7 minutes. A total of 85 freeze-thaw cycles were needed to fully disaggregate Allende Cr.3.7c. The freeze-thaw cycles were completed using an apparatus (Fig. 1) consisting of a motorized arm that lifted the Teflon container out of the warm water and moved it over to a dewer of liquid nitrogen.
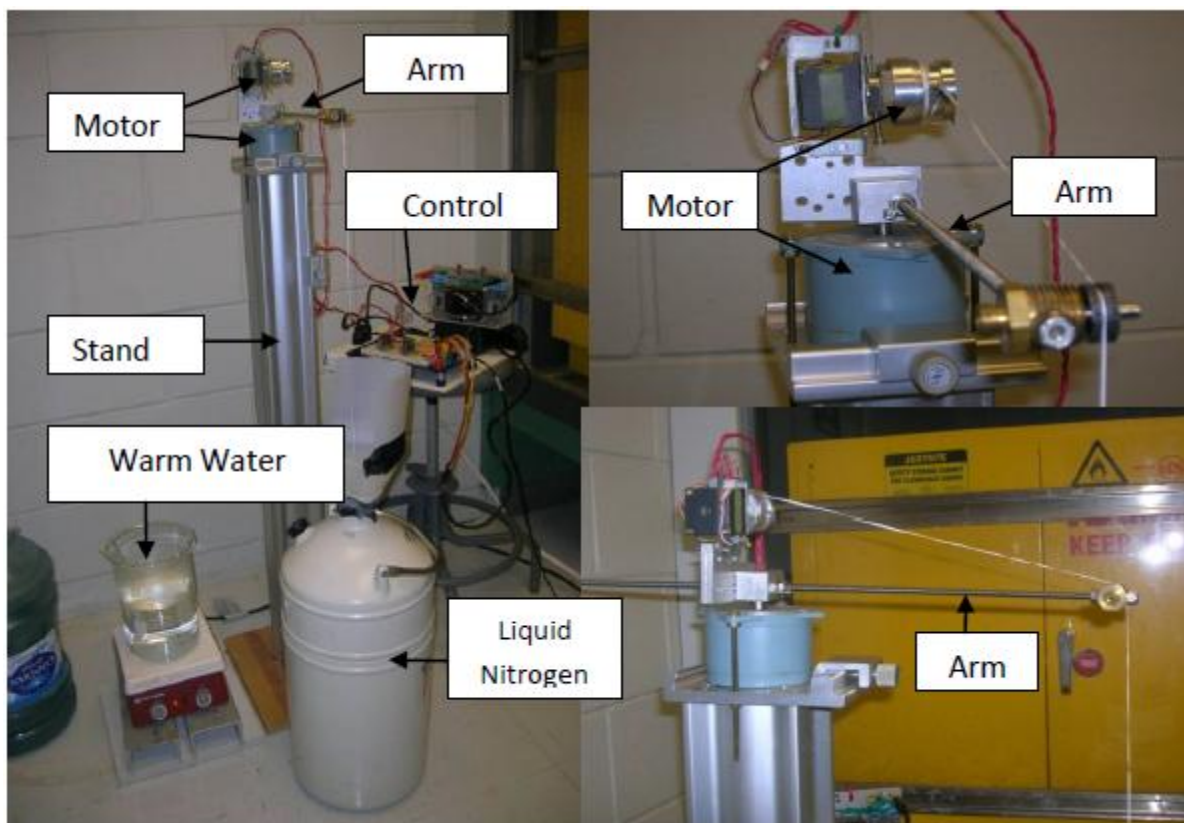
Figure 1. Freeze-thaw disaggregation apparatus used to extract CAIs from Allende Cr.3.7c. Photos by Monika Haring

Once Allende Cr.3.7c was disaggregated, the sample was placed in a petri dish (Fig. 2a).

Due to the fragile nature of CAIs, CAI extraction was performed under a microscope by

immersing the sample in medical grade alcohol and sucking up the CAIs with pipettes. The

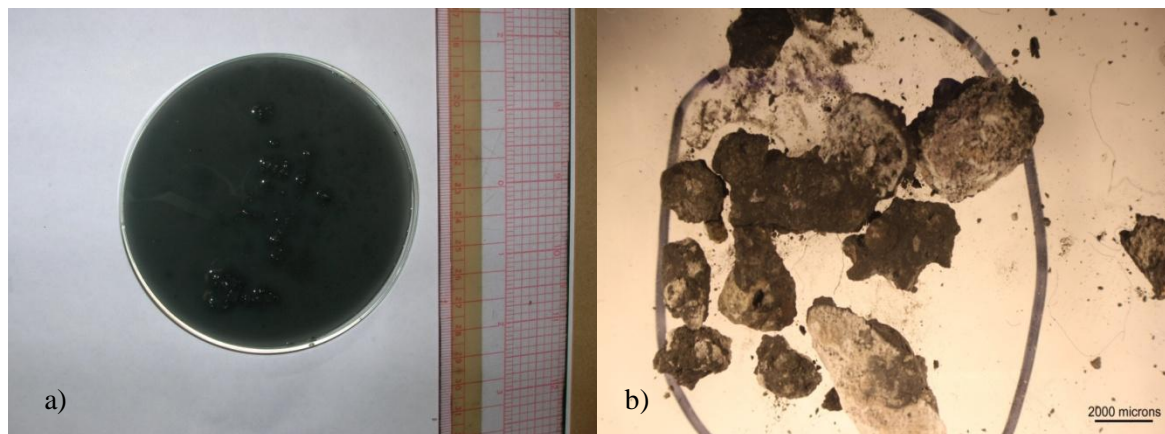CAIs were then moved to a clean petri dish (Fig. 2b).

Figure 2. a) Allende Cr.3.7c after 85 freeze-thaw cycles and b) some CAIs (whitish grey fragments) extracted from Allende Cr.3.7c.
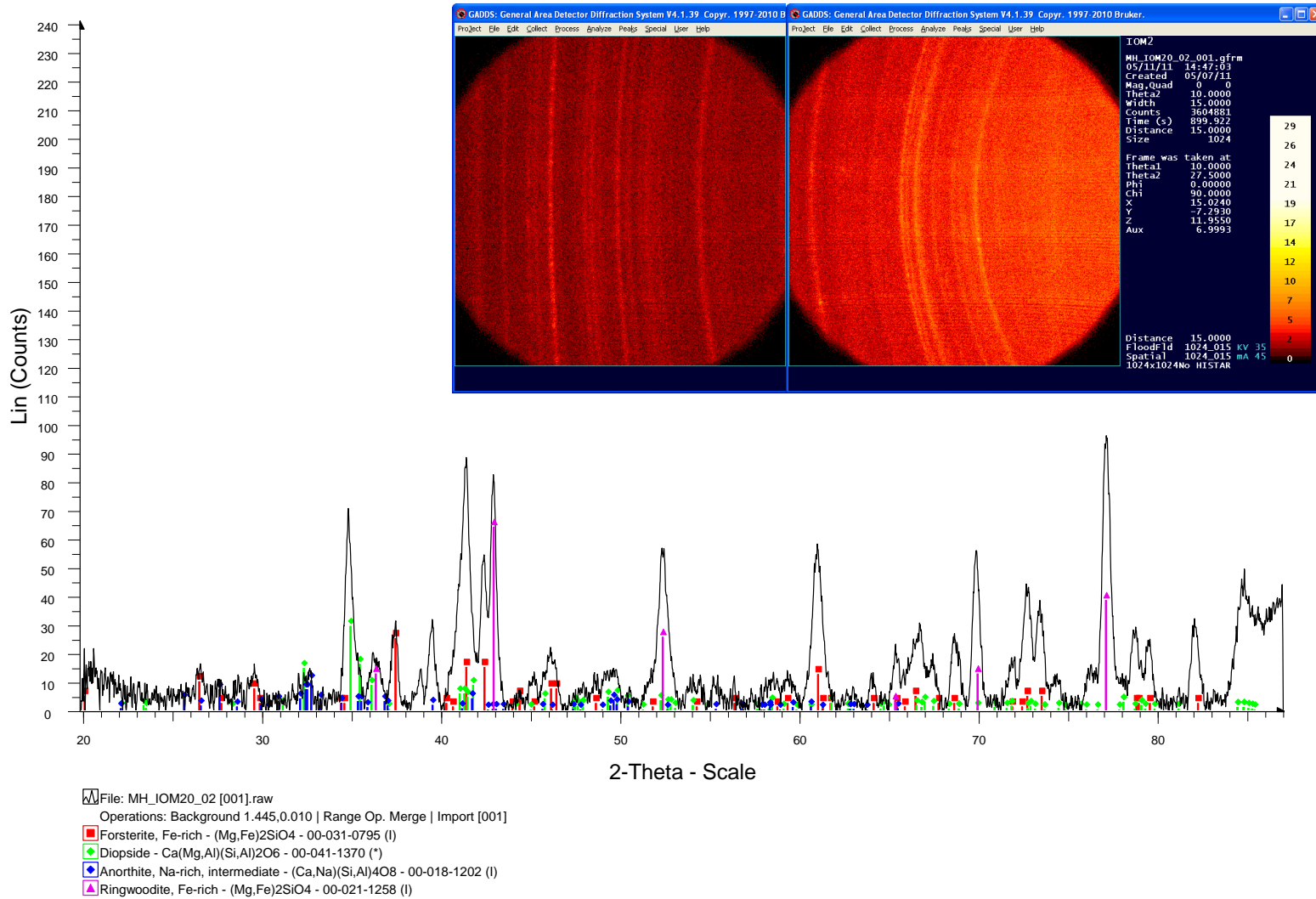
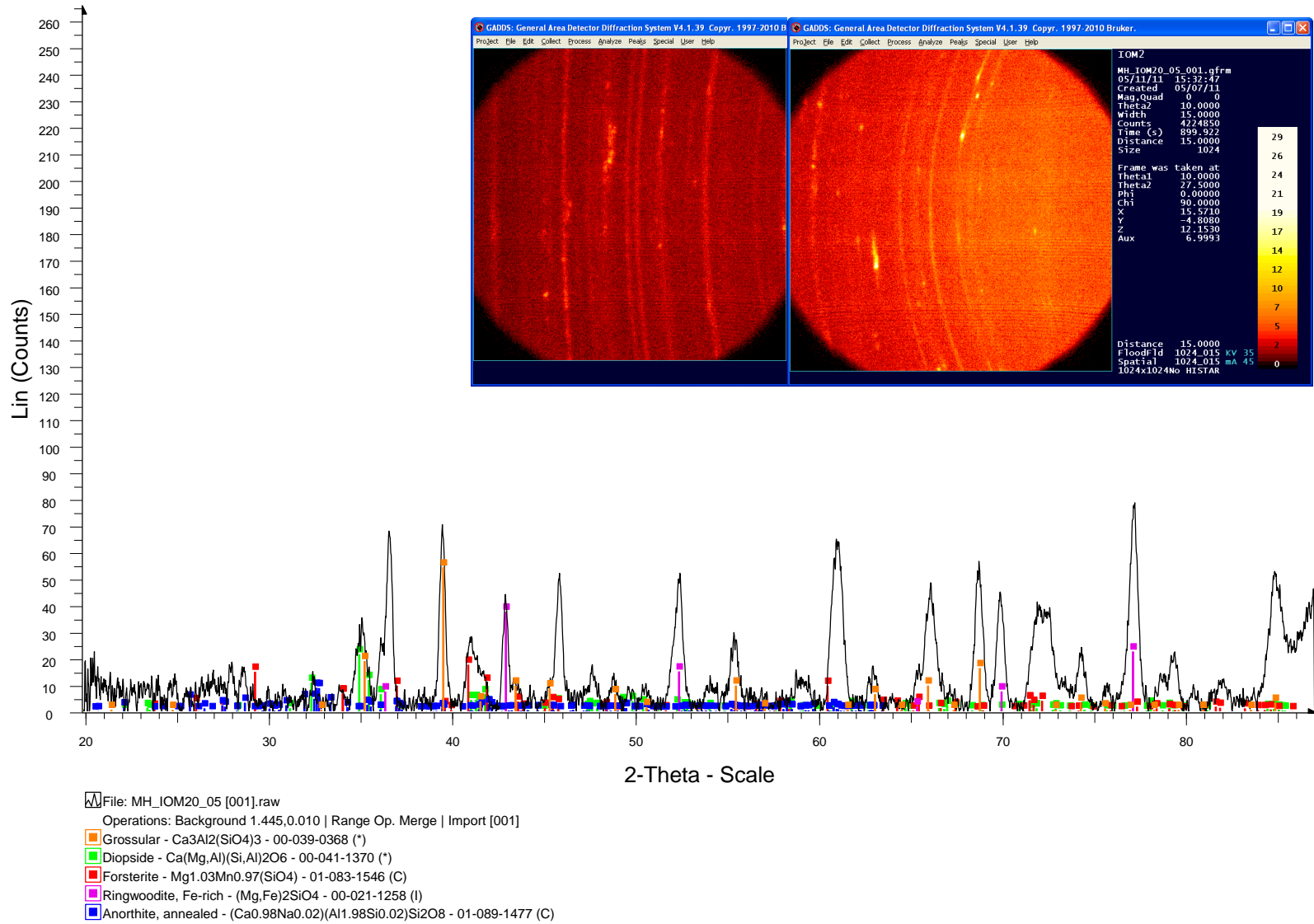# Appendix 2

Micro-XRD of Cr.3.7c CAIs and Sample Selection

A total of 129 points were collected from 29 CAIs from Allende Cr.3.7c using micro-XRD with a beam width of 300 μm and Co Kα radiation . All points were collected using omega scans consisting of two frames each taking 15 minutes to collect. The parameters for each frame are presented below in Table 1.
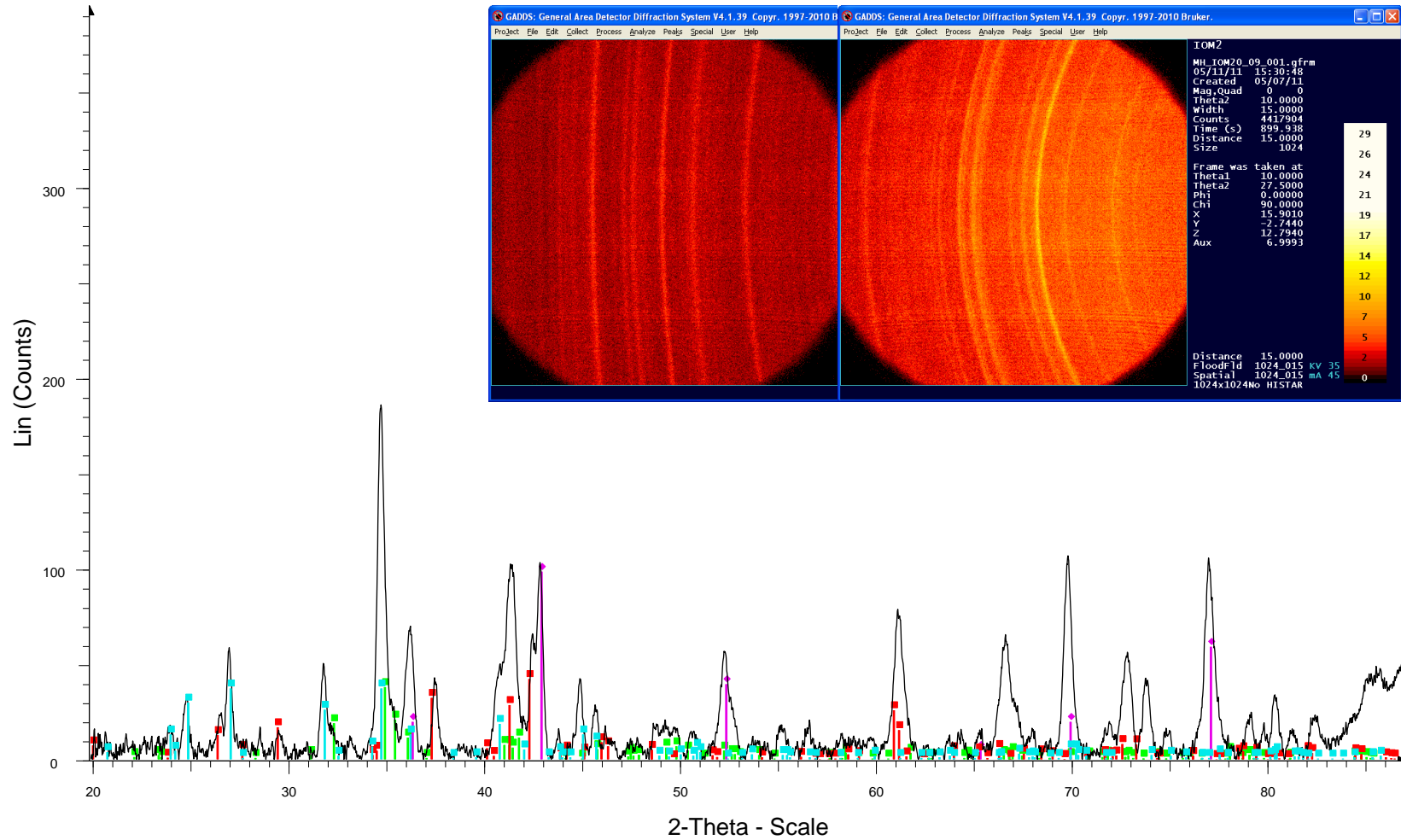
Table 1. Acquisition Parameters for the Allende Cr.3.7c CAIs.		
	Frame 1	Frame 2
σ_1	10°	25°
σ_2	27.5°	45°
2θ	37.5°	70°
width	15°	25°

From μ-XRD, the Allende Cr.3.7c CAIs were found to contain spinel, fassaite, gehlenite, forsterite, nepheline, grossular, and anorthite. The XRD patterns of the CAIs however, consisted mainly of solid rings indicating that the phases within the CAIs were polycrystalline. For the purposes of this study, CAIs with abundant coarse grained (~ 50 – 100 μm diameter) fassaite that is relatively free of inclusions of other phases were needed. The fassaite in the Cr.3.7c CAIs was too fine grained and intergrown with other phases to be used in this study. Some sample XRD patterns of the CAIs are shown below. The mineralogy of the Cr.3.7.c CAIs included primary phases such as anorthite, forsterite, fassaite, and spinel (with a similar unit cell to ringwoodite) as well as secondary phases such as grossular and nepheline.

Representative Micro XRD Data from the Cr.3.7.c CAIs

File: MH_IOM20_02 [001].raw
Operations: Background 1.445,0.010 | Range Op. Merge | Import [001]

■ Forsterite, Fe-rich - (Mg,Fe)2SiO4 - 00-031-0795 (I)
◆ Diopside - Ca(Mg,Al)(Si,Al)2O6 - 00-041-1370 (*)
◆ Anorthite, Na-rich, intermediate - (Ca,Na)(Si,Al)4O8 - 00-018-1202 (I)
▲ Ringwoodite, Fe-rich - (Mg,Fe)2SiO4 - 00-021-1258 (I)

File: MH_IOM20_05 [001].raw
Operations: Background 1.445,0.010 | Range Op. Merge | Import [001]
Grossular - Ca3Al2(SiO4)3 - 00-039-0368 (*)
Diopside - Ca(Mg,Al)(Si,Al)2O6 - 00-041-1370 (*)
Forsterite - Mg1.03Mn0.97(SiO4) - 01-083-1546 (C)
Ringwoodite, Fe-rich - (Mg,Fe)2SiO4 - 00-021-1258 (I)
Anorthite, annealed - (Ca0.98Na0.02)(Al1.98Si0.02)Si2O8 - 01-089-1477 (C)

Lin (Counts)

400

300

200

100

0

20   30   40   50   60   70   80

2-Theta - Scale

GADDS: General Area Detector Diffraction System V4.1.39 Copyr. 1997-2010 B
GADDS: General Area Detector Diffraction System V4.1.39 Copyr. 1997-2010 Bruker.

ProJect File Edit Collect Process Analyze Peaks Special User Help
ProJect File Edit Collect Process Analyze Peaks Special User Help

IOM2
MH_IOM20_13_001.gfrm
05/11/11 15:29:13
Created   05/07/11
Mag.Quad   0   0
Theta2   10.0000
Width   15.0000
Counts   4678370
Time (s)   899.922
Distance   15.0000
Size   1024

Frame was taken at
Theta1   10.0000
Theta2   27.5000
Phi   0.00000
Chi   90.0000
X   15.3670
Y   -0.8980
Z   12.5000
Aux   6.9993

29
26
24
21
19
17
14
12
10
7
5
2
0

Distance   15.0000
FloodFld   1024_015 KV 35
Spatial   1024_015 mA 45
1024x1024No HISTAR

File: MH_IOM20_12 [001].raw
Operations: Background 1.445,0.010 | Range Op. Merge | Import [001]
Ringwoodite, Fe-rich - (Mg,Fe)2SiO4 - 00-021-1258 (I)
Fassaite - (Ca0.968Mg0.578Fe0.220Al0.161Ti0.059)(Si1.728Al0.272)O6 - 01-083-2083 (C)
Nepheline - Na6K1.2Al7.2Si8.8O32 - 01-085-1487 (C)
Forsterite - Mg1.360Fe0.640SiO4 - 01-076-0552 (C)
Grossular - (Ca2.869Fe0.131)(Al1.89Fe0.11)(SiO4)3 - 01-085-1508 (C)

Appendix 3 – SEM EDS Data

CAI – bearing Allende Fragments (CV3.7.c)

Two Allende meteorite fragments were provided by Dr. Carl Agee at the Institute of Meteoritics, University of New Mexico. The two meteorite fragments had weights of 13.74 and 0.17 g. The largest of the two fragments contained small CAIs less than 5 mm in diameter as well as a significant amounts of chondrules (35 vol. %). CAIs were then extracted from the Allende meteorite fragment using freeze thaw methods (See appendix 1). After the CAIs were extracted their mineralogy was determined using micro-XRD (See appendix 2) and largest, coarsest grained CAIs containing the most fassaite were chosen for subsequent SEM-EDS analysis (see below).
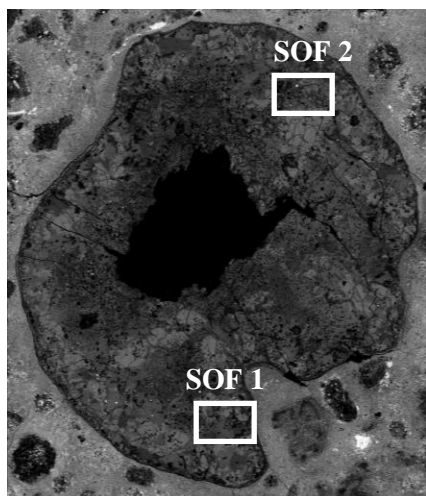
CAI 1
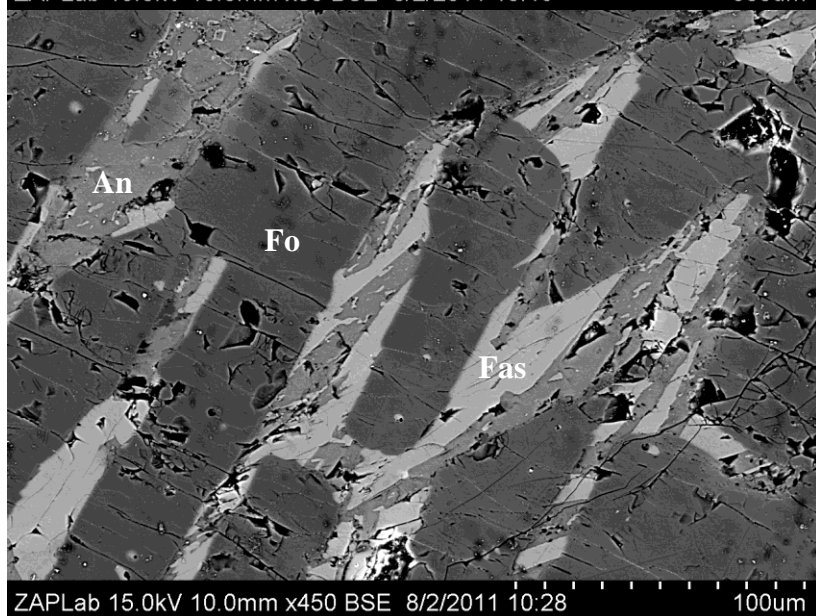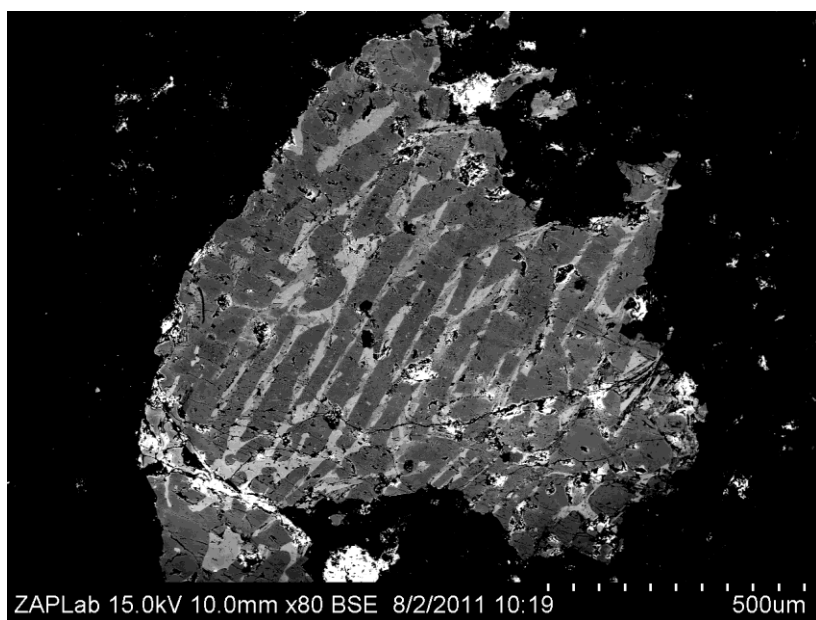
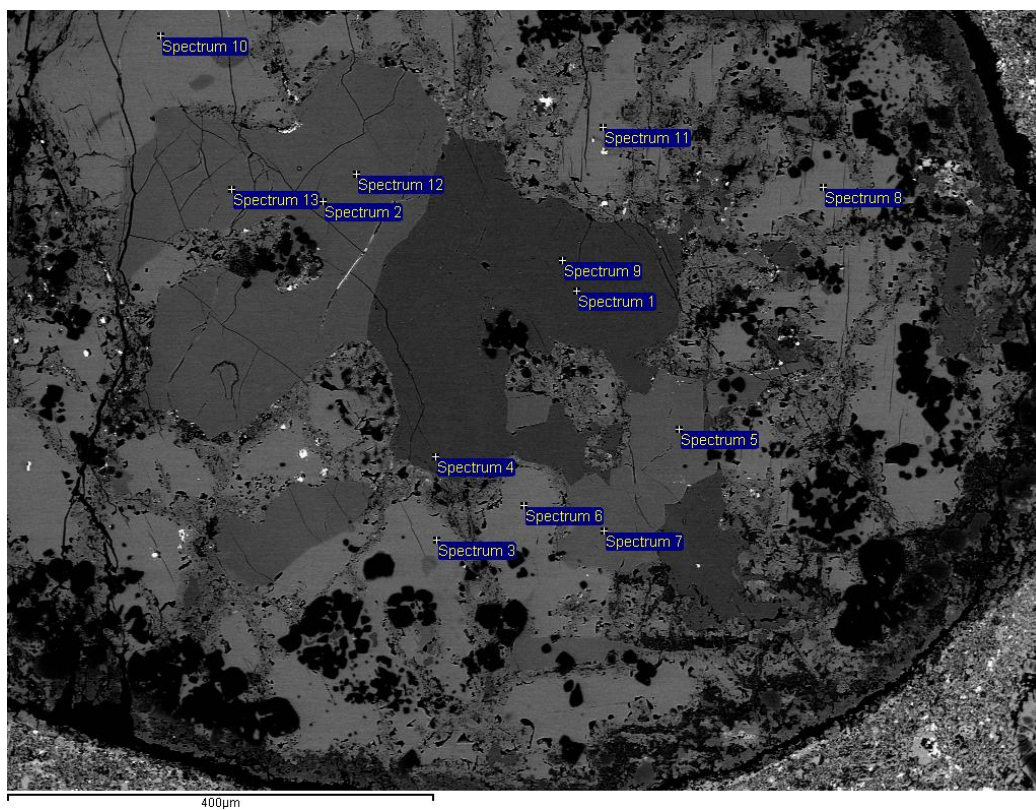**CAI 2**
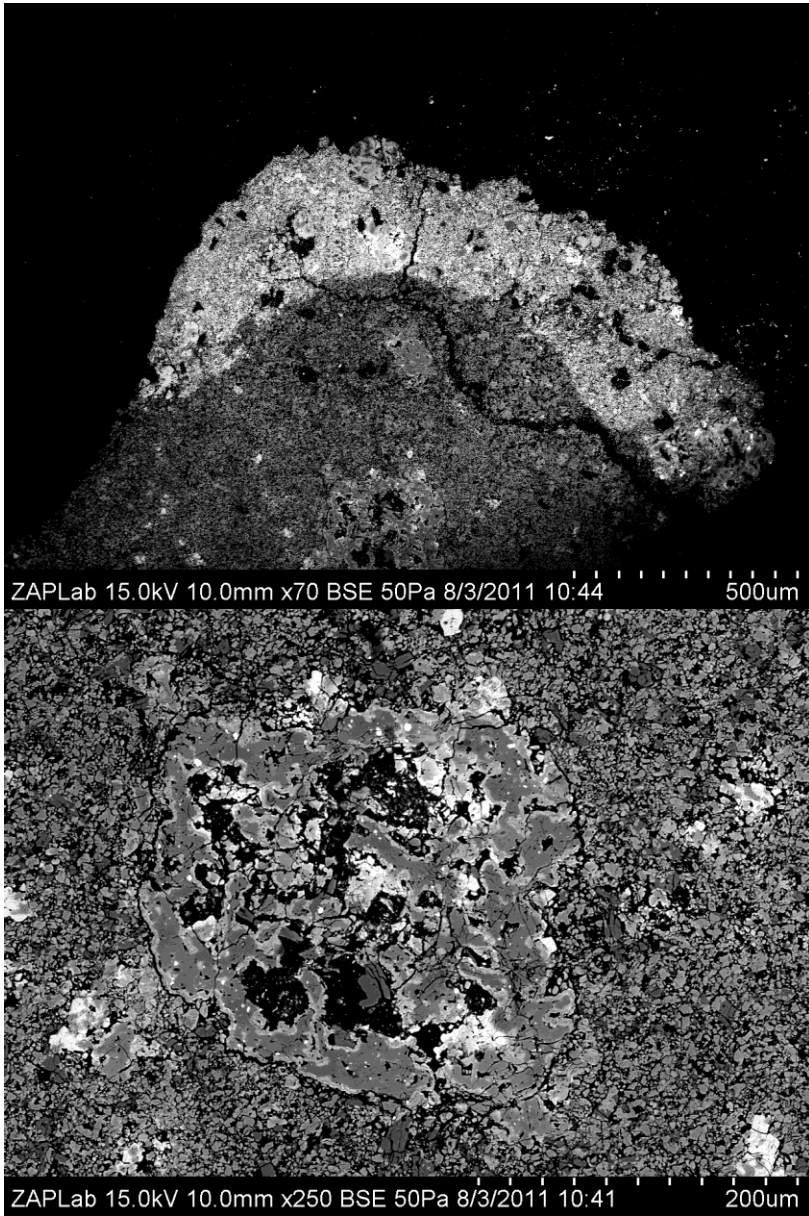
SEM EDS point Analysis

TS62B

TS62B Site of Interest (SOF) 1

Spectrum 1 (Anorthite)
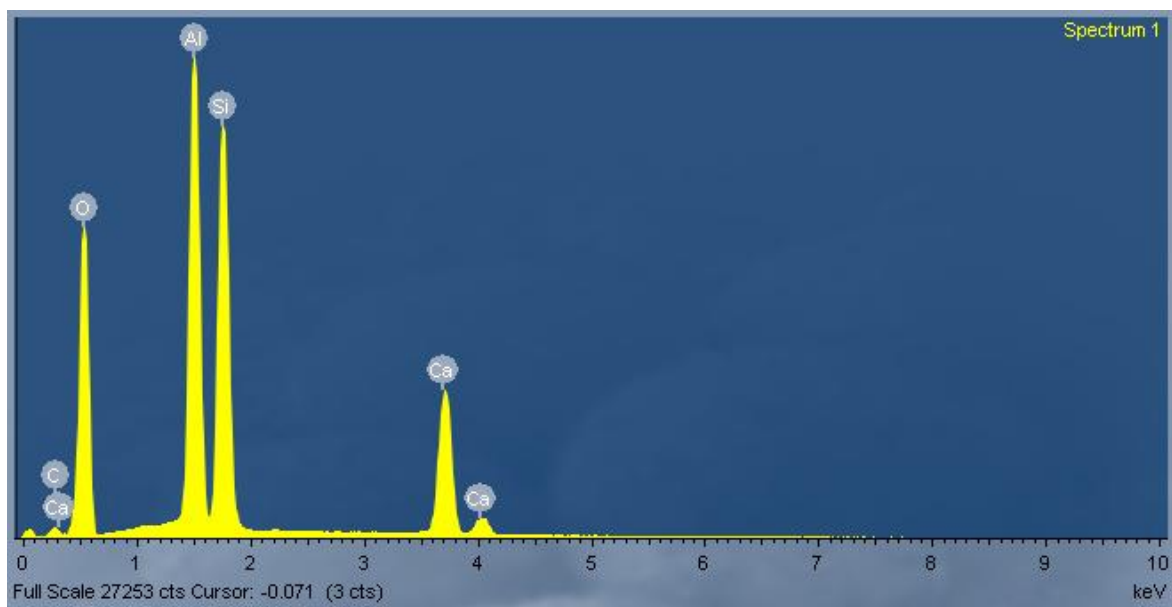
Spectrum 2 (fassaite)
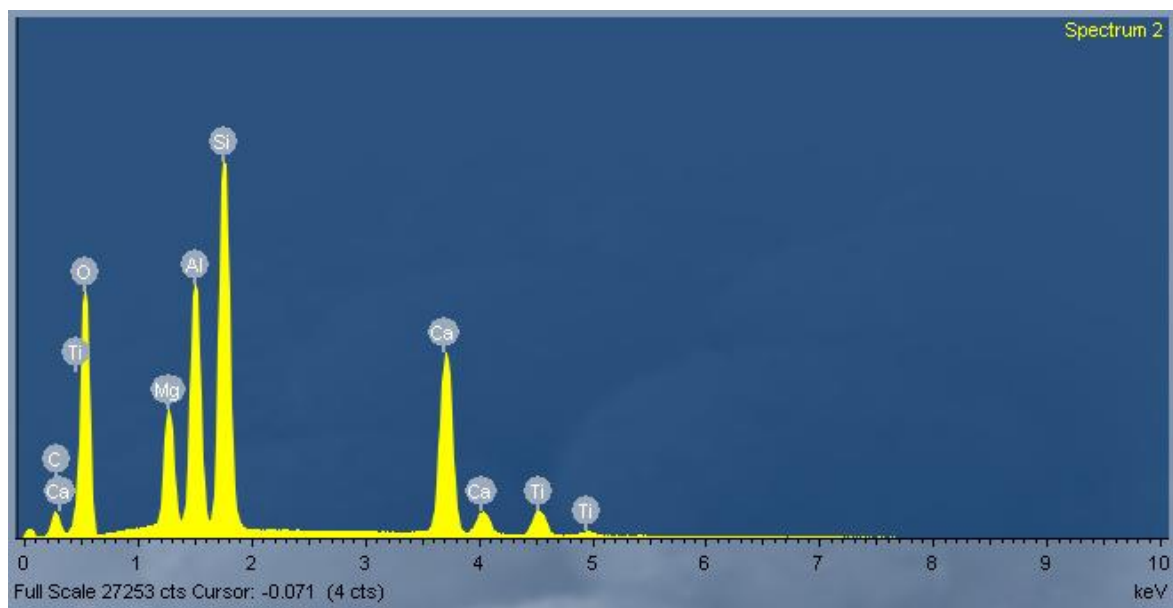
Spectrum 3

TS62B Site of Interest (SOF) 2

Spectrum 1 (Melilite)

Spectrum 11 (Spinel)

USNM 3529

ZAPLab 15.0kV 10.0mm x50 BSE 12/7/2011 14:58   1.00mm

USNM 3529 Site of Interest (SOF) 1

Spectrum 1 (Spinel)

Spectrum 4 (Melilite)

Spectrum 9 (Fassaite)

Appendix 4

EPMA Results from Allende TS62B Fassaite

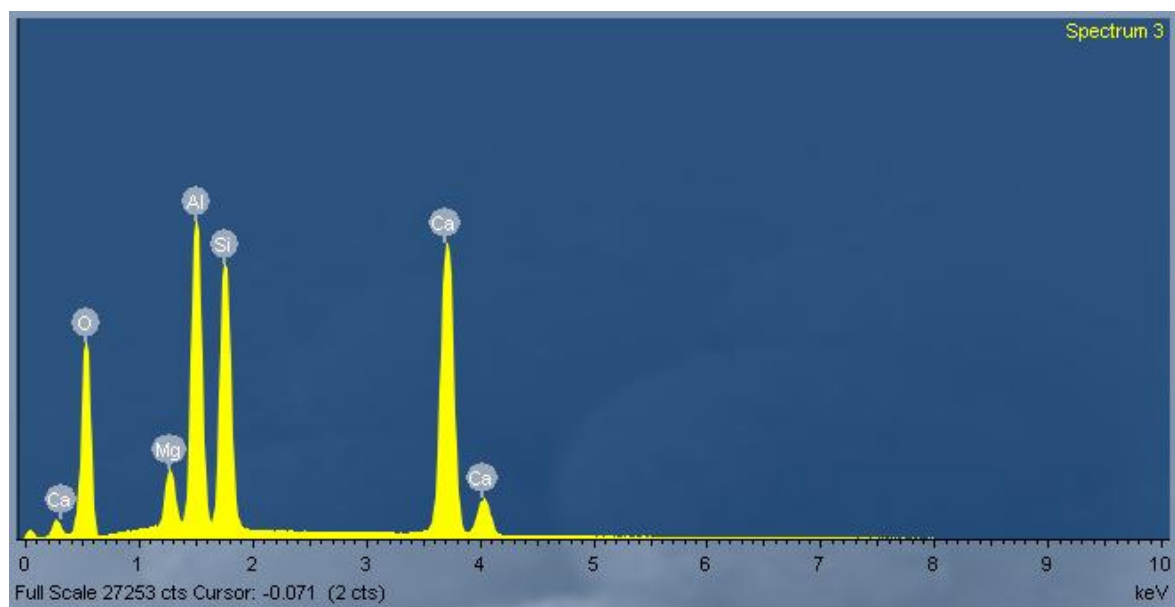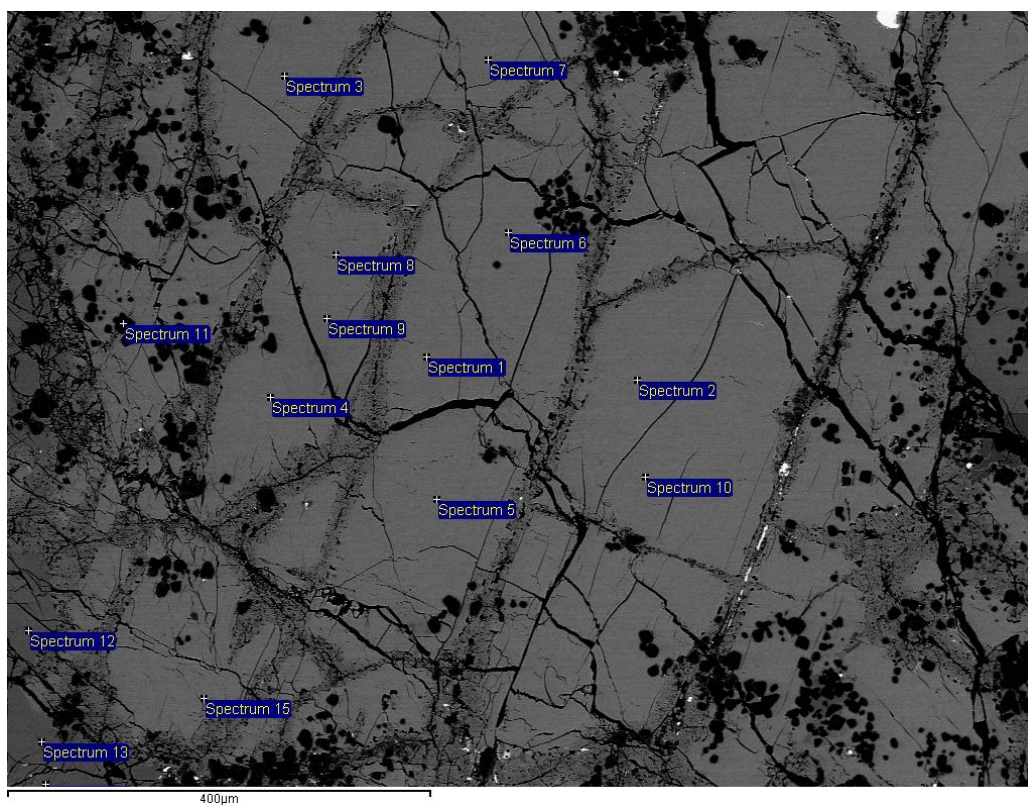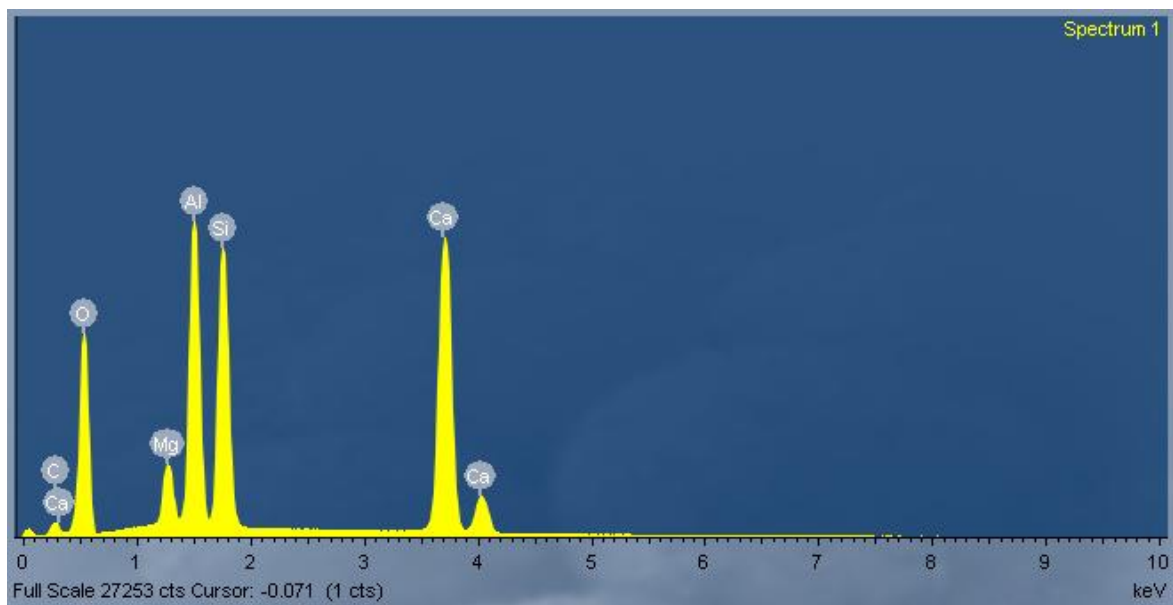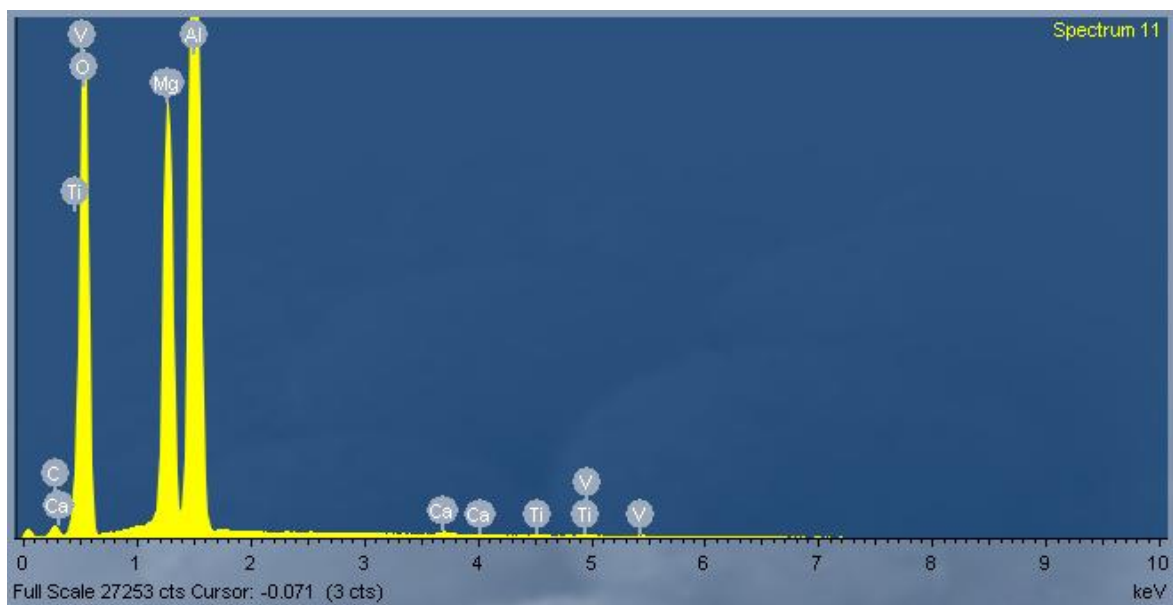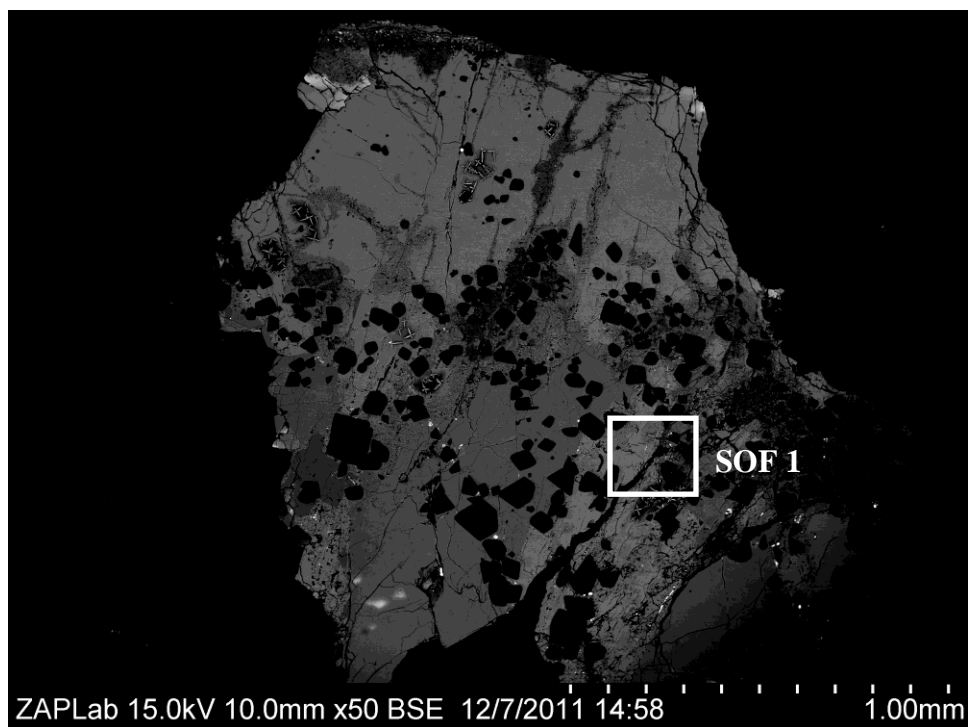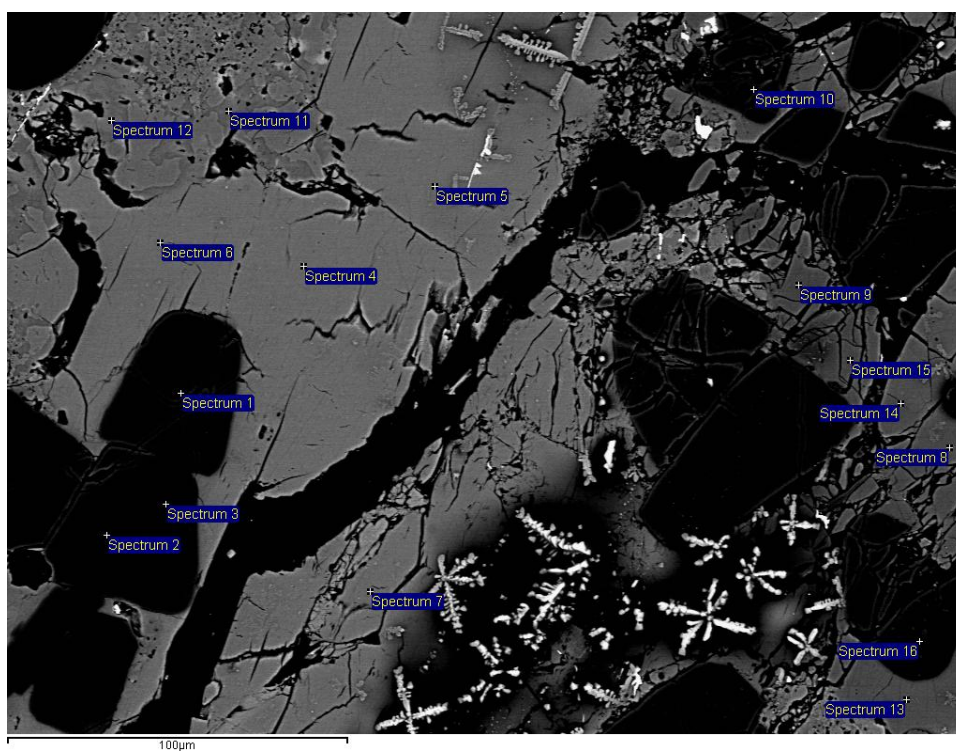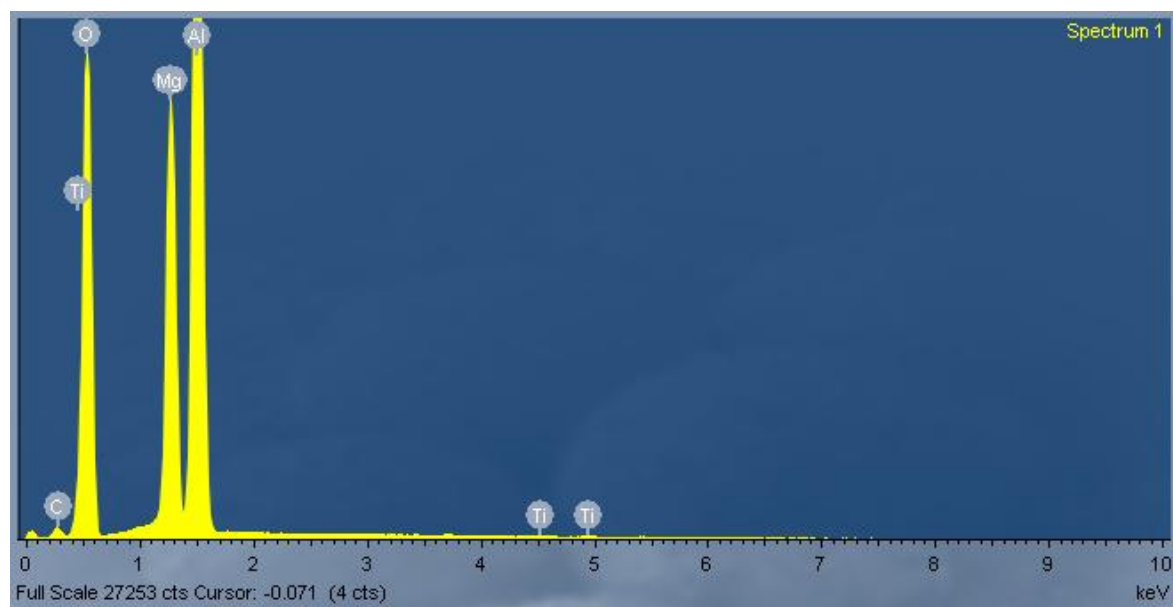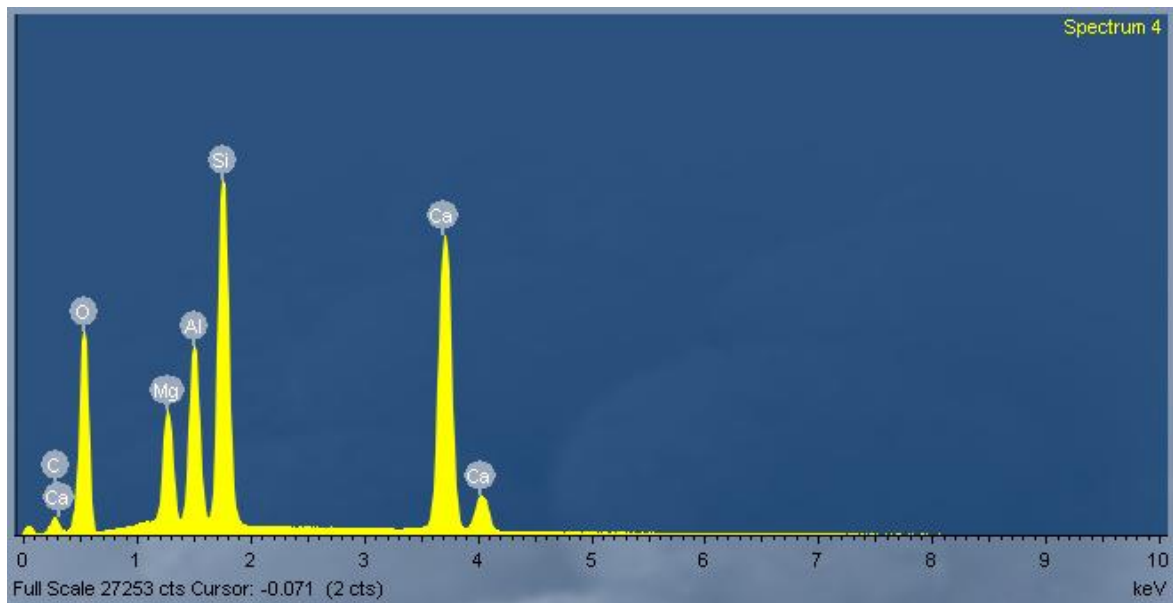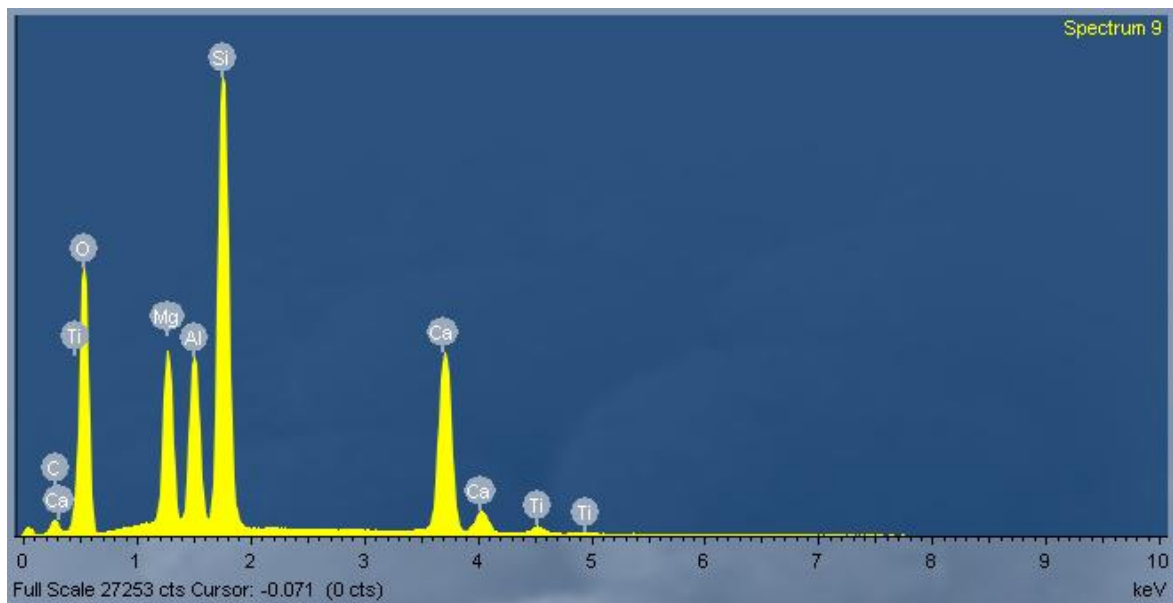| ANALYSIS	SiO$_2$	TiO$_2$	Al$_2$O$_3$	Cr$_2$O$_3$	FeO	MgO	MnO	K2O	CaO	Na$_2$O	Total
1	37.94	6.58	19.51	0.04	0.06	9.94	0.14	0.00	25.63	0.01	99.85
2	37.70	6.37	20.18	0.07	0.07	9.79	0.02	0.03	25.39	0.01	99.63
3	43.43	4.50	14.82	0.03	0.21	11.83	0.04	0.05	25.74	0.07	100.72
4	38.18	6.90	20.97	0.08	0.00	8.95	0.00	0.00	25.54	0.01	100.63
5	42.43	5.38	15.24	0.12	0.07	11.45	0.00	0.04	25.67	0.00	100.40
6	40.49	6.06	18.10	0.08	0.05	10.16	0.00	0.04	25.19	0.02	100.19
7	42.42	3.33	15.50	0.05	0.01	12.81	0.00	0.07	25.64	0.00	99.83
8	37.74	6.30	19.81	0.00	0.00	9.98	0.00	0.02	25.70	0.00	99.55
9	39.33	5.41	19.59	0.02	0.08	10.12	0.00	0.08	25.64	0.03	100.30
10	39.17	6.12	19.15	0.03	0.11	10.10	0.00	0.04	26.03	0.00	100.75
11	42.60	3.49	15.46	0.05	0.40	11.94	0.11	0.06	25.67	0.04	99.82
12	37.44	7.73	19.67	0.08	0.05	8.73	0.05	0.03	26.13	0.04	99.95
13	37.34	7.17	19.90	0.05	0.05	8.56	0.00	0.06	26.72	0.00	99.85
14	40.54	7.49	16.19	0.01	0.00	10.53	0.00	0.05	25.77	0.00	100.58
15	38.46	5.77	19.33	0.05	0.01	9.96	0.00	0.03	26.05	0.01	99.67
16	38.82	5.97	19.31	0.08	0.02	10.23	0.00	0.06	25.86	0.00	100.35
17	43.44	4.10	13.94	0.02	0.04	12.58	0.02	0.05	25.83	0.04	100.06
18	40.85	4.83	15.61	0.03	0.08	12.27	0.02	0.03	26.10	0.03	99.85
19	40.33	5.43	17.49	0.04	0.29	10.24	0.00	0.06	25.81	0.08	99.77
20	40.51	6.36	17.76	0.03	0.03	9.46	0.00	0.05	25.57	0.01	99.78
21	35.56	8.19	22.21	0.11	0.07	8.23	0.05	0.03	25.78	0.00	100.23
22	38.06	6.17	20.75	0.11	0.07	8.88	0.09	0.04	25.84	0.00	100.01
23	38.55	7.15	18.65	0.14	0.00	9.79	0.00	0.01	25.83	0.00	100.12
24	40.29	5.55	18.14	0.05	0.03	10.44	0.00	0.04	25.62	0.01	100.17
25	41.37	5.53	15.84	0.07	0.03	11.17	0.00	0.02	25.86	0.02	99.91
26	37.71	7.91	20.27	0.07	0.00	8.25	0.02	0.07	25.84	0.02	100.16
27	37.78	7.84	20.68	0.04	0.00	8.33	0.00	0.05	25.56	0.02	100.30
28	35.98	7.59	22.05	0.05	0.02	7.99	0.05	0.05	25.73	0.00	99.51
29	37.14	7.15	20.94	0.03	0.02	8.84	0.04	0.02	25.47	0.00	99.65
30	37.43	6.63	21.58	0.11	0.01	8.83	0.00	0.04	25.74	0.02	100.39
31	37.60	6.31	20.97	0.13	0.05	9.38	0.00	0.03	25.75	0.01	100.23
32	37.25	6.23	20.00	0.06	0.00	9.97	0.00	0.06	26.15	0.01	99.73
33	38.49	6.53	19.71	0.04	0.12	9.77	0.00	0.05	25.66	0.00	100.37
34	37.49	7.66	18.90	0.08	0.06	9.84	0.10	0.01	26.10	0.01	100.25

35	38.97	5.77	19.76	0.04	0.02	9.86	0.05	0.02	26.27	0.00	100.76
36	37.71	4.36	22.22	0.15	0.00	10.07	0.12	0.05	25.95	0.02	100.65
37	38.99	4.62	20.61	0.05	0.02	10.96	0.12	0.02	25.39	0.01	100.79

EPMA Results from Allende USNM 3529 Fassaite

ANALYSIS	SiO_2	TiO_2	Al_2O_3	Cr_2O_3	FeO	MgO	MnO	K2O	CaO	Na_2O	Total
1	38.99	7.46	20.25	0.03	0.01	7.84	0.01	0.03	25.45	0.00	100.07
2	39.07	7.45	18.67	0.08	0.06	8.73	0.04	0.00	26.09	0.03	100.22
3	38.01	6.98	17.89	0.06	0.06	10.79	0.01	0.00	25.99	0.00	99.79
4	39.33	5.41	19.59	0.01	0.04	10.12	0.00	0.05	25.46	0.02	100.03
5	42.42	5.12	16.89	0.03	0.01	8.98	0.02	0.06	25.54	0.02	99.09
6	40.10	6.15	18.14	0.02	0.02	10.12	0.02	0.03	25.78	0.03	100.41
7	40.34	6.12	18.67	0.05	0.09	8.76	0.01	0.01	26.01	0.01	100.07
8	40.45	5.78	18.76	0.10	0.00	9.46	0.04	0.02	25.65	0.01	100.27
9	37.34	7.87	20.03	0.03	0.01	8.56	0.02	0.02	25.98	0.01	99.87
10	41.56	7.49	16.19	0.01	0.00	10.53	0.03	0.06	25.01	0.00	100.88
11	38.82	5.97	19.31	0.04	0.02	10.23	0.00	0.00	25.76	0.00	100.15
12	38.55	7.15	18.65	0.10	0.00	9.87	0.01	0.00	25.83	0.01	100.17
13	40.12	6.89	19.05	0.07	0.08	7.24	0.04	0.01	25.79	0.07	99.36
14	42.78	4.67	18.89	0.01	0.01	9.45	0.00	0.02	25.01	0.01	100.85
15	37.89	6.17	21.24	0.09	0.01	8.88	0.09	0.01	25.81	0.01	100.20
16	37.78	7.84	20.31	0.02	0.00	8.12	0.00	0.04	25.78	0.00	99.89
17	38.89	8.01	20.27	0.05	0.04	7.34	0.03	0.01	24.98	0.01	99.63
18	41.37	5.53	16.74	0.05	0.03	11.02	0.01	0.01	25.45	0.00	100.21
19	42.39	5.76	16.07	0.05	0.01	10.96	0.02	0.00	25.25	0.01	100.52
20	36.58	6.63	22.65	0.10	0.07	7.76	0.02	0.02	26.12	0.00	99.95
21	36.14	7.59	21.90	0.01	0.08	7.89	0.00	0.01	26.35	0.02	99.99
22	38.97	5.77	20.13	0.03	0.03	9.01	0.04	0.04	26.27	0.01	100.30
23	40.85	4.83	20.34	0.06	0.09	7.65	0.00	0.05	26.00	0.05	99.92
24	37.49	5.87	19.78	0.08	0.05	11.00	0.05	0.00	26.10	0.01	100.43
25	38.01	3.21	22.22	0.15	0.00	10.07	0.10	0.07	25.93	0.00	99.76
26	39.45	7.35	19.04	0.04	0.12	8.80	0.01	0.00	25.35	0.00	100.16

Appendix 5

Deconvolution of tetrahedral and Octahedral Peaks from the ^{27}Al 3QMAS NMR spectra of Allende TS62B and USNM 3529 Fassaite

From ^{27}Al 3QMAS NMR spectroscopy of Allende TS62B and USNM 3529 spectroscopy, five to six tetrahedral peaks and two octahdedral peaks were resolved. Since ^{27}Al 3QMAS NMR produces 2D spectra, cross-sections along the F2 dimension of the three dimensional peaks must be taken (Fig. 1a & 2a). These cross-sections are plotted as two dimensional peaks (Fig 1b,c & 2 b,c) which are used for peak deconvolution.
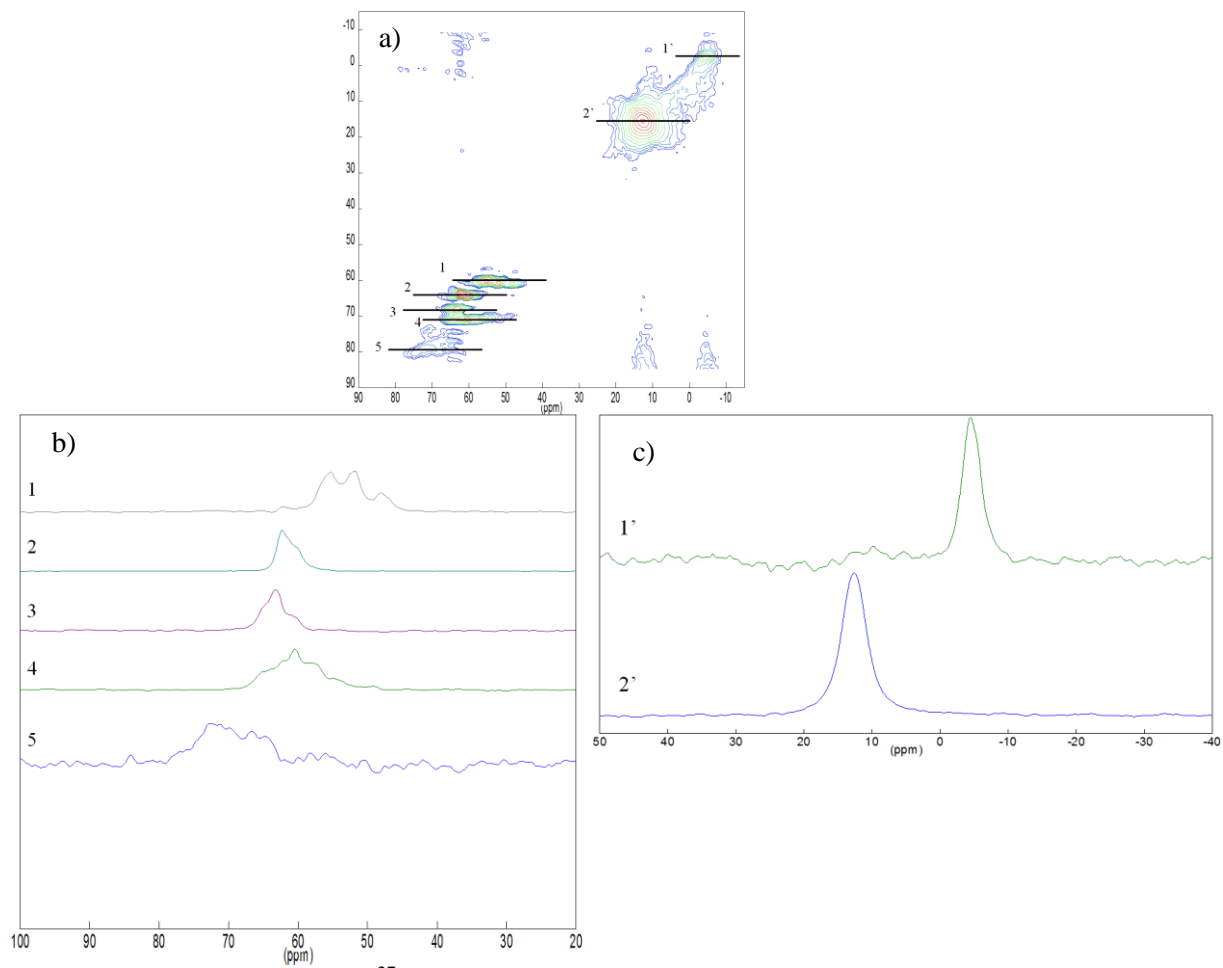
Figure 1. a) Two dimensional ^{27}Al 3QMAS NMR spectra of Allende TS62B with b) tetrahedral and c) octahedral peak cross-sections.
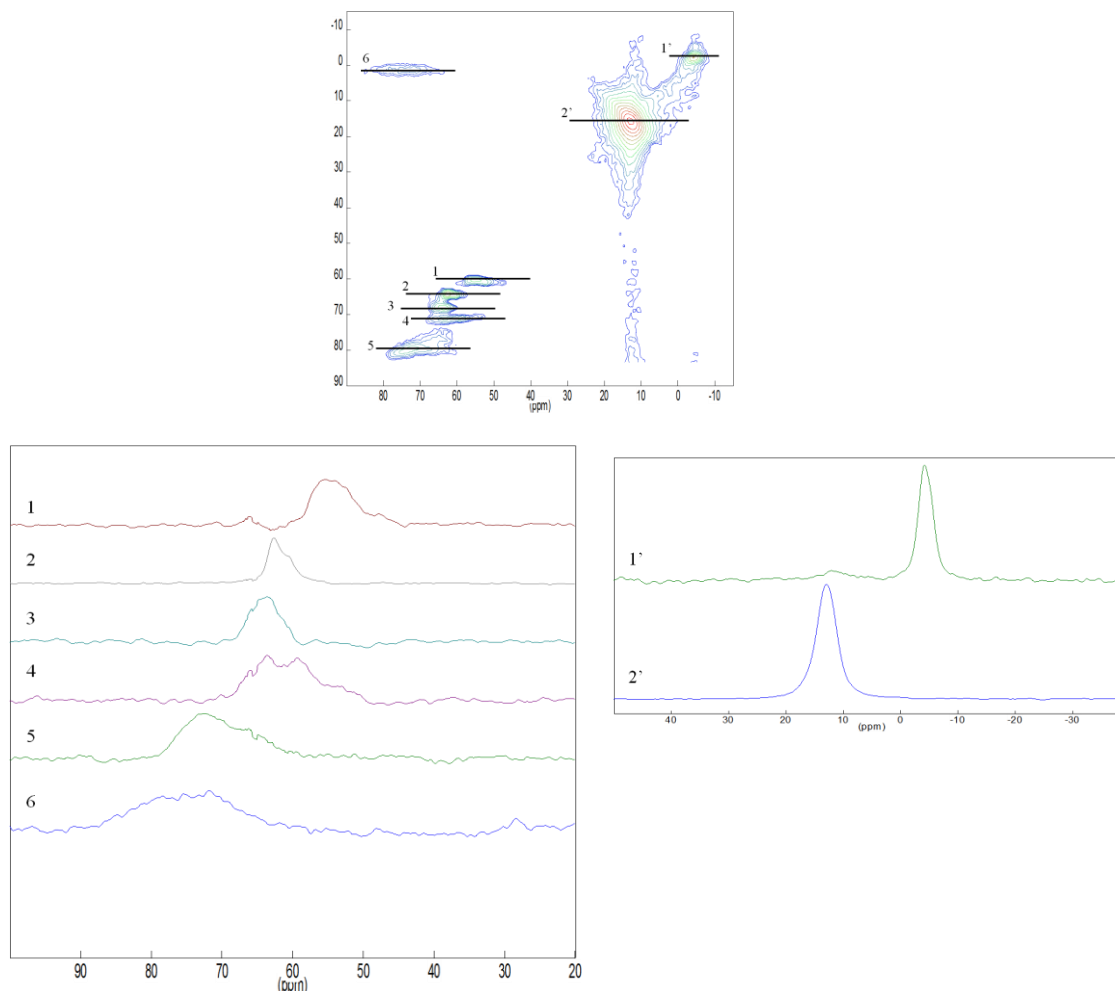
Figure 2. a) Two dimensional ^{27}Al 3QMAS NMR spectra of Allende USNM 3529 fassaite with b) tetrahedral and c) octahedral peak cross – sections.

The tetrahedral and octahedral peaks were fitted using DMFit software by Massiot et al. (2011). Due to quadrupolar broadening effects on the tetrahedral peaks, the tetrahedral peaks were fit with a quadrupolar line shape (Fig. 3 & 4). Unlike the tetrahedral peaks, quadrupolar broadening had little effect on the octahedral peaks so the octahedral peaks were fit with a Gauss/Lorentzian line shape (Fig. 3 & 4).
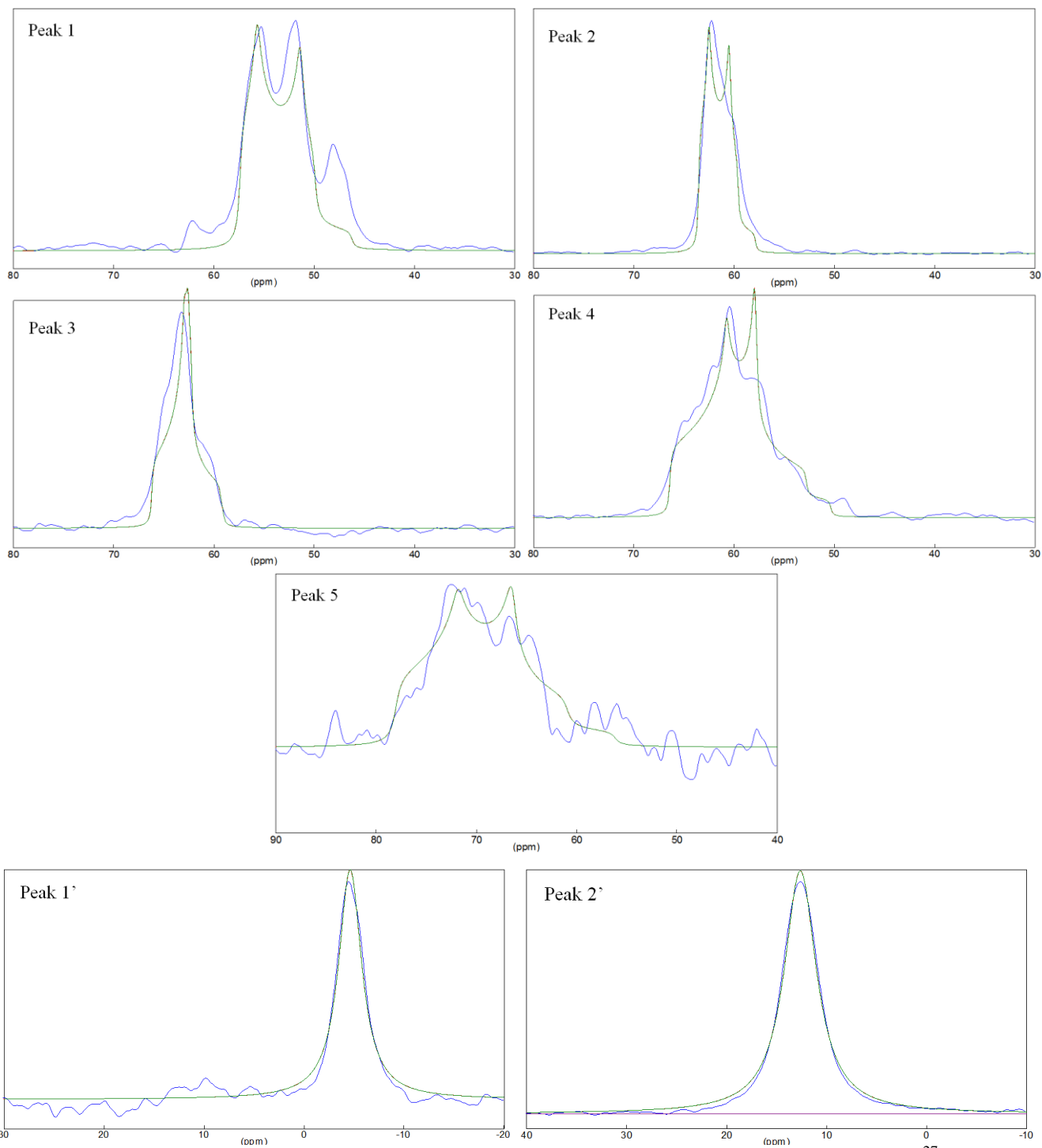
Figure 3. Tetrahedral (Peaks 1 to 5) and octahedral (Peaks 1' and 2') peak deconvolutions from the ^{27}Al 3QMAS NMR spetcrum of Allende TS62B Fassaite.

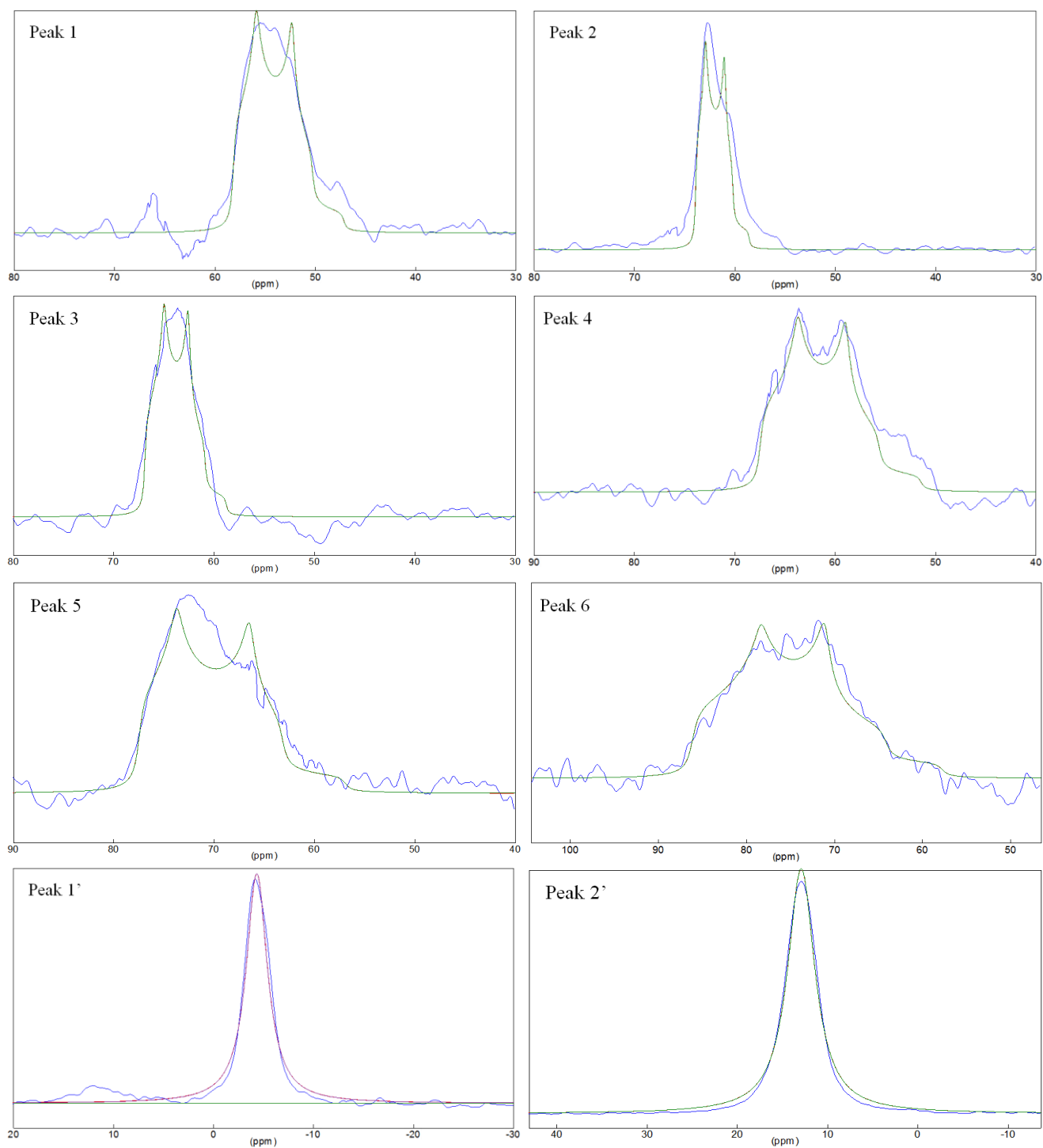Figure 4. Tetrahedral (Peaks 1 to 6) and octahedral (Peaks 1' and 2') peak deconvolutions from the ^{27}Al 3QMAS NMR spetcrum of Allende USNM 3529 Fassaite.

MONIKA HARING CV

EDUCATION

University of Western Ontario, London, ON
M.Sc. Candidate in Geology   **2010 to present**

Laurentian University, Sudbury, ON
B.Sc. Honors in Geology   **2010**
Areas of Concentration: Geochemistry, Mineralogy, and Petrology
Honors Thesis: "UK117 & UK 120: Two Potentially New Minerals
From Mont Saint-Hilaire, Quebec, Canada"

PUBLICATIONS AND PAPERS
Haring, M., McDonald, A.M., Poirier, G. and Cooper, M.A.*:"Steedeite"* , IMA 2010-049.
CNMNC Newsletter, February 2010, page 28; Mineralogical Magazine, 75, 27-31.
2010

Haring, M. McDonald, A.M., Poirier, G. and Cooper, M.A*. :" Laurentianite*", IMA 2010-018.
CNMNC Newsletter, August 2010, p.798, Mineralogical Magazine 74, 797-800.   **2010**

Haring, M., McDonald, A.M., Poirier, G. and Cooper, M.A. (2011). "*Laurentianite, a
new Na-Nb-silicate hydrate mineral from Mont Saint-Hilaire, Quebec: Description,
crystal structure determination and comments on the occurrence of Nb in agpaitic
environments"*. Canadian Mineralogist. 50. (in press)   **2012**

POSTERS AND PRESENTATIONS

M. M. Haring, R.L. Flemming, V. Terskikh, L. Grossman and S. B. Simon**,** Extraterrestrial and
Terrestrial Fassaite Compared: Allende CV3 versus Fassa Valley, Italy. (Poster for the Canadian Space
Summit, London, Ontario)   **2012**

M. M. Haring, R.L. Flemming, V. Terskikh, L. Grossman and S. B. Simon**,** "Crystal Structure and
Cation
ordering in Fassaite from Type B CAI TS62B in Allende CV3"(Poster for the Lunar and Planetary
Science
Conference, The Woodlands, Texas, USA)   **2012**

Flemming, R., McCausland, P.J.A., Izawa, M.R.M., Craig, M.A., **Haring, M.**, Edey D.R, Shivak, J.N.,
 Kanhai, J., Banerjee, N.R., Osinski, G.R., Holdsworth, D.W., Cloutis, E.A. and King, P.L.
"Astromaterials I:
Representative Materials from Across the Solar System" (Poster for the Center for Advanced
Materials & Biomaterials Research (CAMBR) conference University of Western Ontario, Canada.)

Flemming, R., McCausland, P.J.A., Izawa, M.R.M., Craig, M.A., **Haring, M.**, Edey D.R, Shivak, J.N.,
Kanhai, J., Banerjee, N.R., Osinski, G.R., Holdsworth, D.W., Cloutis, E.A. "Astromaterials II:
Shock Metamorphosed Meteorites and Terrestrial Materials" (Poster for CAMBR conference
                                                                    2011

University of Western Ontario, Canada)
Haring, M. "Laurentianite & Steedeite: two new minerals from Mont Saint Hilaire, Quebec, Canada",
Public Lectures for the London Gem and Mineral Club and the Walker Mineralogical Club
2010

Haring, M., "Introduction to Raman Spectroscopy", Oral presentation,
Laurentian University Department of Earth Sciences.
2008

Haring, M., "Neutron Diffraction for Earth Sciences", Oral presentation,
Laurentian University Department of Earth Sciences.
2008

AWARDS

NSERC Alexander Graham Bell Canada Graduate Scholarship   Sep.1st 2011 –
Sep.1st 2012
Ontario Graduate Scholarship   Sep.1st 2010 – Sep.
1st 2011
Dennis David Trevisiol Memorial Scholarship
Sep.1st 2009 – Sep. 1st 2010
Teck Cominco Scholarship
Sep.1st 2009 – Sep. 1st 2010
NSERC Undergraduate Research Student Award   May. 4th 2009 –
Aug. 28th 2009
DeBeers Canada Scholarship
Sep. 1st 2008 – Sep. 1st 2009
Mineralogical Association of Canada Student Award   Sep. 1st 2008 – Sep.
1st 2009
Marsh A. Cooper Award
Sep. 1st 2007 – Sep. 1st 2008
Laurentian University entrance Scholarship   Sep. 1st 2006 – Apr.
3rd 2010

MEMBERSHIPS

Mineralogical Association of Canada
Mineralogical Society of America